Constraining Properties of Dark Matter particles Using Astrophysical Data

Iakubovskyi, D.

Cover Page

The handle http://hdl.handle.net/1887/20523 holds various files of this Leiden University dissertation.

Author: Iakubovskyi, Dmytro
Title: Constraining properties of dark matter particles using astrophysical data
Issue Date: 2013-02-13

Constraining properties of dark matter particles using astrophysical data

PROEFSCHRIFT

TER VERKRIJGING VAN DE GRAAD
VAN DOCTOR AAN DE UNIVERSITEIT LEIDEN,
OP GEZAG VAN RECTOR MAGNIFICUS
PROF. MR. C. J. J. M. STOLKER,
VOLGENS BESLUIT VAN HET COLLEGE VOOR PROMOTIES
TE VERDEDIGEN OP 13 FEBRUARI 2013
TE KLOKKE 15.00 UUR

DOOR

Dmytro Iakubovskyi

GEBOREN TE KRIVOY ROG, OEKRAÏNE IN 1983

Promotor:	Prof. dr. A. Achúcarro
Co-promotor:	Dr. A. Boyarsky
Overige leden:	Prof. dr. E.R. Eliel
	Universiteit Leiden
	Prof. dr. K.H. Kuijken
	Universiteit Leiden
	Prof. dr. I.I. Tkachev
	Instituut voor nucleair onderzoek in Moskou
	Dr. J. Vink
	Universiteit van Amsterdam

Contents

Chapter 1

Introduction

1.1 Dark matter in the Universe

It is widely accepted nowadays that about 80% of the total mass in the Universe exists in the form of some mysterious *dark matter*. Unlike the ordinary ("*luminous*" or "*baryonic*") matter, this substance is detected only through its gravitational force (hence the name "*dark*") and plays a dominant role in the dynamics of celestial objects at scales above $\sim 100\,\mathrm{pc}$ (typical size of the smallest galaxies — satellites of the Milky Way). The need for dark matter in explaining the dynamics of galaxies in the Coma cluster was first observed by F. Zwicky [1] in the 1930s (although some earlier results by Hubble suggested that there should be more "dark stars" than visible ones in the Solar neighborhood, see a historical overview in [2]). Since then a body of strong and convincing evidence for the existence of dark matter has emerged (see e.g. [3–5] and references therein). This conclusion has been supported by numerous independent tracers of gravitational potential at different scales:

– the dynamics of stars in galaxies of all types requires a presence of a significant fraction of non-luminous matter (from dwarf spheroidal satellites of the Milky Way, [6] to large ellipticals [7–9]). In contrast, the dynamics of the gravitationally bound systems of a smaller scale (e.g. globular clusters) seem to be explained by its stellar matter (see e.g. [10]);

– measurements of the circular velocity, using e.g. the hyperfine splitting of hydrogen in spiral galaxies [11, 12];

– emission of the hot ionized gas in galaxy groups and galaxy clusters [13, 14];

– both weak and strong gravitational lensing measurements demonstrate that the dynamics of galaxies and galaxy clusters cannot be explained by the Newtonian potential created by visible matter only [5, 15–20].

In addition to this *independent astrophysical evidence* for the existence of dark matter, cosmological data (analysis of the cosmic microwave background anisotropies and the statistics of galaxy number counts) show that the cosmic large scale structure started to develop much before decoupling of photons and baryons at recombination of hydrogen in the early Universe and, therefore, much before ordinary matter could start clustering [21–26]. As a result current body of cosmological data is well-described by the "concordance model" in which about 20% of the total energy density in the Universe is in the form of dark matter (and only about 5% are in the form of baryonic matter).

The relative abundance of baryonic dark matter is strongly constrained by numerous microlensing experiments probing the MAssive Compact Halo Objects (see e.g. [27–29], for an overview see [30] and references therein) and the results of Big Bang Nucleosynthesis [31]. Attempts to explain dark matter by the existence of primordial black holes has not been fully successful (see e.g. [32, 33]).

No attempts to explain the dark matter phenomenon by the modification of Eisteinian gravity and/or Newtonian laws of dynamics has been successful in explaining the dark matter at the cluster and cosmological scales (see the recent discussion in [34, 35], see also [36, 37] for alternative viewpoints).

Therefore, a microscopic origin of dark matter phenomenon (i.e. a new particle or particles) remains the most plausible hypothesis (see e.g. recent review of [38–41] and refs. therein).

1.2   Dark matter and elementary particle physics

To be a viable dark matter candidate particles must be

– stable or cosmologically long-lived;

– 'dark' (very weakly interacting with the electromagnetic radiation);

– produced in the early Universe by a sufficient amount;

– consistent with existing astrophysical and cosmological bounds.

The only electrically neutral and long-lived particle in the Standard Model are neutrinos. As the neutrino oscillation experiments (see e.g. [42] for details) show that neutrinos have mass, they could play the role of dark matter particles. Neutrinos are involved in weak interactions that keep these particles in the early Universe in thermal equilibrium down to the temperatures of a few MeV. At smaller temperatures, the interaction rate of weak reactions drops below the expansion rate of the Universe and neutrinos "freeze out" from the equilibrium. Therefore, a background of relic neutrinos was created just before primordial nucleosynthesis. As interaction strength and, therefore, decoupling temperature and concentration of these particles are known, their present day density is fully defined by the sum of the masses for all neutrino flavors. To constitute the whole dark matter this mass should be about 11.5 eV (see e.g. [43]). Clearly, this mass is in conflict with the existing experimental bounds: measurements of the electron spectrum of β-decay put the combination of neutrino masses below 2 eV [44] while from the cosmological data one can infer an upper bound of the sum of neutrino masses is 0.58 eV at 95% confidence level [21]. The fact that neutrinos could not constitute 100% of dark matter follows also from the study of phase space density of dark-matter dominated objects that should not exceed the density of degenerate Fermi gas: fermionic particles could play the role of dark matter in dwarf galaxies only if their mass is above a few hundred eV (the so-called 'Tremaine-Gunn bound' [45], for review see [46] and references therein) and in galaxies if their mass is above tens of eV. Moreover, as the mass of neutrinos is much smaller than their decoupling temperature, they decouple relativistically and become non-relativistic only deeply in the matter-dominated epoch ("*hot dark matter*"). For such dark matter the history of structure formation would be very different, and the Universe would look rather differently nowadays [26, 47]. All these strong arguments prove convincingly that the *dominant fraction of dark matter* can not be made up of Standard Model neutrinos, and therefore *the Standard Model of elementary particles does not contain a viable dark matter candidate*. Therefore, the dark-matter particle hypothesis necessarily implies an extension of the Standard Model and any resolution of this puzzle will have a profound impact on the development of particle physics. By constraining

the properties of dark-matter particles one can differentiate among extensions of the Standard Model and learn about the fundamental properties of matter.

Phenomenologically, little is known about the properties of dark-matter particles. The mass of fermionic dark matter is limited from below by the 'Tremaine-Gunn bound'[1]. They are not necessarily stable, but their lifetime should significantly exceed the age of the Universe (see e.g. [50]); dark-matter particles should have become non-relativistic sufficiently early in the radiation-dominated epoch (although a sub-dominant fraction might have remained relativistic much later).

A lot of attention has been devoted to the class of dark matter candidates called *weakly interacting massive particles* (WIMPs) (see e.g. [38, 51] for review). These *hypothetical* particles generalize the neutrino dark matter: they also interact with the Standard Model sector with roughly electroweak strength, however their mass is large enough so that these particles become non-relativistic already at decoupling. In this case the present-day density of such particles depends very weakly (logarithmically) on the mass of the particle as long as they are heavy enough. This "universal" density happens to be within an order of magnitude consistent with the dark matter density [52] (the so-called "*WIMP miracle*"). Due to their large mass and interaction strength, the lifetime of these particles would be extremely short and therefore some special symmetry has to be imposed in the model to ensure their stability.

The interest for this class of candidates is due to their potential relation to electroweak symmetry breaking, which is being tested at the Large Hadron Collider in CERN. In many models trying to make the Standard Model "natural" like, for example, supersymmetric extensions of the Standard Model, there are particles that could play the role of WIMP dark matter candidates. The WIMP searches are important scientific goals of many experiments. Dozens of dedicated laboratory experiments are conducted to detect WIMPs in the Galaxy halo by testing their interaction with nucleons (*direct detection experiments*) (see e.g. [53] and refs. therein). In addition, cosmic ray experiments (measurements of antiparticles), as well as γ-ray and X-ray observations are used to search for WIMPs annihilation signal,

---

[1]A much weaker bound, based on the Liouville theorem, can be applied for bosonic dark matter, see e.g. [48, 49].

see e.g. [54, 55] for details. These searches are called, "indirect detection experiments" as only in conjunction with accelerator or laboratory searches they would provide a definitive answer about the properties of the dark-matter particles.

No convincing signals have been observed so far in either "direct" or "indirect" searches. Additionally, no hints of new physics at the electroweak scale has turned up at the Large Hardon Collider (LHC) or in any other experiments. This makes alternative approaches to the dark-matter problem ever more viable.

However, WIMPs by no means exhaust the list of possible dark-matter candidates. Many particles were suggested with their masses ranging from micro-eV to 10^{13} GeV (see e.g. [40, 51]). All these candidates interact *superweakly* (i.e. much weaker than the Fermi interaction strength) with ordinary matter. They may thus be called super-weakly interacting massive particles (or "super-WIMP"). Super-WIMP dark matter particles differ from WIMPs in two crucial ways: *(i)* correct abundance of dark matter may be produced with the mass of dark matter particles as low as a few keV; *(ii)* super-WIMPs can decay into Standard Model particles. These candidates include: extensions of the Standard Model by right-handed neutrinos (sterile neutrinos, majorons) [56–58], axions [59–61], supersymmetric theories (gravitino, axino) [52, 62–69], models with extra dimensions [67] and string-motivated models [70, 71] The feeble interaction strength makes the laboratory detection of such super-weakly interacting dark matter challenging (see e.g. [72]). Fortunately, many super-WIMP particles possess a 2-body radiative decay channel: DM $\rightarrow \gamma + \nu$ (for fermionic dark matter), DM $\rightarrow \gamma + \gamma$ (for dark matter made up of bosons), producing a monochromatic photon with energy $E_\gamma = m_{\mathrm{DM}} c^2 / 2$. Searching for such a line thus provides a major way of detection of super-WIMP dark matter particles. One can therefore search for the presence of such a monochromatic line with energy in the spectra of dark matter-containing objects [73–76].

Although the lifetime of any realistic decaying dark matter should be much longer than the age of the Universe (see e.g. [50]), the huge amount of potentially decaying dark matter particles in a typical halo could produce a sizable decay signal. For example, there are $\sim 10^{75}$ dark matter particles with a ~ 1 keV mass in the halo of Andromeda galaxy. With the lifetime of the order of the age of the Universe, this would lead to $\sim 10^{57}$ decays per

second, releasing $\sim 10^{45}$ erg/s. For comparison, the total X-ray luminosity of the Andromeda galaxy in the 0.1-2.4 keV band is 6 orders of magnitude smaller, $(1.8 \pm 0.3) \times 10^{39}$ erg/s [77], which immediately tells us that the lifetime of such particles should be at least 6 orders of magnitude longer than the age of the Universe.

In summary: the search for decaying dark matter is an important scientific goal. It can provide valuable constraints on the parameter space of extensions to the Standard Model, and may even lead to the discovery of a signal from dark matter particles. Unlike the search for annihilating dark matter (where the WIMP hypothesis limits the range of masses to the GeV energy range), there is no *a priori* preferred energy range for the searches of decaying dark matter signal.

In this thesis, a systematic program of searches for a decaying dark matter signal is conducted. The thesis starts from the identification of the most plausible mass range for decaying dark matter candidates; then discusses possible observational targets and the detection strategy; and, finally, derives new constraints for decaying dark matter, based on the novel method of analysis of observational data.

1.3 Sterile neutrinos: keV-mass decaying dark matter particles

This thesis concentrates mainly on determining the properties of dark matter particles in a *model-independent* fashion. However, it is instructive to consider a *baseline model* with respect to which the results are gauged. Therefore throughout this thesis we apply our results to the case of *sterile neutrino dark matter candidate* [56, 57, 73, 74, 78–81], see [82–84] for review. This model has recently attracted a lot of attention in the particle-physics community. Namely, it was shown that the minimal extension of the Standard Model by three sterile neutrinos provides a viable and unified description of three major "beyond the Standard Model" phenomena in particle physics – dark matter, neutrino oscillations and generation of baryon asymmetry in the Universe. This model, dubbed νMSM, is one of the very few models that provide testable resolution of the "beyond the Standard Model" puzzles in the situation when no new physics is found at the LHC (the so-called "nightmare scenario" [85]), and suggests how the nature of dark mat-
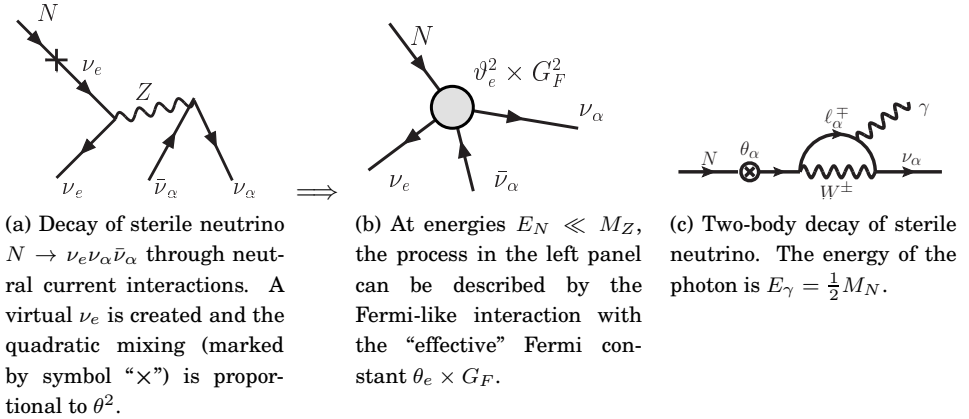
(a) Decay of sterile neutrino $N \to \nu_e \nu_\alpha \bar{\nu}_\alpha$ through neutral current interactions. A virtual ν_e is created and the quadratic mixing (marked by symbol "$\times$") is proportional to θ^2.

(b) At energies $E_N \ll M_Z$, the process in the left panel can be described by the Fermi-like interaction with the "effective" Fermi constant $\theta_e \times G_F$.

(c) Two-body decay of sterile neutrino. The energy of the photon is $E_\gamma = \frac{1}{2} M_N$.

Figure 1.1: Example of interactions of a sterile neutrino: decay $N \to \nu_e \nu_\alpha \bar{\nu}_\alpha$ (panel (a)) and its effective Fermi-like description (panel (b)) and loop-mediated decay $N \to \gamma + \nu_\alpha$ (panel (c)).

ter and other "beyond the Standard Model" phenomena may nevertheless be checked experimentally using existing experimental technologies and major infrastructure. Below, we describe it in more details.

A sterile neutrino is a right-chiral counterpart of the left-chiral neutrinos of the Standard Model (called '*active*' neutrinos in this context). Adding these particles to the Standard Model Lagrangian makes neutrinos massive, and therefore their existence provides a simple and natural explanation of the observed neutrino flavor oscillations. These particles are *singlet leptons* because they carry no charges with respect to the Standard Model gauge groups (hence the name), and therefore along with their Yukawa interaction with the active neutrinos (='Dirac mass') they can have a Majorana mass term (see e.g. [76] for details). They interact with matter via the creation of a virtual active neutrino (quadratic *mixing*), and in this way they effectively participate in weak reactions (see e.g. Fig. 1.1a). At energies much below the masses of the W and Z-bosons, their interaction can be described by the analog of the Fermi theory with the Fermi coupling constant G_F suppressed by the *active-sterile neutrino mixing angle* θ — the ratio of their Dirac to Majorana masses (Fig. 1.1b):

$$\theta_\alpha^2 = \sum_{\text{sterile N}} \left| \frac{m_{\text{Dirac}, \alpha}}{M_{\text{Majorana}}} \right|^2 \tag{1.1}$$

(this mixing can be different for different flavours α).

It was observed long ago that such particles could have been produced in the Early Universe through mixing with active neutrinos [56] and have a correct relic density for any mass [56, 78, 79, 81, 86–88].

Unlike WIMPs whose existence is motivated first of all by the theoretical considerations on the stability of the Higgs mass against quantum corrections that could require a fine-tuning of parameters of the model, the existence of sterile neutrinos is motivated by the *observational phenomena beyond the Standard Model*. Namely, sterile neutrinos would provide a simple and natural explanations of the *neutrino flavour oscillations* [89–92]. However, a *single* sterile neutrino would be unable to explain the two observed mass splittings between Standard Model neutrinos — at least two sterile neutrinos are needed for that. Moreover, should a sterile neutrino play the role of dark matter, the mixing with active neutrinos would be too small to contribute significantly to the flavor oscillations – its lifetime should be very large and, therefore, interaction strength should be too feeble [57, 93]. Therefore, in order to explain dark matter and neutrino mass (one for each Standard Model flavor), the minimal model should contain 3 right-handed neutrinos [57]. In such a model, the lowest mass eigenstate of the active neutrinos will be (almost) zero and the sum of neutrino masses $\sum m_\nu \approx \kappa \sqrt{|\Delta m_{\mathrm{atm}}^2|}$, where $\kappa = 1$ or 2 for normal (inverted) hierarchy [93]. This is one of the predictions of such a model.

In spite of the fact that a dark-matter sterile neutrino plays essentially no role in the neutrino oscillations, the fact that 3 particles are needed to explain *both* dark matter and neutrino oscillations is crucial. As we will see below, primordial properties of sterile neutrino dark matter are determined by two other sterile neutrinos.

If the masses of the two sterile neutrinos, responsible for neutrino oscillations, are below $\sim 2\,\mathrm{GeV}$ (mass of c-quark), such particles can be searched with existing experimental techniques [94, 95]. This is a unique situation when one can directly test the nature of neutrino oscillations in 'intensity frontier' [96] experiments. For masses above $2\,\mathrm{GeV}$ the searches become more difficult.

It turns out that in the mass region between $100\,\mathrm{MeV}$ and the electroweak scale, out-of equilibrium reactions with these two sterile neutrinos are capable of generating the observed matter-antimatter asymmetry of the

Universe (baryogenesis) [80, 97]. These observations motivated a lot of recent efforts for developing the νMSM — *Neutrino Minimal Standard Model* (see [82] for review). Finding these particles in intensity frontier experiments would provide an unparalleled possibility to test baryogenesis in the laboratory. Moreover, if some particles are found in such experiments it will be possible not only to check whether they are responsible for baryogenesis or not, but also unambiguously predict the properties of sterile neutrino dark matter.

Because its interaction with the Standard Model particles is very feeble, sterile neutrino does not need to be stable. The decay channel for sterile neutrinos of all masses is to 3 (anti)neutrinos (Fig. 1.1a).[2] However, the most characteristic feature of sterile neutrino dark matter is its ability to decay into a photon and a neutrino (with cosmologically long lifetime) [73, 74, 98], see Fig. 1.1c. The emitted photon is almost mono-energetic (the width of the dark matter decay line is determined entirely by the motion of dark matter particles). Although the lifetime of the dark matter particles turns out to be *much longer than the age of the Universe*, the humongous number of these particles around us implies that the combined emission may be sizable.

If dark matter is made of sterile neutrinos, detecting astrophysical signal from their decay (the "indirect detection") may be the only way to identify this particle experimentally. However, it may be possible to prove the dark matter origin of observed signal unambiguously using its characteristic properties.

In summary: three sterile neutrinos with the masses below electroweak scale form a minimal testable model that provides a unified description of three major *observational* problems "beyond-the-Standard-Model" [57, 80, 82, 97]:

1) neutrino flavour oscillations;
2) the absence of primordial anti-matter in the Universe;
3) existence of dark matter.

---

[2]For masses above $1 \, \mathrm{MeV}$ additional decay channels become kinematically possible.

1.3.1 Production of sterile neutrinos in the early Universe

The active-sterile neutrino mixing is strongly suppressed at temperatures above a few hundred MeV and peaks roughly at [56]

$$T_{peak} \sim 130 \left(\frac{M_{N_{\text{DM}}}}{1 \, \text{keV}} \right)^{1/3} \text{MeV} , \qquad (1.2)$$

Sterile neutrino dark-matter candidates are *never in thermal equilibrium* and their number density is significantly smaller than that of the active neutrinos (that is why they can account for the observed dark matter abundance without violating the 'Tremaine-Gunn bound'). In particular, the shape of the primordial momentum distribution of the sterile neutrinos is roughly proportional to that of the active neutrinos [73]:

$$f_{N_{\text{DM}}}(t,p) = \frac{\chi}{e^{p/T_\nu(t)} + 1} , \qquad (1.3)$$

where the normalization $\chi \sim \theta_{\text{DM}}^2 \ll 1$ and where $T_\nu(t)$ is the temperature of the active neutrinos.[3] Comparing the production temperatures Eq. (1.2) of dark matter sterile neutrinos with their masses shows that they are produced relativistically in the radiation-dominated epoch. Indeed, for the primordial dark matter distribution of the form (1.3) one has $\langle p \rangle \sim T_{peak} \gtrsim M_{N_{\text{DM}}}$ for $M_{N_{\text{DM}}} \lesssim 40 \, \text{GeV}$. Relativistic particles stream out of the overdense regions and erase primordial density fluctuations at scales below the *free-streaming horizon* (FSH) – particles' horizon where they becomes nonrelativistic (for a detailed discussion of characteristic scales see e.g. [99] and references therein). This effect influences the formation of structures. If dark matter particles decouple nonrelativistically (*cold* dark matter models, CDM) the structure formation occurs in a "bottom-up" manner: specifically, smaller scale objects form first and then merge into the larger ones [100]. CDM models fit modern cosmological data well. In the case of particles, produced relativistically and *remaining relativistic* into the matter-dominated epoch (i.e. *hot* dark matter, HDM), the structure formation goes in a "top-down" fashion [101], where the first structures to collapse have sizes comparable to the Hubble size [102–104]. The HDM scenarios contradict large-scale structure (LSS) observations [47]. Sterile neutrino dark matter that

---

[3]The true distribution of sterile neutrinos is in fact colder than that shown in Eq. (1.3). Specifically, the maximum of $p^2 f_{N_1}(p)$ occurs at $p/T_\nu \approx 1.5 - 1.8$ (depending on $M_{N_{\text{DM}}}$), as compared with $p \approx 2.2 T_\nu$ for the case shown in Eq. (1.3) [81, 86].

is produced relativistically and is then redshifted to nonrelativistic velocities in the radiation-dominated epoch is an intermediate, *warm dark matter* (WDM) candidate [73, 79, 105]. Structure formation in WDM models is similar to that in CDM models at distances above the free streaming scale. Below this scale density fluctuations are suppressed, compared with the CDM case. The free-streaming scale can be estimated as [103]

$$\lambda_{\mathrm{FS}}^{co} \sim 1\,\mathrm{Mpc} \left(\frac{\mathrm{keV}}{M_{N_{\mathrm{DM}}}} \right) \frac{\langle p_N \rangle}{\langle p_\nu \rangle}\,. \tag{1.4}$$

where $1\,\mathrm{Mpc}$ is the (comoving) horizon at the time when momentum of active neutrinos $\langle p_\nu \rangle \sim 1\,\mathrm{keV}$. If the spectrum of sterile neutrinos is nonthermal, then the moment of non-relativistic transition and $\lambda_{\mathrm{FS}}^{co}$ is shifted by $\langle p_N \rangle / \langle p_\nu \rangle$.

This mechanism specifies a *minimal* amount of sterile neutrinos that will be produced for given M_1 and θ_1. The requirement that 100% of dark matter be produced via such mixing places an *upper bound* on the mixing angle θ_1 for a given mass. This conclusion can only be affected by entropy dilution arising from the decay of some heavy particles below the temperatures given in Eq. (1.2) [106, 107].

The production of sterile neutrino dark matter may substantially change in the presence of lepton asymmetry when the resonant production (*RP*) of sterile neutrinos [78] occurs, analogous to the Mikheyev–Smirnov–Wolfenstein effect [108, 109]. When the dispersion relations for active and sterile neutrinos cross each other at some momentum p, the effective transfer of an excess of active neutrinos (or antineutrinos) to the population of dark matter sterile neutrinos occurs. The maximal amount of sterile neutrino dark matter that can be produced in such a way is limited by the value of lepton asymmetry, $\eta_L \equiv |n_\nu - n_{\bar\nu}|/s$, where s is the entropy of relativistic species in plasma. The present dark matter abundance $\Omega_{\mathrm{DM}} \sim 0.25$ translates into the requirement of $\eta_L \sim 10^{-6} \left(\frac{\mathrm{keV}}{M_{N_{\mathrm{DM}}}} \right)$ in order for resonnatly produced sterile neutrinos to constitute the dominant fraction of dark matter. One notices that the resonant production occurs only for values of lepton asymmetry, η_L much larger than the *measured* value of *baryon asymmetry of the Universe*: $\eta_B \equiv \frac{n_B}{s} \sim 10^{-10}$ [21]. Such a value of η_L does not contradict to any observations though. Indeed, the upper bounds on η_L are based on either primordial nucleosynthesis (BBN) or CMB measurements (as chemical potential of neutrinos would carry extra radiation density) [110, 111]. These bounds

read $|\eta_L| \lesssim$ few $\times 10^{-3}$ (see e.g. [112–114]). We see, therefore, that the lepton asymmetry, required for resonant sterile neutrino production is still considerably smaller than the upper limit. Notice, that at epochs prior to BBN even $\eta_L \sim 1$ is possible (if this lepton asymmetry disappears later). Such a scenario is realized e.g. in the *Neutrino Minimal Standard Model*, νMSM (see [82] for review), where the lepton asymmetry keeps being generated below the sphaleron freeze-out temperature and may reach $\eta_L \sim 10^{-2} \div 10^{-1}$ before it disappears at $T \sim$ few GeV [87].

1.3.2   Structure formation with sterile neutrino dark matter

Non-negligible velocities of 'warm' sterile neutrinos alter the power spectrum of density fluctuations at scales below the *free-streaming horizon* scale. Additionally, the suppression of the halo mass function below a certain scale [115] and different history of formation of first structures affects the way the first stars were formed and therefore the reionization history of the Universe, abundance of the oldest (*Population III*) stars, etc. [116–121].

The effects of suppression of the matter power spectrum are probed with the **Lyman-α forest method** [122–125] (see [99] for critical overview of the method and up-to-date bounds). Using neutral hydrogen as a tracer of overall matter overdensity, one can reconstruct the power spectrum of density fluctuations at redshifts $2 < z < 5$ and scales $0.3 - 5$ h/Mpc (in comoving coordinates) by analyzing Lyman-α absorption features in the spectra of distant quasars.

If all dark matter is made of sterile neutrinos with a simple Fermi-Dirac-like spectrum of primordial velocities (1.3), the matter power spectrum has a sharp (cut-off like) suppression (as compared to ΛCDM) at scales below the free-streaming horizon (1.4) (similar to the case of 'thermal relics' [105]). In this case the Lyman-α forest data [99, 122–126] puts such strong constraints at their free-streaming length, which can be expressed as the *lower bound* on their mass $M_{N_{\rm DM}} \geq 8$ keV (at 3σ CL) [99]. Such WDM models produce essentially no observable changes in the Galactic structures (see e.g. [99, 127–130]) and therefore, from the observational point of view such a sterile neutrino dark matter (although formally 'warm') would be indistinguishable from pure CDM.

On the other hand, resonantly produced sterile neutrinos have spectra that significantly differ from those in the non-resonant case [78, 88]. The

primordial velocity distribution of RP sterile neutrinos contains narrow resonant (*cold*) *plus* a nonresonant (*warm*) components – CWDM model (see [99, 131] for details).[4] In the CWDM case, however, Lyman-α constraints allow a significant fraction of dark matter particles to be very warm [99]. This result implies for example, that sterile neutrino with the mass as low as $1-2$ keV is consistent with all cosmological data [131].

The first results [133] demonstrate that resonantly produced sterile neutrino dark matter, compatible with the Lyman-α bounds [131], do change the number of substructure of a Galaxy-size halo and their properties. Qualitatively, structures form in these models in a bottom-up fashion (similar to CDM). The way the scales are suppressed in CWDM models is more complicated (and in general less severe for the same masses of WDM particles), as comparable with pure warm dark matter models. The first results of [133] demonstrate that the resonantly produced sterile neutrino dark matter models, compatible with the Lyman-α bounds of [131], do change the number of substructure of a Galaxy-size halo and their properties. The discrepancy between the number of observed substructures with small masses and those predicted by ΛCDM models (first pointed out in [134, 135]) can simply mean that these substructures did not confine gas and are therefore completely dark (see e.g. [136–139]). This is not true for larger objects. In particular, CDM numerical simulations invariably predict several satellites "too big" to be masked by galaxy formation processes, in contradiction with observations [134, 135, 140, 141]. Resonantly produced sterile neutrino dark matter with its non-trivial velocity dispersion, turns out to be "warm enough" to amend these issues [133] (and "cold enough" to be in agreement with Lyman-α bounds [131]).

Ultimate investigation of the influence of *dark matter decays* and of *modifications in the evolution of large scale structure* in the 'sterile neutrino Universe' as compared with the ΛCDM model requires a **holistic approach**, where all aspects of the systems are examined within the same set-up rather than studying the influence of different features one-by-one. Potentially observable effects of particles' free streaming and decays are expected in terms of

– formation and nature of the first stars [117, 118, 142, 143];

– reionization of the Universe [119, 121, 144–146];

---

[4]Axino and gravitino models may have similar spectra of primordial velocities, c.f. [132].

- the structure of the intergalactic medium as probed by the Lyman-α forest [99, 124–126, 131, 147–149];
- the structure of dark matter haloes as probed by gravitational lensing [149–153];
- the structure and concentration of haloes of satellite galaxies [133, 154–157].

The results of this analysis will be confronted with measured cosmological observables, using various methods: Lyman-α analysis (with BOSS/SDSS-III or X-Shooter/VLT [158]), statistics and structure of dark matter halos, gravitational lensing, cosmological surveys).

The weak lensing surveys can be used to probe further clustering properties of dark matter particles as sub-galactic scales, as the next generation of these surveys will be able to measure the matter power spectrum at scales down to $1-10$ h/Mpc with a few percent accuracy. The next generation of lensing surveys (such as e.g. KiDS, LSST, WFIRST, Euclid) can provide sensitivity, compatible with the existing Lyman-α bounds [150, 151]. As in the case of the Lyman-α forest method the main challenge for the weak lensing is to properly take into account baryonic effects on matter power spectrum. The suppression of power spectrum due to primordial dark matter velocities can be extremely challenging to disentangle from the modification of the matter power spectrum due to baryonic feedback [148, 159, 160]. Finally, the modified concentration mass relation, predicted in the CWDM models, including those of resonantly produced sterile neutrinos ([131, 161]) can be probed with the weak lensing surveys (see e.g. [162, 163]) if their sensitivity can be pushed to halo masses below roughly $10^{12} M_\odot$.

1.4   The structure of the thesis

I. We begin in Chapter 2 with the *determination of the lower bound on the mass of dark matter particles* and the energy range of possible searches. If the dark matter particles are fermions, there is a very robust bound on their mass. Namely, due to the Pauli exclusion principle, there exists the densest "packing" of the fermions in a given region of the phase space (known as *"Tremaine-Gunn bound"*, [45]). Decreasing the mass of the dark matter particles, one increases their number (and, hence, phase-space density) in any dark matter-dominated object. The requirement that this phase-space

density did not exceed that of the degenerate Fermi gas thus leads to the *lower mass bound*. With additional assumptions, this bound can be further strengthened (and even generalized to the case of bosonic dark matter). We overview existing approaches and their limitations and propose a new method that allows to derive strong yet robust bounds on the mass of dark matter particles, improving on the original Tremaine-Gunn bound. By considering the existing data on different types of galaxies, we conclude that the strongest bound on the mass of dark matter fermions comes from the dwarf satellite galaxies of the Milky Way. Using recent results of the mass modeling of dwarf spheroidal galaxies and paying special attention to systematic uncertainties in relevant parameters, it is shown that the mass of dark matter fermion should exceed ∼0.4 keV, and therefore the dark matter decay signal should be searched in X-ray and γ-ray energy ranges. As the decay width increases with the mass of the particle, *we conclude that the X-ray range is the preferred range of searches for fermionic decaying dark matter*.

II. We proceed with the identication of the best observational targets for decaying dark matter searches (Chapter 3). To this end we analyze dark matter distributions in several hundreds of dark matter-dominated objects in the local Universe (redshift $z < 0.1$). We consider different types of galaxies (dwarf, spiral, and elliptical); galaxy groups and galaxy clusters – all types of dark matter-dominated objects, with their masses spanning eight orders of magnitude. We demonstrate that the expected dark matter decay signal (proportional to the "*dark matter column density*") increases slowly with the mass of the object. We determine a relation between the dark matter column density and the mass of the halo and demonstrate that the *scatter of this relation* can be predicted based on the existing numerical simulations of structure formation. Therefore, decaying dark matter would produce a unique all-sky signal, with a known slow-varying angular distribution. Such a signal can be easily distinguished from any possible astrophysical background and therefore makes the astrophysical search for decaying dark matter *another type of a direct detection experiment*.

III. These results allows us to define a *detection strategy for radiatively decaying dark matter* (Chapter 4). First of all, one has a freedom of choosing the observational targets, avoiding complicated astrophysical backgrounds. In particular, although galaxy clusters possess in general the highest dark matter column density, due to their high emission in X-rays the expected

signal to noise ratio is not optimal (for spectral resolution of modern X-ray missions). The best targets thus become dwarf and spiral galaxies. The expected decay signal from these targets varies within a factor of few and although lower, than that of the galaxy clusters can be searched for against much lower astrophysical background.

Our findings also demonstrate that if a candidate spectral line is found, its surface brightness profile may be measured, distinguished from astrophysical emissions, and compared among several objects with similar expected signal. This allows to *unambiguously* discriminate decaying dark matter signal from possible astrophysical or instrumental backgrounds. To illustrate the power of this approach, we investigate the recent claim of that a spectral feature at ~ 2.5 keV in the *Chandra* observation of Willman 1 can be interpreted a dark matter decay line. We demonstrate that such an interpretation is ruled out by archival observations of M31 and Fornax/Sculptor dwarf spheroidals with high significance.

We conclude Chapter 4 with the review of the current status of decaying dark matter searches. We collect all existing bounds on decaying dark matter lifetime in the keV energy range. These results are obtained from the analysis of medium exposure (about 100 kilo-seconds) observations of individual objects of different types. We argue that with the current generation of X-ray telescopes there are two possible ways to further improve the existing bounds and probe the theoretically interesting regions of particle physics models:

(a) Deep (few mega-secounds) observations of the most X-ray quiet objects. "*Classical*" dwarf spheroidal galaxies (Ursa Minor, Draco, Sculptor, Fornax), where the dark matter content can be determined robustly are the preferred targets. The problem with this approach is the limited visibility of some of these objects and large investment (about 10%) of the annual observational time of the satellite (total observational time available each year for *XMM-Newton* and *Chandra* satellites is about half of the calendar year, i.e. 14–15 Msec). Allocating time for such an observation in the absence of a candidate line is hardly possible. On the other hand, observations of these objects would provide an important confirmation of the signal, detected with some other means.

(b) Total exposure of all observations of dark matter-dominated objects with the X-ray satellites is several orders of magnitude longer than any pos-

sible single observation. Therefore a possible way to advance with the existing X-ray instruments is *to combine a large number* of X-ray observations of different dark matter-dominated objects. The idea is that the spectral position of the dark matter decay line is the same for all these observations, while the astrophysical backgrounds in the combined spectrum would "average out", producing a smooth continuum against which a small line would become visible. Naively, such a dataset, uniformly processed, should allow to improve the existing bounds by at least an order of magnitude *and* study spatial dependence of each candidate line.

IV. Chapter 5 is devoted to this goal – *analysis of a large dataset of archival XMM-Newton observations of galaxies*. Extremely large combined exposure of this dataset (two orders of magnitude longer than a typical single observation) presents several new challenges. Indeed, large number of counts in each energy bin mean that the statistical errors become very small (sub-% level). To extract meaningful bounds one needs therefore to control systematic errors at the comparable level. The level of systematics of the *XMM-Newton* is considered to be much higher (5-10%) due to the instrument's degradation with time, variability of the instrumental background, imperfect knowledge of the instrument's response functions, etc. To tackle these problems, a novel method of data analysis has been developed that delivers the required control over the level of systematics. We demonstrate the sensitivity of this method and search for the presence of lines in the 2.5–11 keV energy range. We find several new line candidates. After careful analysis, all these candidates are quantified as faint instrumental lines which have not been observed previously. Finally, we construct strongest to-date upper bounds on decaying dark matter parameters probing significant part of the parameter space of the corresponding particle physics models.

V. We conclude Chapter 6 with the discussion of the prospects of searching for decaying dark matter line with new instruments. The real progress requires at least an order of magnitude improvement of energy resolution for diffuse sources, combined with the high throughput instruments. We argue therefore that the X-ray micro-calorimeters (rather than present-day CCD-based detectors) should be used for this goal. Such a micro-calorimeter delivers required spectral resolution in the energy range from sub-keV to tens of keV. Parameters of such a mission and its tentative observational programme is discussed.

Chapter 2

Mass of the dark matter particles

2.1   Introduction

In this Chapter we discuss the lower bounds on the mass of dark matter particles, coming from the analysis of dark matter phase-space distribution in different types of dark matter dominated objects.

If the dark matter particles are fermions, there is a very robust bound on their mass. Namely, due to the Pauli exclusion principle, there exists the densest "packing" of the fermions in a given region of the phase space [45]. Decreasing the mass of dark matter particles, one increases their number in a given gravitationally bound object, containing dark matter. The requirement that the phase-space density of the dark matter does not exceed that of the degenerate Fermi gas leads to the *lower mass bound*. A weaker version of the same bound can be generalized for the bosonic dark matter as well. We review the existing approaches, and concentrate on two methods of deriving such a bound. The first (model-independent) approach uses the information about the *observed* matter distribution only and applies to any type of fermionic dark matter. The second method also requires an assumption about the initial (primordial) distributions of dark matter velocities. Stronger, model-dependent bounds are quoted for several dark matter models (thermal relics, non-resonantly and resonantly produced sterile neutrinos, etc.). These latter bounds rely on the assumption that baryonic feedback cannot significantly increase the maximum of a distribution function of dark matter particles. It turns out that the strongest bound comes from the objects with the largest phase-space density – dwarf spheroidal galaxies (dSphs). We discuss the ob-

servational data on dSphs as well as astronomical uncertainties in relevant parameters.

While these considerations are very generic and rely almost exclusively on such fundamental properties of dynamical systems like Liouville theorem, they provide important restrictions on possible particle physics models. For example, applying these considerations to the case of neutrino dark matter would rule out the possibility that massive neutrinos constitute the dominant fraction of dark matter in the Universe (the lower bound of their mass would imply that the $\Omega_{\mathrm{DM}} \ll 1$). For the scenario in which all the dark matter is made of sterile neutrinos produced via non-resonant mixing with the active neutrinos (NRP) this gives $m_{\mathrm{NRP}} > 1.7 \ \mathrm{keV}/c^2$. Combining these results in their most conservative form with the X-ray bounds of dark matter decay lines, we conclude that the non-resonant production scenario remains allowed in a very narrow parameter window only. This conclusion is independent of the results of the Lyman-α analysis. The dark matter model in which sterile neutrinos are resonantly produced in the presence of lepton asymmetry remains viable. Within the minimal neutrino extension of the Standard Model (the νMSM), both mass and the mixing angle of the dark matter sterile neutrino are bounded from above and below, which suggests the possibility for its experimental search.

This Chapter is organized as follows. After an overview of the original Tremaine-Gunn bound and its modifications (Section 2.2), we introduce the concept of maximal coarse-graining and propose a conservative modification of the original bound (Section 2.3). In Section 2.4 we analyze existing observational data on Milky Way and Andromeda galaxies, galaxy groups and Milky Way satellite dSphs and use it to determine the phase-space density of these objects. Special attention is paid to systematic uncertainties of measured values. Our results are summarized in Section 2.6.

2.2   Dark matter mass limits

Consider a spherically symmetric dark matter-dominated object with the mass M within the region R. One can obtain the lower bound m_{DEG} on the dark matter mass by demanding that the maximal (Fermi) velocity of the degenerate fermionic gravitating gas of mass M in the volume $\frac{4}{3}\pi R^3$ does

not exceed the escape velocity $v_\infty = \left(\frac{2G_N M}{R}\right)^{1/2}$:

$$\hbar \left(\frac{9\pi M}{2gm_{\mathrm{DEG}}^4 R^3}\right)^{1/3} \leq \sqrt{\frac{2G_N M}{R}} \Rightarrow m_{\mathrm{DEG}}^4 \geq \frac{9\pi\hbar^3}{4\sqrt{2}gM^{1/2}R^{3/2}G_N^{3/2}}. \qquad (2.1)$$

Here and below g denotes the number of internal degrees of freedom of dark matter particles, and G_N is the Newton's constant. Such a consideration, applied to various dark matter dominated objects, leads to the mass bound, which we will call m_{DEG} in what follows (see Table 2.4 below).[1]

The above considerations assume that the dSphs are *purely spherical* systems. Analysis of [166] shows that ellipticity of stars in dSphs vary from $0.22^{+0.18}_{-0.22}$ for Leo IV to 0.80 ± 0.04 for Ursa Major I. Simulated dark matter halos on the other hand tend to have rather moderate ellipticity, $\epsilon_{\mathrm{DM}} \lesssim 0.32$ [167].[2] According to Section 2.5, the ellipticity of dark matter halos can lower the resulting limit on m_{DEG} by $\lesssim 10\%$.

The limit, obtained in such a way, is very robust, as it is independent of the details of the formation history of the system. The only uncertainties associated with it are those of astronomical nature: systematic errors in the determination of velocity and density distribution. All these issues will be discussed below (Section 2.4, 2.3).

For particular dark matter models (with the known primordial velocity dispersion) and under certain assumptions about the evolution of the system which led to the observed final state, this limit can be strengthened [45, 46, 48, 49, 157, 168–173]. The argument is based on the *Liouville's theorem* (see e.g. [168, 174]) and assumes that the collapse of the system is disipation-less and collisionless. The Liouville theorem states that the phase-space distribution function $f(t, x, v)$ does not change in the course of disipationless collisionless dynamics. The consequence of the Liouville theorem is that the function $f(t, x, v)$ "moves" in the phase-space, according to the Hamiltonian flow, and therefore its maximum (over the phase space) remains unchanged. Therefore, if one could determine the characteristics of a phase-space distribution function from astronomically observed quantities (in the first place

---

[1]The spatially homogeneous dark matter distribution is only an approximation. In reality one should consider self-gravitating degenerate fermionic gas. It is possible to show that, under some external conditions, the system of weakly interating fermions undergoes a first-orger phase transition to a nearly degenerate "fermion star" [164]. The existence of such objects may also have insteresting astrophysical applications [165].

[2]Therefore it is hard to explain the ellipticity of stars in the most elongated dSphs, see the discussion in [166].

average density $\bar{\rho}$ and velocity dispersion σ) in dSphs (or any other dark matter dominated objects), the Liouville theorem would allow to connect the measured values with the primordial properties of dark matter particles.

One such characteristics of the phase-space distribution is its *maximum*. Any physical measurement can probe only the phase-space distribution, averaged over some phase-space region – a *coarse-grained* phase-space density (phase-space density) (as opposed to exact or *fine-grained* phase-space density). Such a coarse-grained phase-space density, averaged over phase-space cells $\Delta\Pi(x, v)$ centered around points (x, v) in the phase space, is defined via

$$\bar{f}(t, x, v) = \frac{1}{\text{vol}(\Delta\Pi)} \int\limits_{\Delta\Pi(x,v)} d\Pi' \, f(t, x', v') \qquad (2.2)$$

(here $\text{vol}(\Delta\Pi)$ is the volume of the phase-space cell). From the definition (2.2) it is clear that the maximal (over the whole phase space) value of the coarse-grained phase-space density $\bar{f}_{max}(t)$ cannot exceed the maximal value of the corresponding fine-grained phase-space density. On the other hand, as a consequence of the Liouville theorem, the maximum of the fine-grained phase-space density f_{max} does not change in time. Thus, one arrives to the following inequality

$$\bar{f}_{max}(t) \leq f_{max} . \qquad (2.3)$$

The inequality (2.3) allows to relate the properties of dark matter at present time t with its primordial properties, encoded in f_{max}. For example, if one assumes that initially dark matter particles possess relativistic Fermi-Dirac distribution function with some temperature T_{FD} (relativistically decoupled thermal relics):

$$f_{\text{FD}}(p) = \frac{g}{(2\pi\hbar)^3} \frac{1}{e^{p/T_{\text{FD}}} + 1} \qquad (2.4)$$

and recovers from astronomical measurements that in the final state the coarse-grained phase-space density of the system is described by the isothermal sphere (see e.g. [174]) with a core radius r_c and a 1D velocity dispersion σ, whose maximum is given by

$$\bar{f}_{iso,max} = \frac{9\sigma^2}{4\pi G_N (2\pi\sigma^2)^{3/2} r_c^2} \qquad (2.5)$$

the comparison of the maximum of the coarse-grained phase-space density (2.5) with its primordial (fine-grained) value leads to the so-called Tremaine-

Gunn mass bound [45]:

$$m_{\mathrm{FD}} \geq m_{\mathrm{TG}}, \quad \text{where} \quad m_{\mathrm{TG}}^4 \equiv \frac{9(2\pi\hbar)^3}{(2\pi)^{5/2} g G_N \sigma\, r_c^2}. \tag{2.6}$$

For the case of initial distribution (2.4) this bound is stronger than the one, based on the Pauli exclusion principle, by a factor $2^{1/4}$ [45]. For different primordial dark matter distributions this difference can be significant (as we demonstrate later). We would like to stress, though, that these stronger bounds make assumptions about the evolution of phase-space density, while the one, based on the Pauli exclusion principle does not assume anything about either primordial velocity distribution of the particles, or the formation history of the observed object and simply compares measured phase-space density with the maximally allowed for fermions.

Another characteristics of the phase-space distribution function is the "average phase-space density"

$$Q \equiv \frac{\bar{\rho}}{\langle v^2 \rangle^{3/2}}, \tag{2.7}$$

introduced in [175, 176]. The value of Q_f (average phase-space density today) is simply defined in terms of the observed quantities $\bar{\rho}$ and $\langle v^2 \rangle = 3\sigma^2$ and therefore serves as a convenient estimator of the phase-space density for any dark matter dominated object. One can calculate primordial Q_i for an arbitrary homogeneous distribution function $f(p)$

$$Q_i = \frac{g\, m^4}{(2\pi\hbar)^3} \frac{\left(\int f(p) d^3 p \right)^{5/2}}{\left(\int f(p) p^2 d^3 p \right)^{3/2}} \tag{2.8}$$

and compare it with its value today Q_f. It was claimed in [175, 176] that **Q** cannot increase during the evolution of dark matter:

$$Q_i \geq Q_f. \tag{2.9}$$

Applying this inequality to the dSphs, one obtains several times stronger mass bound, than that of [45].

To illustrate the origin of the inequality (2.9), authors of [175, 176] noticed that in the case of the *uniform monoatomic ideal gas*, **Q** is related to the usual thermodynamic entropy per particle (see Appendix 8.2.1.1) and the

inequality for **Q** becomes a consequence of the second law of thermodynamics. Indeed, in this case one can see that

$$\frac{S[f]}{N} = -\log\left(\frac{Q(\bar{\rho},\sigma)\hbar^3}{m^4}\right) + \log C[f] \,, \qquad (2.10)$$

where in the right hand side of (2.10) functional $C[f]$ does not depend on the average density and velocity of the dark matter particles.

However, because of the long-range interaction of dark matter particles, the notion of Boltzmann entropy is well-defined only for the primordial dark matter distribution and not for the final state of dark matter evolution (see e.g. the discussion in [177]). Moreover, we will show below that in general *the increase of entropy does not imply the decrease of* Q. Indeed, the values of $C[f]$ are different for different types of phase-space distributions f and therefore they can change with time if the shape of the (coarse-grained) distribution changes. Namely, even if initial (i) and final (f) states both satisfy relation (2.10) between the entropy and **Q** ($S_{i,f} = \log C_{i,f} - \log \frac{Q_{i,f}\hbar^3}{m_{\text{DM}}^4}$) from the second law of thermodynamics

$$S_f \geq S_i \qquad (2.11)$$

it only follows that

$$Q_i \geq Q_f \frac{C_i}{C_f} \,. \qquad (2.12)$$

Therefore, in general, the inequality (2.9) does not follow from entropic considerations.

Moreover, the simple relation (2.10) between the entropy and **Q** does not hold for the distributions we are interested in. For example, for the Fermi-Dirac distribution (2.4) one has:

$$\frac{S}{N} = \text{const}\,\frac{m_{\text{FD}}^4}{Q\hbar^3} \qquad (2.13)$$

(see Appendix 8.2.1.3 for details). The relation becomes even more complicated, if one considers dark matter candidates (e.g., sterile neutrinos, gravitinos), which are produced out of thermal equilibrium. In general, when the primordial distribution function depends on several parameters, both **Q** and entropy are expressed through these parameters in a non-trivial way and the simple relation (2.10) does not hold. For example, this is the case when dark matter is produces in two stages and the dark matter distribution

shape has two components: colder and warmer one. Physically interesting examples include: production of sterile neutrino in the presence of lepton asymmetry [78, 87, 88]; production of gravitino thermally at high temperatures (see e.g. [178, 179]) accompanied by non-thermal production via late decays of next-to-lightest supersymmetric particles (see e.g. [180]).

Keeping in mind the above considerations, one might be tempted to use the entropy of the system as an estimator of phase-space density and utilize the entropy increase (2.11) instead of the inequality on Q to put a lower bound on the dark matter mass. However, unlike Q, which by definition is expressed solely in terms of measured quantities $\bar{\rho}$ and σ, the inequality (2.11) requires the knowledge of the phase-space distribution function in the final state (e.g. to determine the C_f in the right-hand side of Eq. (2.10) or, more generally to express the entropy of the final state in terms of the observed quantities). This information cannot be simply deduced from astronomical observations. One possible way to formulate a conservative, robust inequality would be to find the *maximal* possible entropy for a given system with measured macroscopic parameters. However, it was shown in [168, 174, 181, 182] that such a maximum does not exist. Namely, for a gravitating system which usually consists of a compact core and a widely dispersed halo of finite mass, the total Boltzmann entropy of the system goes to infinity when the halo becomes infinite. Physically, the measured density and velocity dispersion characterize the inner part of the object. The astronomical observations do not usually probe the outskirts of gravitating systems (such as dSphs) and phase-space distributions (such as (2.5)) do not describe them properly. On the other hand, to compare with the homogenous initial system having a primordial velocity spectrum, we need to know an entropy of the *whole* system. The large (and unknown!) fraction of this entropy can be related to the outskirts. The entropy of the gravitating system depends on the precise state of the halo.

As a result, *it is not possible to construct a simple and robust limit, using entropy considerations*.

2.3 Maximal coarse-graining

In view of the above arguments, to derive a conservative mass bound, in this work we will follow the original approach of Tremaine and Gunn [45] with

some modification.

An important advantage of this approach is that the maximum of the phase space density is likely to be located in the inner, dense part of an object. Therefore, under this reasonable assumption, the results *do not depend* on the dark matter distribution in the outskirts (see the discussion above).

As discussed already, the coarse-grained phase-space distribution in the final state cannot be measured directly, and one has to make assumptions to deduce its maximum. A conservative way to minimize this uncertainty is to use the "maximally coarse-grained distribution". It is based on a simple fact that the mean value of a function, averaged over an arbitrary region cannot exceed its maximal value. Therefore, the average value of coarse-grained phase space density in a large phase-space volume can be taken as a conservative estimate of the $\bar{F}_{max}$, independent on assumptions about the actual form of phase-space distribution.

To this end we consider an (approximately spherically symmetric) gravitating system (having in mind a dwarf spheroidal galaxy), that has the mass $M(R)$ confined within the radius R. The phase-space volume, occupied by the dark matter particles, forming such a system can be approximated by

$$\Pi_\infty = \left(\frac{4}{3}\pi\right)^2 R^3 v_\infty^3 \ , \tag{2.14}$$

where we have introduced *escape velocity* v_∞. The "coarsest" phase-space density is such that the averaging (2.2) goes over the whole phase-space volume: $\Delta\Pi = \Pi_\infty$:

$$\bar{F} = \frac{M}{\Pi_\infty} = \frac{9}{16\pi^2}\frac{M}{R^3 v_\infty^3} = \frac{3\bar{\rho}}{4\pi v_\infty^3} \tag{2.15}$$

As an estimate for R we take *half-light radius* r_h (i.e. the radius where surface brightness profile falls to 1/2 of its maximal value). Neglecting possible influence of ellipticity of stellar orbits (c.f. Section 2.5), assuming constant dark matter density within r_h and isothermal distribution of stars [183], we obtain the following estimate on the average dark matter density within r_h:

$$\bar{\rho} = \frac{3\log 2}{2\pi}\frac{\sigma^2}{G_N r_h^2}, \tag{2.16}$$

Assuming isotropic velocity distributions,[3] the escape velocity v_∞ of the dark matter particles is related to the velocity dispersion σ via $v_\infty \simeq \sqrt{6}\sigma$. In such

---

[3]This assumption seems to be correct for the dark matter particles, since numerical simu-

a way we obtain the averaged phase-space density $\bar{F}$:

$$\bar{F} = \frac{M}{\Pi_\infty} = \frac{\bar{\rho}}{8\pi\sqrt{6}\sigma^3} \approx \frac{3\log 2}{16\sqrt{6}\pi^2 G_N \sigma r_h^2} \approx \qquad (2.17)$$

$$\approx 1.25 \frac{M_\odot}{\text{pc}^3}\left(\frac{\text{km}}{\text{sec}}\right)^{-3}\left(\frac{\text{km/sec}}{\sigma}\right)\left(\frac{1\,\text{pc}}{r_h}\right)^2 ,$$

which coincides with its maximal value (being flat).

As a consequence of Eq. (2.3), this "coarse-grained" phase-space density $\bar{F}$ is smaller than the f_{max} – the maximum value of fine-grained phase-space density, equal to its primordial value:

$$\bar{F} \leq f_{max} . \qquad (2.18)$$

Eq. (2.18) relates the observed properties of the dark matter-dominated systems (l.h.s.) with the microscopic quantity on the r.h.s. of inequality, which depends on the production mechanism of the dark matter.

We are mostly interested in two types of primordial momentum distribution. One is the relativistic Fermi-Dirac (2.4) with its f_{max} being equal to

$$f_{max,\text{FD}} = \frac{g\,m_{\text{FD}}^4}{2(2\pi\hbar)^3} \qquad (2.19)$$

(we fix the overall normalization of the phase-space distribution function by the relation $M = \int d^3x\,d^3v\,f(t,x,v)$, where M is the total mass of the system). Another one is an (approximate) form of the momentum distribution for sterile neutrinos, produced via non-resonant oscillations with the active ones [56, 73]. For the latter case we consider the velocity dispersion to be[4]

$$f_{\text{NRP}}(p) = \frac{g\chi}{e^{p/T_\nu} + 1} . \qquad (2.20)$$

---

lations of dark matter structures of different scales show that the velocity anisotropy $\beta(r) \equiv 1 - \frac{\sigma_\theta^2 + \sigma_\phi^2}{2\sigma_r^2}$ tends to be zero towards the central region [184–188]. It is not clear whether β equals to zero for stars in dSphs. The assumption of isotropy of stellar velocities leads to the *cored* density profiles [189, 190], therefore our estimate for $\bar{\rho}$ tends to be robust. This is confirmed by comparison of the estimate (2.16) with those, based on [191–193], where dark matter density profiles were obtained under the assumptions of different anisotropic distributions of stars in dSphs.

[4]In reality the momentum distribution in the case of non-resonant production does not have thermal shape. The exact shape, taking into account contributions from primeval plasma at temperatures around QCD transition, can be computed only numerically [81, 86]. The difference between the exact distribution and (2.20) does not exceed 20%, which does not affect the mass bounds.

Chapter 2. Mass of the dark matter particles

The normalization constant χ is proportional to the mixing strength between active and sterile neutrinos and T_ν is the temperature of neutrino background $T_\nu(z) = (1+z)T_{\nu_0}$, related to the temperature of the cosmic microwave background today via $T_{\nu_0} = (4/11)^{1/3}T_{\text{CMB},0}$. For the maximal value of distribution (2.20) we find

$$f_{max,\text{NRP}} = \frac{g\chi m_{\text{NRP}}^4}{2(2\pi\hbar)^3} \ . \tag{2.21}$$

From the definition (2.20) one can relate the normalization factor $g\chi$ to the dark matter abundance (see e.g. [122])

$$\omega_{\text{DM}} \equiv \Omega_{\text{DM}}h^2 = g\chi\frac{m_{\text{NRP}}[\text{eV}]}{94\ \text{eV}}. \tag{2.22}$$

Therefore we can rewrite maximal value of the primordial phase-space density (2.22) as

$$f_{max,\text{NRP}} = \frac{94\omega_{\text{DM}}}{2(2\pi\hbar)^3}\frac{m_{\text{NRP}}^3}{\text{eV}^3} \ . \tag{2.23}$$

Notice, that unlike the Fermi-Dirac case, for the non-resonant production scenario f_{max} behaves as the *third* power of particle's mass.

In the presence of lepton asymmetry in primeval plasma the resonant production of sterile neutrinos becomes possible [78]. A possible lepton asymmetry, generated in the framework of the νMSM and spectra of sterile neutrino dark matter were recently computed in [87, 88]. Qualitatively, these spectra contain a "cold" (resonant) component and a "warm" one, produced through non-resonant oscillations, analogously to the non-resonant production scenario of [56]. The spectra as a whole become colder than in the non-resonant production case (see e.g. Fig. 6 in [88]). The maxima of primordial phase-space distributions for these spectra are higher (sometimes significantly) than for spectra, produced in the non-resonant production scenario (c.f. Fig. 5 in [88]). Therefore, in general mass bound for such a dark matter is expected to be weaker than that of the non-resonant production scenario. The exact form of these spectra can be computed only numerically. We used a number of spectra to check those which satisfy the bound (2.18) or TG bound (see Section 2.6).

Let us compare expression (2.17) with the original Tremaine-Gunn bound (maximum of the right hand side of Eq. (2.6)):

$$F_{\text{TG}} = \frac{9}{8\pi^2\sqrt{2\pi}G_N\sigma r_c^2} \ . \tag{2.24}$$
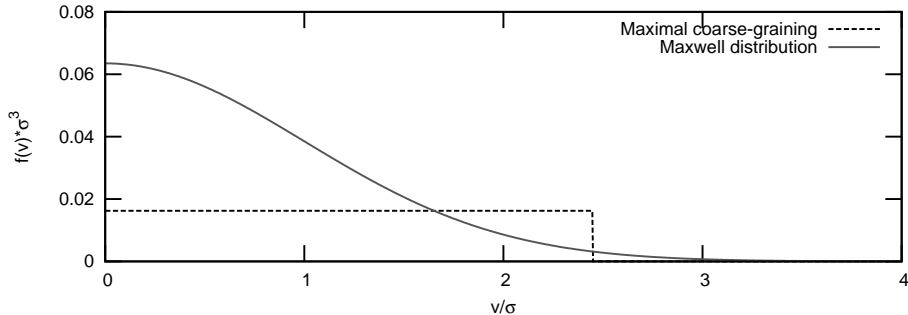
Figure 2.1: Comparison of velocity profiles assumed in [45] (grey solid line) and in this work (black dashed line).

The values of $\bar{F}$ is smaller than F_{TG} by

$$\frac{\bar{F}}{F_{\text{TG}}} = \frac{\log 2\sqrt{\pi}}{6\sqrt{3}} \left(\frac{r_c}{r_h}\right)^2 \approx 0.118 \left(\frac{r_c}{r_h}\right)^2 , \qquad (2.25)$$

where r_c and r_h are the core radius of isothermal profile and the half-light radius, correspondingly. When comparing $\bar{F}$ and F_{TG} below, we take $r_h \simeq r_c$. Essentially, the difference between $\bar{F}$ and F_{TG} is due to the different assumed velocity distributions. While the Maxwell distribution was assumed in [45] (c.f. Eq. (2.5)), we assume constant velocity profile from escape velocity v_∞ down to $v = 0$ (as shown on the Fig. 2.1). The numerical factor in (2.25) is the ratio of areas under two velocity curves of Fig. 2.1. Translated into the mass bound, relation (2.25) means that for dark matter particles with distribution (2.4) one would obtain roughly 40% stronger mass bound by using the original Tremaine-Gunn bound, rather than $\bar{F}$ (and $\approx 60\%$ stronger mass bound for the case of the distribution (2.20)).

Let us compare our new bound with the one, based of [175, 176]. Following the definition (2.7), we express the measured value Q_f for a dSph through the observed quantities

$$Q = \frac{\bar{\rho}}{\eta^3 (3\sigma^2)^{3/2}} \approx 14.83 \frac{M_\odot}{\text{pc}^3} \left(\frac{\text{km}}{\text{sec}}\right)^{-3} \left(\frac{\text{km sec}^{-1}}{\sigma}\right) \left(\frac{1\,\text{pc}}{r_h}\right)^2 \frac{1}{\eta^3} , \qquad (2.26)$$

where η is the scaling factor which accounts for the fact that the dark matter particles do not necessarily have the same velocity dispersion as the stars, r_h is the half-light radius, σ is the measured one-dimensional velocity dispersion of the stars and $\bar{\rho}$ is defined in (2.16). It was estimated in [176]

that $\eta \approx 1$. In Eq. (2.26) we used the same value of $\bar{\rho}$ as in Eq. (2.17). For the same dSph, Q_f is bigger than $\bar{F}$ (given by expression (2.17)) by a factor $8\pi\sqrt{2}/3 \approx 11.85\ldots$.

On the other hand, for any initial momentum distribution $f(p)$ we should compare Q_i, given by Eq. (2.8), with the $f_{max}^{(i)}$. For both types of distribution (2.4) and (2.20) the ratio of initial Q_i/f_{max}^i is given by

$$\frac{Q_i}{f_{max}^{(i)}} = \frac{4\pi\zeta^{5/2}(3)}{5\sqrt{15}\zeta^{3/2}(5)} \approx 0.973\ldots \qquad (2.27)$$

As a result, a bound, based on the decrease of the average phase-space density Q is stronger than $\bar{F}$ bound from the same object by a factor:

$$\frac{f_{max}^{(i)}}{Q_i}\frac{Q_f}{\bar{F}} \approx 12.176\ldots \qquad (2.28)$$

(where again we put $\eta = 1$). This leads to ≈ 1.87 times stronger bound on the m_{FD} and ≈ 2.3 times stronger bound for m_{NRP}.

2.4 Analysis of measured values

In this Section we estimate phase-space density in different dark matter-dominated objects. We demonstrate that the dwarf spheroidal satellites of the Milky Way possess the highest phase-space density and thus provide the strongest limits on the mass of dark matter particles.

2.4.1 Galaxies

In this Section we study the restrictions on the mass of dark matter particles, coming from the analysis of the phase-space density of spiral galaxies. The distribution of dark matter is modeled based the analysis of the *rotational curves* — dependence of the circular rotational velocity of stars (optical data) and neutral hydrogen (radio data) around the galaxy centre as a function of distance (for mass modeling of the Milky Way, see e.g. [194, 195], for Andromeda galaxy – [11, 12]). Well outside the galactic bulge where the circular velocity curve flattens, the dark matter density can be found with the help of the following relation

$$\bar{\rho}_{gal} = \frac{3}{4\pi G_N}\frac{v_h^2(r)}{r^2}, \qquad (2.29)$$

where $v_h(r)$ – part of the rotational velocity, contributed to dark matter [5] at distance r from the galaxy centre and is (approximately) constant. The velocity of dark matter particles in a compact halo does not exceed $v_\infty = \sqrt{2}v_h^{max}$. Here v_h^{max} is the maximum of the rotation curve, reached at some radius r_{max} before starting to decline. However, there are only few objects (classical dSphs) for which the value of v_h^{max} and r_{max} had been measured, see e.g. [196]). Therefore determination of these values provides the strongest uncertainty in the evaluation of the phase-space density of dark matter in spiral galaxies.

We write the phase-space density estimate as (see also (2.15))

$$\bar{F}_{gal} = \frac{3\bar{\rho}_{gal}}{4v_\infty^3} = \frac{9}{32\pi^2\sqrt{2}G_N v_h(r_{gal})r_{gal}^2}, \tag{2.30}$$

where r_{gal} is the *inner* radius of the halo, some proxy for r_{max}. To be conservative we use r_{gal}, where the dark matter contribution is equal to contribution from barionic matter (the sum of bulge and disk components).

For the subsequent analysis we used two spiral galaxies with the best studied haloes – Milky Way and Andromeda galaxy. The velocity profiles for these galaxies are shown, e.g., in [194, 197]. The results for r_{gal} and $v_h(r_{gal})$, as well as the obtained bounds for $\bar{F}$ are shown in Table 2.1.

The average value of the lower mass bound from Table 2.1 implies $m_{\rm DEG} > 34\text{eV}$, $m_{\rm FD} > 40\text{eV}$. As we will see in Sec. 2.4.3 below, it is much weaker compared to bound obtained from dwarf spheroidal galaxies. Therefore, if the dSph dynamics (in contrast to dynamics of spiral galaxies) is *not* due to dark matter, the lower mass bound in the dark matter particles is ~ 40 eV, depending on the dark matter species.

2.4.2 Galaxy groups

The dark matter profiles in galaxy groups are obtained from the analysis of X-ray thermal emission distribution from tha hot gas halo. In this paper, we used the data from [198], where the distributions of dark matter, baryonic matter in galaxies and hot integralactic gas are derived. Similar to previous subsection, to take into account the uncertainties of dark matter and hot gas

---

[5]Note that this velocity is somewhat lower than the total rotational velocity of stars around the galaxy centre. This is due to the presence of two additional components – disk and buldge – formed by the luminous matter.

Profile (1)	Ref. (2)	r_{gal} kpc (3)	$v(r_{gal})$ km/sec (4)	$\bar{F}_{gal}, M_\odot\times$ pc^{-3} (km/sec)$^{-3}$ (5)	m_{DEG} keV (6)	m_{FD} keV (7)
MW, A1	[194]	3.0±0.6	150±10	3.45 ×10^{-9}	0.043	0.051
M31, C1	[194]	3.8±0.8	180±10	1.79 ×10^{-9}	0.036	0.043
M31a	[197]	6.0±1.2	140±10	0.93 ×10^{-9}	0.031	0.037
M31b	[197]	6.5±1.3	140±10	0.79 ×10^{-9}	0.030	0.035
M31c	[197]	6.0±1.2	150±10	0.86 ×10^{-9}	0.030	0.036

Table 2.1: Parameters of selected spiral galaxies from [194, 197] (columns 1-5) and obtained lower mass bounds for different dark matter types (columns 6-7). m_{DEG} denotes the model-independent bound coming from Pauli principle (2.1), m_{FD} – model-dependent bound for dark matter particles with momentum distribution (2.4).

distribution we use the phase-space density values calculated in r_{gr}, where dark matter mass $M_{gr} = M(r_{gr})$ starts to dominate over the barionic mass. The maximal velocity of dark matter particles is estimated as

$$v_\infty = \sqrt{\frac{2G_N M_{gr}}{r_{gr}}}, \tag{2.31}$$

from what (using (2.15)) we obtain the conservative estimate of the maximal phase-space density value,

$$\bar{F}_{gr} = \frac{9}{32\sqrt{2}\pi^2 G_N^3/2 M_{gr}^1/2 r_{gr}^{3/2}}. \tag{2.32}$$

The results are presented in Table 2.2. The averaged values of the mass bound, derived from Table 2.2 are $m_{\text{DEG}} > 24$ eV, $m_{\text{FD}} > 29$ eV. Therefore, if the dSph dynamics, in contrast to dymamics of spiral galaxies and galaxy groups, is not due to dark matter, the lower bounds on the dark matter particle mass is ~ 25-30 eV, depending on the dark matter model.

2.4.3   Dwarf spheroidal galaxies

Dwarf spheroidal galaxies (dSphs) are the compact (around ~ 1 kpc) and gravitationally bound systems with low surface brightness and high velocity dispersion. To explain the latter, one needs to introduce the mass-to-luminosity value with is hundreds times more than the value observed in

Object (1)	Ref. (2)	M_{gr} $10^{10} M_\odot$ (3)	r_{gr} kpc (4)	$\bar{F}_{gr}, M_\odot \times$ pc^{-3} (km/sec)$^{-3}$ (5)	$m_{\rm DEG}$ keV (6)	$m_{\rm FD}$ keV (7)
Abell 262	[198]	6.5±0.7	6.5±1.7	5.34 ×10^{-10}	0.027	0.032
NGC 533	[198]	5.0±0.5	5.0±1.5	9.02 ×10^{-10}	0.031	0.037
MKW 4	[198]	25±3	12.0±3.6	1.08 ×10^{-10}	0.018	0.022
IC 1860	[198]	13±1	9.5±2.9	2.14 ×10^{-10}	0.021	0.026

Table 2.2: Parameters of chosen galaxy groups from [198] (columns 1-5) and obtained lower mass bounds for different dark matter types (columns 6-7). $m_{\rm DEG}$ denotes the model-independent bound coming from Pauli principle (2.1), $m_{\rm FD}$ – model-dependent bound for dark matter particles with momentum distribution (2.4).

usual galaxies (see, for example, [199]). The possible reason for such a huge velocity dispersion is the disturbance of the cental part of dSphs with the tidal forces of our Galaxy. However, the observable features of tidal disturbance – the so-called "tidal tails", formed from stars which is going out of dSph – were found in single dSphs (Sagitarius, Ursa Major II). Therefore, the most realistic model by the moment for a *majority* of dSphs is their domination with dark matter. As a result, it is assumed that the dSphs are the *most compact* objects dominated with dark matter.

Over the last several years, a number of very faint, very dense dSphs were detected [200–206]. To calculate the mass limits, we used the data from two papers [205, 206] in which the dark matter phase-space density was estimated. First of all, we should notice that although both of these papers provide the estimate of Q for each object, they use different prescriptions for computing this value.

In [205] the quantity Q is estimated inside the half-light radius r_h, using one-dimensional velocity dispersion σ of stars:

$$Q_{Gil} = \frac{\bar{\rho}}{\sigma^3} = \frac{3}{8\pi G_N r_h^2 \sigma} \ . \tag{2.33}$$

Compared to our definition (2.17) $\bar{F} = \frac{\log 2}{2\sqrt{6\pi}} Q_{Gil} \approx 0.045 Q_{Gil}$. Following [207] the authors of [206] define *central density*

$$\rho_0 = 166 \sigma^2 \eta^2 / r_c^2 \tag{2.34}$$

where $\eta \sim 1$ is a numerical parameter, characterizing plausible density pro-

Galaxy	r_h, Plummer	r_h, exponential
Coma Berenices	5.0'	5.9'
Canes Venatici II	3.0'	3.3'
Leo IV	3.3'	3.4'
Hercules	8.0'	8.4'

Table 2.3: Uncertainties of determination of half-light radius r_h for several dSphs.

files (for details see [206, 207]). They used ρ_0 to define the quantity:

$$Q_{SG} \equiv \frac{\rho_0}{\sigma^3} \,, \tag{2.35}$$

As a result for the same object Q_{SG} is by a factor of 14.60 greater than Q_{Gil}.

Using the available information about dSph galaxies (refs. [205, 206] and refs. therein), we calculate $\bar{F}$, trying also to estimate the errors. Several factors contribute to the errors of σ and r_h.

First of all, as σ is the dispersion of measured velocities, it has the statistical error (which can be quite large for the ultra-faint dSphs where the number of stars can be rather small ($\sim 10-100$, c.f. [206, Table 3]). However, the systematic error is much larger. The authors of [206] found the systematic error on their determination of velocity dispersion to be $2.2\,\mathrm{km/sec}$. We add this error in quadratures to the statistical errors, found in [206, Table 3]. The results are shown in the column number 4 in the Table 2.4.

The half-light radius r_h is a derived quantity and there are several contributions to its errors. First of all, the surface brightness profile is measured in angular units and their conversion to parsecs requires the knowledge of the distance towards the object. These distances are generally known with uncertainties of about 10% (see [199, 199, 200, 203, 208–217]). Another uncertainty comes from the method of determination of r_h. The surface brightness profile gets fit to various models to determine this quantity. For several dSphs: Coma Berenices, Canes Venatici II, Hercules and Leo IV authors used two different profiles (Plummer and exponential) for evaluating the annular half-light radius [200]. Their results are present in the Table 2.3. We use these results to estimate the systematic error on r_h to be 20% and use it for all the dSph, where r_h is quoted without errors. The results of determination r_h are shown in the 3rd column of the Table 2.4. The obtained values of $\bar{F}$ with corresponding errors are presented in the Table 2.4, column

5. We determined the errors on $\bar{F}$ by pushing the uncertainties in both σ and r_h so that the values of $\bar{F}$ is minimized (maximized).

2.5 Influence of aspherical shapes of dark matter halos

In this Section we analyze how the bound changes due to the deviation of a dark matter halo from a spherical shape. Such asphericity affects both the spatial volume V and the escape velocity v_∞. We consider the dSph as homogeneous ellipsoid with semi-axes a, b and c and assume the ellipticity of its 2D projection[6] $\epsilon \lesssim 0.5$. Because we observe only 2D projection of such an ellipsoid, there are two possibilities:

Prolate dSph: $c > b \simeq a$. We see the axes b and c, related to the "averaged" radius R via $b = R(1 - \epsilon)^{1/2}, c = R(1 - \epsilon)^{-1/2}$. The spatial volume V is therefore

$$V = \frac{4}{3}\pi abc \approx \frac{4}{3}\pi R^3 (1 - \epsilon)^{1/2} \approx \frac{4}{3}\pi R^3 (1 - 0.5\epsilon). \qquad (2.36)$$

The gravitational potential for $\epsilon \lesssim 0.5$ is dominated by monopole and quadrupole components,

$$\phi \approx \phi^{(0)} + \phi^{(2)}. \qquad (2.37)$$

The maximal value of the potential occurs near the end of the minor semi-axis:

$$|\phi_{max}| \equiv \frac{v_\infty^2}{2} = \frac{G_N M}{a} - \frac{G_N D_{zz}}{4a^3}, \qquad (2.38)$$

where $D_{zz} = \frac{2M(c^2 - a^2)}{5}$ – the quadrupole moment of the system [218]. For $\epsilon \ll 1$ we then obtain

$$\frac{V v_\infty^3|_{prolate}}{V v_\infty^3|_{spherical}} \approx 1 + 0.05\epsilon, \qquad (2.39)$$

which gives us the correction for m_{DEG} of smaller than 1% (for $\epsilon = 0.5$).

---

[6]Throughout this paper, we define the *ellipticity* ϵ in a way similar to that in [174] (see also [166]), i.e. $\epsilon \equiv 1 - b/a$, where a and b are the *semi-major* and *semi-minor* axis, respectively. Thus, the case of $\epsilon = 0.5$ corresponds to axis ratio 1:2.

Oblate dSph: $c \simeq b > a$. We observe the axes a and c, therefore the spatial volume V changes by $(1 - \epsilon)^{-1/2} \approx 1 + 0.5\epsilon$. The maximum of the gravitational potential is then given by

$$|\phi_{max}| \approx \frac{G_N M}{a} + \frac{G_N D_{xx}}{2a^3} \approx \frac{G_N M}{R}(1 + 0.1\epsilon). \qquad (2.40)$$

where D_{xx} is given by the same expression, as D_{zz} above. The maximal phase-space volume changes in the oblate case by $\approx 1 + 0.65\epsilon$, so the correction for m_{DEG} will constitute about 8% for $\epsilon \simeq 0.5$.

Thus, the departure from spherical symmetry for dark matter halos of dSphs changes the limit on m_{DEG} by less than $\lesssim 10\%$ for the case of axis ratio 1:2. This uncertainty is below several others, therefore, we will consider dSphs to be spherical in what follows.

dSph	References	r_h pc	σ km/s	$\bar{F}$ $M_\odot/(pc^3(km/s)^3)$	$m_{\rm DEG}$ keV/c^2	$m_{\rm FD}$ keV/c^2	$m_{\rm NRP}$ keV/c^2	$m_{\rm NRP,TG}$ keV/c^2
(1)	(2)	(3)	(4)	(5)	(6)	(7)	(8)	(9)
dSphs from [205]								
Sextans	[199, 205]	630±170	6.6±2.3	$4.78^{+8.97}_{-2.58}\cdot10^{-7}$	$0.147^{+0.044}_{-0.026}$	$0.174^{+0.053}_{-0.031}$	$0.454^{+0.192}_{-0.104}$	$0.715^{+0.302}_{-0.163}$
Fornax	[199, 205]	400±103	10.5±2.7	$7.45^{+10.74}_{-3.70}\cdot10^{-7}$	$0.164^{+0.041}_{-0.026}$	$0.195^{+0.049}_{-0.031}$	$0.527^{+0.183}_{-0.108}$	$0.830^{+0.288}_{-0.170}$
Leo I	[199, 205]	330±106	8.8±2.4	$1.31^{+2.59}_{-0.72}\cdot10^{-6}$	$0.189^{+0.059}_{-0.034}$	$0.224^{+0.070}_{-0.041}$	$0.635^{+0.279}_{-0.148}$	$1.00^{+0.44}_{-0.23}$
UrsaMinor	[199, 205]	300±74	9.3±2.8	$1.49^{+2.27}_{-0.76}\cdot10^{-6}$	$0.195^{+0.051}_{-0.031}$	$0.232^{+0.060}_{-0.037}$	$0.665^{+0.240}_{-0.139}$	$1.05^{+0.38}_{-0.23}$
Carina	[199, 205]	290±72	6.8±1.6	$2.19^{+2.87}_{-1.05}\cdot10^{-6}$	$0.215^{+0.050}_{-0.039}$	$0.255^{+0.060}_{-0.039}$	$0.755^{+0.243}_{-0.148}$	$1.19^{+0.38}_{-0.23}$
Draco	[166, 205]	221±16	9.5±1.6	$2.70^{+1.07}_{-0.69}\cdot10^{-6}$	$0.226^{+0.020}_{-0.016}$	$0.269^{+0.023}_{-0.019}$	$0.809^{+0.095}_{-0.076}$	$1.27^{+0.15}_{-0.12}$
Bootes	[199, 204, 219]	246±28	$6.5^{+2.1}_{-1.3}$	$3.18^{+1.88}_{-1.24}\cdot10^{-6}$	$0.236^{+0.029}_{-0.027}$	$0.280^{+0.035}_{-0.033}$	$0.855^{+0.143}_{-0.130}$	$1.35^{+0.23}_{-0.20}$
Sculptor	[199, 205]	160±40	10.1±0.3	$4.99^{+3.62}_{-1.98}\cdot10^{-6}$	$0.264^{+0.038}_{-0.031}$	$0.314^{+0.046}_{-0.037}$	$0.993^{+0.198}_{-0.154}$	$1.56^{+0.312}_{-0.243}$
Leo II	[199, 205]	185±48	6.8±0.7	$5.38^{+5.55}_{-2.30}\cdot10^{-6}$	$0.269^{+0.052}_{-0.035}$	$0.319^{+0.062}_{-0.042}$	$1.02^{+0.27}_{-0.17}$	$1.60^{+0.43}_{-0.27}$
dSphs from [206]								
Canes Venatici I	[166, 206]	564±36	7.6±2.2	$5.17^{+3.46}_{-1.63}\cdot10^{-7}$	$0.150^{+0.020}_{-0.013}$	$0.178^{+0.024}_{-0.016}$	$0.467^{+0.087}_{-0.055}$	$0.735^{+0.137}_{-0.087}$
Ursa Major I	[166, 206]	318^{+50}_{-39}	7.6±2.4	$1.63^{+1.46}_{-0.70}\cdot10^{-6}$	$0.199^{+0.035}_{-0.026}$	$0.237^{+0.041}_{-0.031}$	$0.684^{+0.163}_{-0.118}$	$1.08^{+0.26}_{-0.19}$
Hercules	[166, 206]	330^{+75}_{-52}	5.1±2.4	$2.25^{+3.74}_{-1.28}\cdot10^{-6}$	$0.216^{+0.060}_{-0.041}$	$0.257^{+0.071}_{-0.049}$	$0.762^{+0.294}_{-0.187}$	$1.20^{+0.46}_{-0.29}$
Leo T	[166, 206]	178±39	7.5±2.7	$5.26^{+8.22}_{-2.66}\cdot10^{-6}$	$0.267^{+0.071}_{-0.043}$	$0.318^{+0.084}_{-0.051}$	$1.01^{+0.37}_{-0.21}$	$1.59^{+0.59}_{-0.33}$
Ursa Major II[7]	[166, 206]	140±25	6.7±2.6	$9.53^{+13.55}_{-4.59}\cdot10^{-6}$	$0.310^{+0.077}_{-0.047}$	$0.369^{+0.091}_{-0.056}$	$1.23^{+0.42}_{-0.24}$	$1.94^{+0.67}_{-0.38}$
Leo IV	[166, 206]	116^{+26}_{-34}	3.3±2.8	$2.82^{+34.39}_{-1.91}\cdot10^{-5}$	$0.406^{+0.368}_{-0.100}$	$0.483^{+0.438}_{-0.119}$	$1.77^{+2.41}_{-0.55}$	$2.79^{+3.80}_{-0.87}$
Coma Berenices	[166, 206]	77±10	4.6±2.3	$4.59^{+7.53}_{-2.19}\cdot10^{-5}$	$0.459^{+0.126}_{-0.069}$	$0.546^{+0.150}_{-0.082}$	$2.08^{+0.80}_{-0.41}$	$3.28^{+1.25}_{-0.64}$
Canes Venatici II	[166, 206]	74^{+14}_{-10}	4.6±2.4	$4.97^{+8.92}_{-2.66}\cdot10^{-5}$	$0.468^{+0.137}_{-0.082}$	$0.557^{+0.163}_{-0.097}$	$2.14^{+0.87}_{-0.48}$	$3.36^{+1.38}_{-0.76}$

Table 2.4: Parameters for dSphs from [205, 206] (columns 1–5) and derived lower mass limits for various types of dark matter (columns 6–9). $m_{\rm DEG}$ refers to the limit from Pauli exclusion principle (2.1), $m_{\rm FD}$ is the limit for particles with the momentum distribution (2.4), $m_{\rm NRP}$ and $m_{\rm NRP,TG}$ – for distribution (2.20). All results are quoted for $g = 2$ internal degrees of freedom. Results for non-resonant production scenario are for $\omega_{\rm DM} = 0.105$ [220].

2.6 Results

Our main results are compiled into the Table 2.4 (columns 6–9). The **column 6** of Table 2.4 contains the bound on m_{DEG} (given by Eq. (2.1)) based on the Pauli exclusion principle. It is independent of the details of the evolution of the system, is not affected by the presence of baryons (see below) and holds for any fermionic dark matter. The **column 7** contains the mass bounds for the relativistically decoupled dark matter particles (primordial distribution (2.4)), obtained by combining Eqs.(2.17)–(2.19). **Columns 8** and **9** are discussed below, Section 2.6.1.

   We quote all the mass bounds with the corresponding uncertainties, coming from those of in determination of σ and r_h (see Section 2.4). However, for any given object there can be unique reasons, violating the standard assumptions and therefore increasing the uncertainties. Therefore, although the strongest bounds in Table 2.4 come from the Canes Venatici II dSph, we decided to take a value which independently follows from several objects as a single number, characterizing our results (for a given type of dark matter). To this end we choose the value, obtained for Leo IV.[8] Thus, the mass bounds, quoted below are excluded from three dSphs: Leo IV, Canes Venatici II and Coma Berenices [9]. To summarize, we obtain the following model independent lower bound, applicable to *any type of fermionic dark matter*:

$$m_{\mathrm{DEG}} > 0.41 \,\mathrm{keV}/c^2 \;, \tag{2.41}$$

   If instead we assume that dark matter in the form of "*relativistic thermal relics*" with the Fermi-Dirac distribution, the bound becomes

$$m_{\mathrm{FD}} > 0.48 \,\mathrm{keV}/c^2 \;, \tag{2.42}$$

   Notice, that we chose not to use the bounds, based on the "average phase-space density" Q [175, 176] (see discussion in the Section 2.2). However, as this bound is widely used in the literature, we quote analogs of lower

---

[8]Notice, that the numbers for Leo IV essentially coincide with the mass limits from Canes Venatici II and Coma Berenices if all uncertainties in these dSphs are pushed to *minimize* the mass bound.

[9]It is possible that Coma Berenices is undergoing tidal disruption (like another ultra-faint dSph, Ursa Major II , closely resembling Coma Berenices) [206]. However, unlike Ursa Major II (or the best known example of tidally disrupted dSph, Sagittarius), there are no known tidal streams near the position of Coma Berenices and the evidence in favor of tidal disruption are quite moderate (c.f. discussion in Sec. 3.6 of [206]).

limits (2.42) and (2.44) based on inequality (2.9) (which we denote $m_{\text{FD,HD}}$ and $m_{\text{NRP,HD}}$ correspondingly):

$$m_{\text{FD,HD}} = 0.9 \, \text{keV}/c^2 \, ,$$
$$m_{\text{NRP,HD}} = 4.0 \, \text{keV}/c^2 \, .$$

(2.43)

For details see Appendix 8.2.2.

2.6.1   Implication for sterile neutrino dark matter

In this Section we consider implications of our results for sterile neutrino dark matter. For sterile neutrinos, produced through non-resonant mixing with the active neutrinos ("*NRP production*" [56, 79, 81]). Combining Eqs. (2.17), (2.18) and (2.23) one obtains the result for the case of dark matter with primordial velocity distribution (2.20), quoted in the **column 8**. Both bounds in columns 7 and 8 conservatively assume maximally coarse-grained distribution function (see Section 2.3). In instead of the maximal coarse-graining, one assumes the isothermal distribution in the final state (c.f. Fig. 2.1), one arrives to the original Tremaine-Gunn bound, shown in the **9th column**. It is obtained by comparing the expressions (2.21) with (2.24).[10] We denote the corresponding mass bound by $m_{\text{NRP,TG}}$.

$$m_{\text{NRP}} > 1.77 \, \text{keV}/c^2 \, ,$$

(2.44)

and

$$m_{\text{NRP,TG}} > 2.79 \, \text{keV}/c^2 \, .$$

(2.45)

We can compare lower bounds (2.44)–(2.45) with the upper ones, coming from astrophysical (X-ray) constraints on the possible flux from sterile neutrino dark matter decay [221–231]. Taking central value (2.44) and comparing it with the X-ray constraints, one sees that there exists a narrow window of parameters for which 100% of dark matter can be made from the non-resonant produced sterile neutrino (c.f. Fig. 2.2). Less conservative bound (2.45), based on [45] (marked by the dark orange double-dotted vertical line on the Fig. 2.2) almost completely closes this window. Notice, that these bounds are comparable with the lower mass limit $m_{\text{NRP}} > 5.6 \, \text{keV}/c^2$, coming from the Ly-$\alpha$ forest analysis of [126].

---

[10]The value of r_c is not currently known for several new, faint dSphs, from which we obtain the best limits on dark matter mass. Therefore, to calculate the Tremaine-Gunn limit in Table 2.4, we use the conservative estimate $r_c \approx r_h$ (see comment after Eq.(2.25)).
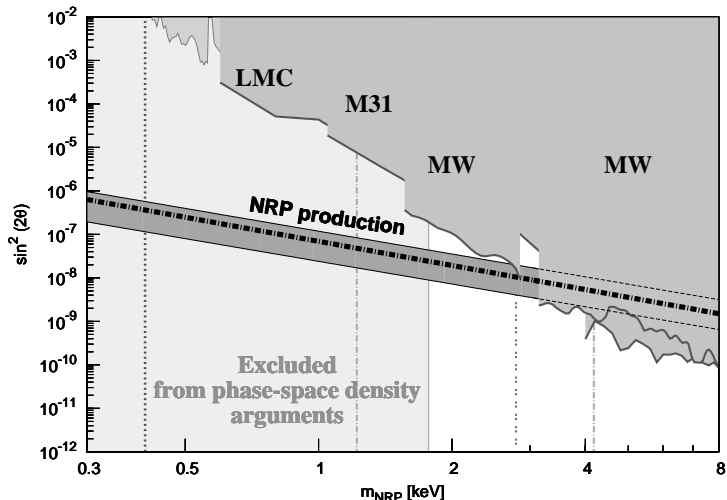
Figure 2.2: Restrictions on parameters of sterile neutrino (mass and mixing $\sin^2(2\theta)$ between sterile and active neutrinos) from X-rays ([223, 228–231]) and phase-space density considerations (this Chapter; see also [46]). Our analysis excludes the shaded region to the left of the vertical line (2.44). Two dashed-dotted vertical lines mark the systematic uncertainties of this bound. The dotted line on the left marks the bound (2.41) based on the Pauli exclusion principle. The double-dotted dark orange line marks the bound (2.45). The black dashed-dotted line is the *non-resonant production production curve* (i.e. pairs of m_{NRP} and θ that lead to the correct dark matter abundance) [81]. The gray region marked "NRP production" accounts for possible uncertainties in the abundance computations within non-resonant production scenario (see [81, 86] for details).

We also performed the analysis for sterile neutrinos, produced in the presence of lepton asymmetry (resonant production mechanism) [78, 87, 88]. This mechanism is more efficient than the non-resonant production scenario and allows us to achieve the required dark matter abundance for weaker mixings (c.f. Fig. 4 in [88]). This lifts the upper bound on the dark matter particle mass in resonant production scenario to ~ 50 keV/c^2. To estimate the lower mass bound at this scenario, we have analyzed a number of available spectra (mass range $1 - 20$ keV/c^2, asymmetries $(2 - 700) \times 10^{-6}$ (see [87, 88] for the definition of asymmetry). The result are collected on the Fig. 2.3. One can see that based on $\bar{F}$, the $M_{RP} = 1$ keV/c^2 is allowed for
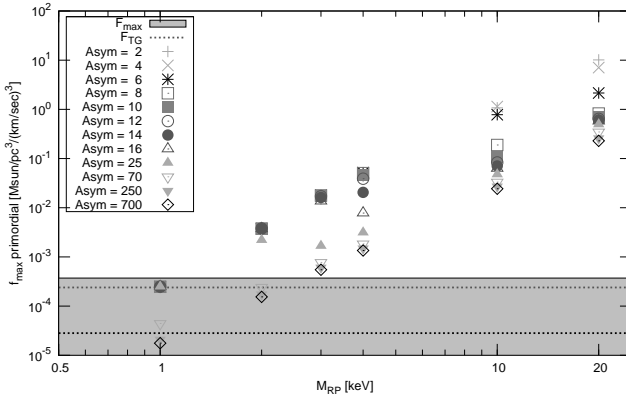
Figure 2.3: Restrictions on resonantly produced sterile neutrinos. Primordial f_{max} is computed numerically based on the spectra from [87, 88]. Different symbols parametrize different lepton asymmetries for a given mass (see definition of lepton asymmetry in [87, 88]). Grey shaded region is bounded by the maximal and minimal values of $\bar{F}$ for Leo IV (from Table 2.4, column 5). Horizontal dotted lines represent central value for $\bar{F}$ (lower) and F_{TG} (upper) for Leo IV. The dark matter spectrum is ruled out if the point falls into the shaded region (below the dotted line).

lepton asymmetries $L \gtrsim 10^{-4}$ and higher masses $M_{\mathrm{RP}} \geq 2 \, \mathrm{keV}/c^2$ are allowed for all available asymmetries. Based on the original Tremaine-Gunn bound, $M_{\mathrm{RP}} = 2 \, \mathrm{keV}/c^2$ is also allowed for sufficiently high ($L \gtrsim 10^{-4}$) lepton asymmetries. Thus, resonantly produced sterile neutrinos remain a viable dark matter candidate (see Fig. 2.4).

Finally, we would like to comment on the mechanism of production of sterile neutrinos from decay of massive scalar field, for example the inflaton [232] (for other models see [233–236]). The primordial phase-space distribution function for this case was computed e.g. in [232, 234, 236, 237]. Maximal value of phase-space density for this distribution is that of degenerate Fermi gas. Notice that the distribution functions in [232, 234, 236] $f(p)$ is formally unbounded for small momenta: $f(p) \sim p^{-1/2}$. From this one can easily find that the fraction of particles, having maximal phase-space density, is $\sim 10^{-8}$. As only this small fraction of all particles has maximal phase-space density, we expect the mass bound in this case to be stronger than (2.41).
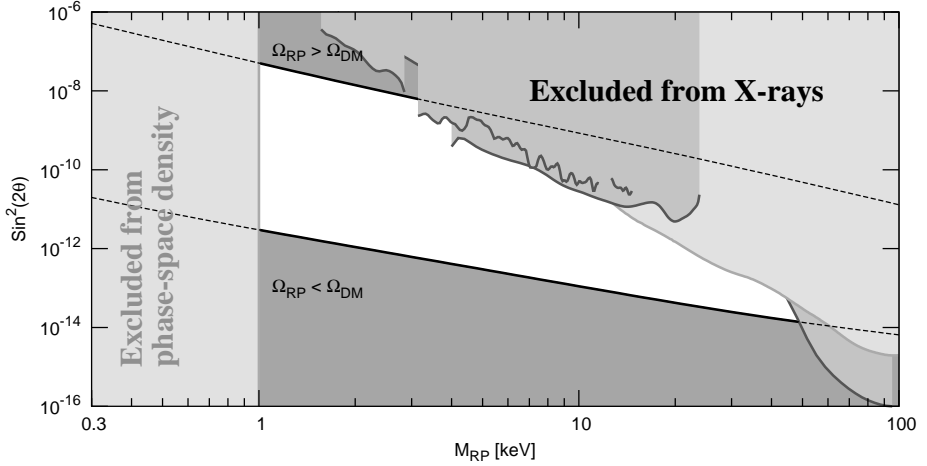
Figure 2.4: Allowed window of parameters for sterile neutrinos produced via resonant oscillations (white unshaded strip between two black lines). Two bounding black lines are obtained for non-resonant (upper line, lepton asymmetry $= 0$) and resonant production with the maximal lepton asymmetry, attainable in the νMSM [87, 88] (lower line). The grey regions in the upper right corner represent X-ray bounds [223, 228, 230, 231]. Region below $1\,\mathrm{keV}$ is ruled out from the phase-space density arguments (this work).

2.6.2 Influence of baryons

It should be noticed that our bounds (2.42)–(2.45) are valid under the assumption that the influence of the baryons does not result in the *increase* of the phase-space density in the course of structure formation. If this assumption does not hold, only the bound (2.41) remains intact. We discuss the robustness of this assumption below.

Although dark matter consists of the non-interacting particles, the remaining part of the galaxy – the baryons – interact with one another and dissipate their energy, finally concentrating towards the center. The baryons, which are condensed in the center, influence the shape of dark matter halo gravitationally, increasing the central dark matter density [238, 239]. The opposite effect is the energy feedback from SNae, galactic winds and reionization, which creates the strong outflow, significantly decreasing the mass of the gas and thereby affecting the dark matter halo shape. Such a

feedback is thought to be responsible to the formation of dwarf spheroidals from gas-rich dwarf spiral/irregular galaxies [240–244]. Clearly both gas condensation and feedback strongly influence the central phase-space density of dark matter [245], and in principle can lead to the violation of the inequality (2.3). Numerical studies of galaxy mergers show that baryons can lead to the increase of the phase-space density during the merger (see e.g. [246]). However, the method used in this work – coarse-graining of the phase-space density over a large phase-space region – reduces the influence of baryons. Indeed, we take the spatial averaging over the radius $R \sim r_h$, which includes external part of the system, where the amount of baryons is small. Additional studies are necessary to estimate effects of baryons and make our bounds more robust. We plan to address these issues elsewhere.

In the presence of lepton asymmetry, the resonant production of sterile neutrino dark matter takes place [78]. This mechanism is more efficient [78, 87, 88] than the non-resonant production scenario and allows to achieve required dark matter abundance for weaker mixings (c.f. Fig. 4 in [88]). This lifts the upper bound on the dark matter particle mass in this scenario up to $\sim 50\mathrm{keV}/c^2$. At the same time, for the same mass the primordial velocity distribution of resonant produced sterile neutrino dark matter is colder than in non-resonant production case. This f_{max} is as much as the order of magnitude bigger than (2.21) (c.f. [88]). This brings down by a factor ~ 2 the analog of the mass bound (2.44). Analyzing available spectra for a range of lepton asymmetries, we see that models with $m_{\mathrm{RP}} \gtrsim 1\,\mathrm{keV}/c^2$ are allowed. Thus, there is a large open "window" of allowed dark matter masses (c.f. Fig. 2.4). However, as the dependence of the velocity spectrum on the lepton assymetry is not monotonic, to obtain the exact shape of the lower bound on the mass at given mixing angle more work is needed. Nevertheless, our results show that the sterile neutrinos, produced in the presence of lepton asymmetry, are viable dark matter candidates, allowed by all current bounds.

Chapter 3

Decaying dark matter signal from different objects

In this Chapter we analyze dark matter distributions in several hundreds of dark matter-dominated objects in the local Universe (redshift $z < 0.3$) in order to estimate the dark matter decay map and determine optimal observational targets and detection strategy. We demonstrate that the expected dark matter decay signal (proportional to the "*dark matter column density*") increases slowly with the mass of the object. We determine a relation between the dark matter column density and the mass of the halo and demonstrate that the *scatter of this relation* can be predicted based on the existing numerical simulations of structure formation. Therefore, decaying dark matter would produce a unique all-sky signal, with a known slow-varying angular distribution — a signal that can be easily distinguished from any possible astrophysical background and therefore makes the astrophysical search for decaying dark matter an "almost direct" detection experiment.

3.1   Dark matter column density

The flux from the dark matter decay from a given direction (in $\mathrm{photons\ s^{-1}cm^{-2}}$) is given by

$$F_{\mathrm{DM}} = \frac{\Gamma E_\gamma}{m_{\mathrm{DM}}} \int_{\mathrm{fov\ cone}} \frac{\rho_{\mathrm{DM}}(\mathbf{r})}{4\pi|\mathbf{D}_L + \mathbf{r}|^2} \mathbf{dr}. \tag{3.1}$$

Here $\mathbf{D}_L$ is the *luminosity* distance between an observer and the centre of an observed object, $\rho_{\mathrm{DM}}(\mathbf{r})$ is the dark matter density, and the integration is

performed over the dark matter distribution inside the (truncated) cone – solid angle, spanned by the field of view (FoV) of the X-ray satellite. In case of distant objects[1], Eq. (3.1) can be simplified:

$$F_{\mathrm{DM}} = \frac{M_{\mathrm{DM}}^{\mathrm{fov}}\Gamma}{4\pi D_L^2}\frac{E_\gamma}{m_{\mathrm{DM}}}, \tag{3.2}$$

where $M_{\mathrm{DM}}^{\mathrm{fov}}$ is the mass of dark matter within a telescope field of view, m_{DM} – mass of the dark matter particle. In the case of small FoV, Eq. (3.2) simplifies to

$$F_{\mathrm{DM}} = \frac{\Gamma \mathcal{S}_{\mathrm{DM}}\Omega E_\gamma}{4\pi m_s}, \tag{3.3}$$

where

$$\mathcal{S}_{\mathrm{DM}} = \int_{l.o.s.} \rho_{\mathrm{DM}}(r)dr \tag{3.4}$$

is the *dark matter column density* (the integral goes along the line of sight), $\Omega \ll 1$ - FoV solid angle.

We start in Section 3.2 with the estimate of the decaying dark matter signal from the Milky Way halo. We demonstrate that unlike the case of annihilating dark matter, the decay signal is not concentrated in the Galactic Center (with its strong and uncertain astrophysical backgrounds), but varies slowly over the whole sky. In Sec. 3.3.2 we show that the dark matter column density weakly depends on properties of galaxies and galaxy clusters and changes no more than by an order of magnitude between the smallest galaxies and largest galaxy clusters. Finally, in Sec. 3.4 we discuss the obtained results.

3.2 Decay signal of the Milky Way halo

Because we reside in the inner part of Milky Way dark matter halo, it is the only object whose dark matter decay signal would be spread across the whole sky. The dark matter column density for the Milky Way halo is calculated using the expression [228]

$$\mathcal{S}_{\mathrm{DM}}^{MW}(\phi) = \int_0^\infty \rho_{\mathrm{DM}}\left(\sqrt{r_\odot^2 + z^2 - 2zr_\odot\cos\phi}\right) dz \tag{3.5}$$

---

[1]Namely, if luminosity distance D_L is much greater than the characteristic scale of the dark matter distribution.

where ϕ is the off-the-Galactic-center region, so that for the direction with galactic coordinates (l, b)

$$\cos\phi = \cos b \cos l. \tag{3.6}$$

and $r_\odot = 8\,\mathrm{kpc}$ is the distance from the Earth to the Sun.

It can be seen (e.g. [223, 228, 231]) that the function S_{DM}^{MW} can change only by a factor of few, when moving from the Galactic center ($\phi = 0°$) to the anti-center ($\phi = 180°$). That is, the Milky Way contribution to the decay is an all-sky signal. This is in stark contrast with the annihilating dark matter, where only few degrees around the Galactic Center represent a "region-of-interest".

3.3 Decaying dark matter signal from extragalactic objects

Let us now compare how contributions of other Galactic and extragalactic dark matter dominated objects compares with the column density of the Milky Way.

To properly compare the dark matter distributions in different objects, fitted by different density profiles, we *average* dark matter column density within a central part of an object. Namely, for each object we define a *characteristic radius* r_* (to be specified later, Sec. 3.3.2) and compute

$$\mathcal{S} = \frac{2}{r_*^2} \int_0^{r_*} r\,dr \int dz\, \rho_{\mathrm{DM}}(\sqrt{r^2 + z^2}) \tag{3.7}$$

Integral over z extends to the virial boundary of a dark matter halo (and can be extended all the way to infinity, as the integral converges). The definition (3.7) implies that $\mathcal{S}$ is proportional to the dark matter surface density within r_* ($\mathcal{S} \propto \rho_* r_*$), where ρ_* is the average dark matter central density.

It has been argued for some time that ρ_* and r_* *for galaxies* are inversely proportional (for review see e.g. [247], see [248, 249] for recent results). Similar result, *extended to cluster scales*, was originally discussed in [223]. If this were true, the dark matter column density and hence expected signal would be the same for different objects.

To investigate this result and to study the distribution of dark matter column density in the objects in local Universe, we compile a catalog of more than 1000 dark matter density profiles of about 300 unique objects

Type	No. objects	References	Objects
Galaxy clusters	130	[250–262]	[263]
Galaxy groups	26	[198, 264, 265]	[266]
Elliptical galaxies	10	[267–271]	[272]
Spiral galaxies	180	[195, 273–300]	[301]
Dwarf spheroidals	11	[10, 192, 193, 196, 300, 302]	[303]
total	357		

Table 3.1: **Observational data.** The table lists the types of objects; total number of collected objects; references used to collect the observational data; and the final list of selected objects.

(see Table 3.1 for details). The dataset contains dark matter-dominated objects of all types, from dwarf spheroidal satellites of the Milky Way to galaxy clusters. It spans more than 8 orders of magnitude in the halo masses and more than four orders of magnitude in r_* ($0.2\,\mathrm{kpc} \lesssim r_* \lesssim 2.5\,\mathrm{Mpc}$). For each of the objects we compute the dark matter column density, averaging over several profiles (if different measurements for the same object are available).

3.3.1 Types of dark matter density profiles

The distribution of dark matter in galaxies, galaxy groups and galaxy clusters can be described by several density profiles. In this work we concentrated on four popular choices for dark matter density profiles and establish how their parameters are related to the characteristic radius, r_*.

I. Numerical (N-body) simulations of the cold dark matter model have shown that the dark matter distribution in all relaxed halos can be fitted with the universal Navarro-Frenk-White (NFW) profile [304, 305]:

$$\rho_{\mathrm{NFW}}(r) = \frac{\rho_s r_s}{r(1 + r/r_s)^2} \tag{3.8}$$

parametrised by ρ_s and r_s. A more useful parametrization is in terms of the halo mass, M_{200}, and the concentration parameter, $c \equiv R_{200}/r_s$. Namely, R_{200} is the radius at which the average dark matter density is 200 times larger than the critical density of the universe ρ_{crit}. The halo mass M_{200} is the total mass of dark matter within this radius. The variables (ρ_s, r_s) and

(M_{200}, c) are thus connected as follows:

$$\rho_s = f(c)\rho_{\text{crit}}$$
$$r_s = \left(\frac{3M_{200}}{800\pi\rho_{\text{crit}}c^3}\right)^{1/3} \tag{3.9}$$
$$f(c) = \frac{200}{3}\frac{c^3}{\ln(c+1) - c/(c+1)}$$

The equations (3.9) allow to determine $\mathcal{S} \propto r_s\rho_s$ (see Eq. 3.4 as a definition of column density), knowing halo mass and concentration parameter M_{200}, c.

II. The Burkert (BURK) profile [306] has been shown to be successful in explaining the kinematics of disk systems (e.g. [286]):

$$\rho_{\text{BURK}}(r) = \frac{\rho_B r_B^3}{(r_B + r)(r_B^2 + r^2)}. \tag{3.10}$$

III. Another common parametrizations of cored profiles are given by the pseudo-isothermal (ISO) profile [287]

$$\rho_{\text{ISO}}(r) = \frac{\rho_c}{1 + r^2/r_c^2}. \tag{3.11}$$

IV. Modified pseudo-isothermal (IS2) profile [296]

$$\rho_{\text{IS2}}(r) = \frac{\rho_0}{\left(1 + r^2/r_0^2\right)^{3/2}}. \tag{3.12}$$

The quantity $\mathcal{S}(R)$ can be calculated analytically for all these choice of $\rho(r)$. For example, for the pseudo-isothermal profile one obtains:

$$\mathcal{S}_{\text{ISO}}(R) = \frac{2\pi\rho_c r_c^2}{R^2}\left[\sqrt{R^2 + r_c^2} - r_c\right]. \tag{3.13}$$

For the NFW density distribution (3.8):

$$\mathcal{S}_{\text{NFW}}(R) = \frac{4\rho_s r_s^3}{R^2}\left[\frac{\arctan\sqrt{R^2/r_s^2 - 1}}{\sqrt{R^2/r_s^2 - 1}} + \log\left(\frac{R}{2r_s}\right)\right]. \tag{3.14}$$

Notice, that this expression is real for both $R > r_s$ and $R < r_s$. The corresponding expression for the Burkert profile is rather lengthy and not very illuminating.
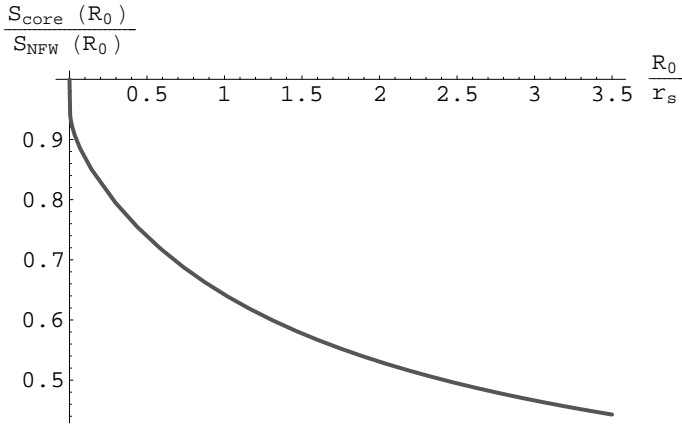
Figure 3.1: **The ratio of average column densities of the extreme cored and NFW profiles as a function of** R_0 (c.f. Eq. (3.15)).

3.3.2 Dependence of $\mathcal{S}$ on the inner slope of density profile.

In order to equally well fit the same rotation curve data, two dark matter profiles should have roughly the same mass within some radius R_0, determined by the observational data. If both profiles happen to have the same behaviour at large distances, their $\mathcal{S}$, averaged over R_0 will be essentially equal (as it is determined by the sum of the masses inside the sphere R_0 and in the outside of the cylinders, where the mass is dominated by the large r asymptotics).[2] In reality the situation is of course more complicated, one has to take into account the influence of baryons, the span of radii at which the data exists, etc.

We conservatively estimate the difference of column densities between a cusped and a cored profile as follows. We take the NFW density profile (3.8) as a representative of the cusped profile and its "extreme cored" counterpart $\rho_{core}(r)$ defined as follows:

$$\rho_{core}(r) = \begin{cases} \rho_{\text{NFW}}(r), & r > R_0 \\ \rho_{\text{NFW}}(R_0), & r \leq R_0 \end{cases} . \tag{3.15}$$

The column densities of these two profiles, averaged within R_0, differ only because the initial mass inside a *sphere* with radius R_0 for the cored pro-

---

[2]We will see below (Eq. (3.19)), that this is indeed the case for NFW and Burkert profiles.
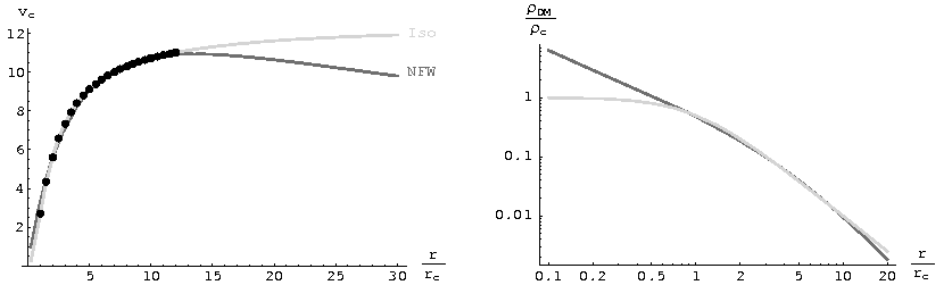
Figure 3.2: **Comparison of NFW and ISO profiles for the *simulated* rotation velocity points.** *Left panel:* the velocity data (black points, in units of $G_N \rho_c r_c^2$) is generated, assuming the ISO profile and fitted with the NFW profile. The parameters of the corresponding NFW profile (in the units of r_c, ρ_c) are given by eq. (3.16) in the text. *Right panel:* comparison of the density profiles with parameters, related by (3.16). The x-axis is in the units of isothermal core radius r_c.

file (3.15) diminishes as compared to the NFW case.

The resulting ratio of dark matter column densities is shown in the Supplementary Fig. 3.1 as a function of averaging radius R_0. In particular, for $R_0 = r_s$ this ratio is 64%, for $R_0 = 2r_s$ it equals to 53% and for $R_0 = 3r_s$ it drops to 47%. This implies that the difference of dark matter column densities between the cusped (NFW) and the extreme version of the cored profile (3.15) is within 50% for realistic averaging radii R_0 (usually $R_0 \sim 1-3r_s$). This difference is small compared to the intrinsic scatter expected on a object by object basis and well below the observational uncertainties on the parameters describing the density profile. This makes $\mathcal{S}$ a very robust quantity to compare observed properties of dark matter halos and results from numerical simulations and, consequently, test the prediction of the cold dark matter model.

The rotation curve of a galaxy is often fitted by several dark matter profiles (e.g. ISO and NFW). Let us analytically establish the relation between parameters of several profiles, *fitting the same rotation curve.* To this we take an ISO density profile and generate according to it the circular velocity profile $v_c^2(r)$, with r in the range $r_c \lesssim r \lesssim 15r_c$.[3] Then we fit these data using an NFW profile (see Fig. 3.2, left). We find the following relations between

---

[3]The final result is not sensitive to the exact choice of this range.

the parameters of the two profiles:

$$\text{NFW vs. ISO} \quad : \quad r_s \simeq 6.1 \, r_c \quad ; \quad \rho_s \simeq 0.11 \, \rho_c \, . \qquad (3.16)$$

The corresponding rotation curves and density profiles are shown in Supplementary Fig. 3.2.

Let us now compare the column densities for NFW and ISO profiles, whose parameters are related via Eq. (3.16). Results as a function of radius R are shown on Fig. 3.3. In particular, one sees that for $R = r_s$

$$\frac{\mathcal{S}_{\text{NFW}}(r_s)}{\mathcal{S}_{\text{ISO}}(6r_c)} \approx 0.91 \quad . \qquad (3.17)$$

One may be surprised that the cusped profile leads to the smaller column density than the cored one (as Eq. (3.17) demonstrate). This result however, can be simply understood. We match the velocity profiles for the NFW and ISO at some off-center distances $R_0 \sim 2r_s$, by demanding that the mass inside this sphere is the same for both profiles. The ISO profile is shallower in the outer regions than the NFW one. The ratio between the mass inside a sphere of the radius R_0 and a cylinder with base radius R_0 is equal to 0.58 at $R_0 = 6r_c$ for ISO profile, while it is 0.63 at $R_0 = r_s$ for the NFW profile . Thus the mass in the outer part of a cylinder is larger for the shallower ISO profile than for the cuspy NFW one, which explains the result (3.17).

It is clear from previous considerations that $\mathcal{S}_{\text{NFW}}$ and $\mathcal{S}_{\text{BURK}}$ (similarly matched) should be essentially identical, as both profiles have identical behaviour at $r \to \infty$. Indeed, in the case of the NFW and Burkert profiles the relation between their characteristic parameters is given by

$$\text{NFW vs. BURK} \quad : \quad r_s \simeq 1.6 r_B \quad ; \quad \rho_s \simeq 0.37 \rho_B \qquad (3.18)$$

which leads to

$$\frac{\mathcal{S}_{\text{NFW}}(r_s)}{\mathcal{S}_{\text{BURK}}(1.6r_s)} \approx 0.98 \quad . \qquad (3.19)$$

Finally, it should be noticed that we assume an infinite extension for Dark Matter halos, when computing the column density. However, the integrals in (3.7) are convergent at large off-center distances and therefore the details of the truncation of the dark matter distributions for $R > R_{200}$ do not affect the value of $\mathcal{S}$ by more than 10%.
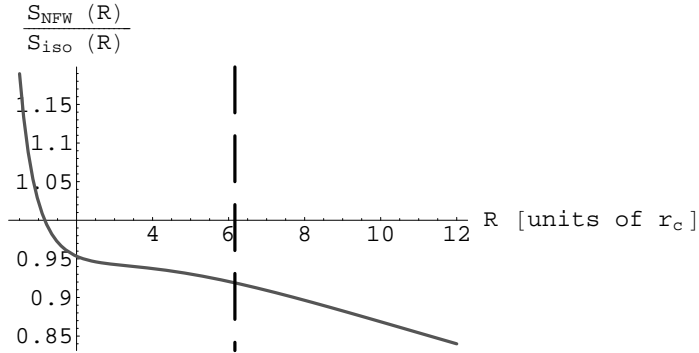
Figure 3.3: **Comparison of the column densities of NFW and ISO profiles.** Profiles describe the same data and their parameters are related via (3.16). The column density is averaged within various radii R. Dashed vertical line marks $R = r_s = 6.1 r_c$.

3.4 Universal properties of dark matter halos

The resulting dependence of dark matter column density on the type and mass of the objects is shown in Fig. 3.5.

By studying dark matter distribution in a large dataset of cosmic objects of different scale including dwarf, spiral and elliptical galaxies, galaxy groups and galaxy clusters we find the following relation between the characteristic dark matter column density $\mathcal{S}$ and the halo mass M_{halo}[4]:

$$\lg \mathcal{S} = 0.21 \lg \frac{M_{\mathrm{halo}}}{10^{10} M_\odot} + 1.79 \tag{3.20}$$

(with $\mathcal{S}$ in $M_\odot\,\mathrm{pc}^{-2}$).

To understand the relation (3.20) we compare our data with the results from cosmological N-body simulations within the ΛCDM [307, 308]. For each simulated halo we compute M_{halo}, fit the particle distribution to the NFW density profile and calculate $\mathcal{S}$ using formula (3.7). The observational data together with results from ΛCDM numerical simulations [307] is plotted of the Fig. 3.5. The black dashed-dotted line on this Figure is the $\mathcal{S} - M_{\mathrm{halo}}$

---

[4]We use M_{200} as halo mass M_{halo}. A proper definition of M_{200} can be found e.g. in [307] or in the Supplementary Information.
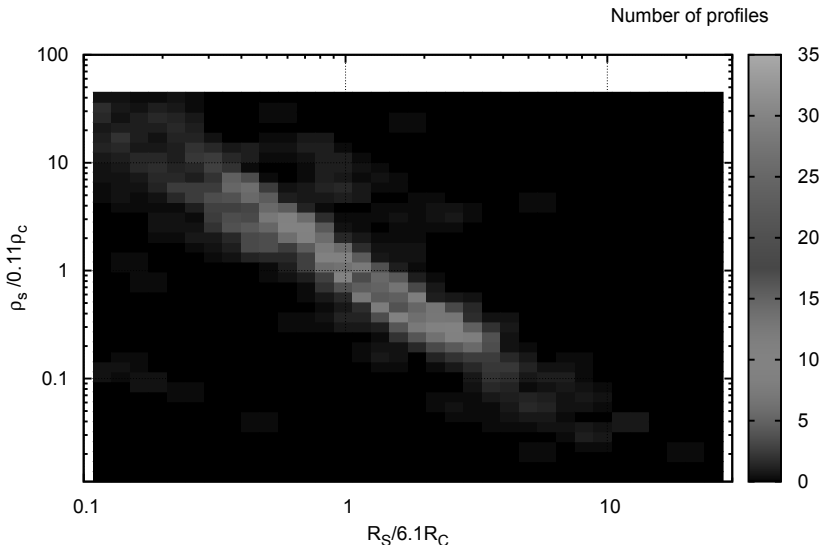
Figure 3.4: **Relation between parameters of NFW and ISO profiles in observed objects.** For objects for which both NFW and ISO fits of velocity rotation curves were available, we plot the ratios r_s/r_c and ρ_s/ρ_c. The maximum of the histogram lies in a region (3.16).

relation obtained from N-body simulations [307], using the fifth year cosmological parameters obtained from Wilkinson Microwave Anisotropy Probe (WMAP) satellite [309]. It fairly well reproduces the fit (3.20). Moreover, the pink shaded region (showing the 3σ scatter in the simulation data) contains most of the observational points within the halo mass range, probed by simulations. Therefore, the observed $M_{\text{halo}} - \mathcal{S}$ scaling coincides with the relation between the parameters of dark matter density profiles observed in numerical simulations for long time [305, 307, 310] over more than five orders of magnitude in mass.

Dwarf spheroidal satellites (dSphs) of the Milky Way (orange diamonds on the Fig. 3.5) do not follow the relation (3.20). Recently the Aquarius project has produced a statistically significant sample of well resolved density profiles for satellite halos [308], making it possible to determine their $r_* - \rho_*$

relation. Satellites were found to be more concentrated than isolated halos and thus have a higher value of $\mathcal{S}$ at fixed M_{halo}. Fig. 3.5 shows that the $\mathcal{S} - M_{\mathrm{halo}}$ relation for satellite halos (gray dashed line) from the Aquarius simulation [308] reproduces well the data on dSphs.

The fit to the data without the dSphs has the slope ≈ 0.23, much better quality of fit, and coincides extremely well with the results of N-body simulations [307] for isolated halos (black dashed-dotted line on Fig. 3.5). At masses below $10^{10} M_{\odot}$ no isolated halos were resolved in [307] and a simple toy model [307, 311] was used to predict the relation between parameters of NFW profile in a given cosmological scenario. The model (dotted line in the Fig. 3.5) fits well the results for the few spiral galaxies in this range. *Thus the agreement between observations and predictions from ΛCDM extend over more than eight orders of magnitude in mass.*

Comparison of our data with theoretical predictions (N-body simulations in our case) indicates that, despite the presence of various systematic errors in the data, the dark matter distributions in the observed objects exhibit a universal property – a systematic change of the average column density $\mathcal{S}$ as a function of the object mass ($\mathcal{S} \propto M_{\mathrm{halo}}^{0.2}$, relation (3.20)). This is different from the flat $\mathcal{S} = \mathrm{const}$ dependence, previously suggested [247–249]. The latter is based, in our view, on a confusion between the properties of isolated and non-isolated halos. Excellent agreement with pure dark matter simulations suggest also that the observed scaling dependence is insensitive to the presence of baryons, details of local environment, formation history.

The relation (3.20) can be used to search for deviations from cold dark matter model (e.g. warm dark matter models [105]) or modifications of gravity at large scales [312]. This motivates dedicated astronomical observations with all the data processed in a uniform way. Studies of the galaxies with the masses below $10^{10}\ M_{\odot}$ and galaxy clusters would be especially important.

Various scaling relations are known in astrophysics ("fundamental plane relation" for elliptical galaxies [313], "Tully-Fisher relation" for spiral galaxies [314], etc.). The relation (3.20) discussed in this Section differs in one crucial aspect: *it extends uniformly to all classes of objects at which dark matter is observed.* It would be very difficult to explain such a relation within Modified Newtonian dynamics [315] theory considered as an alternative to dark matter. That is why this relation, further confirmed, studied and understood analytically, may serve as one more evidence of the existence of dark matter.
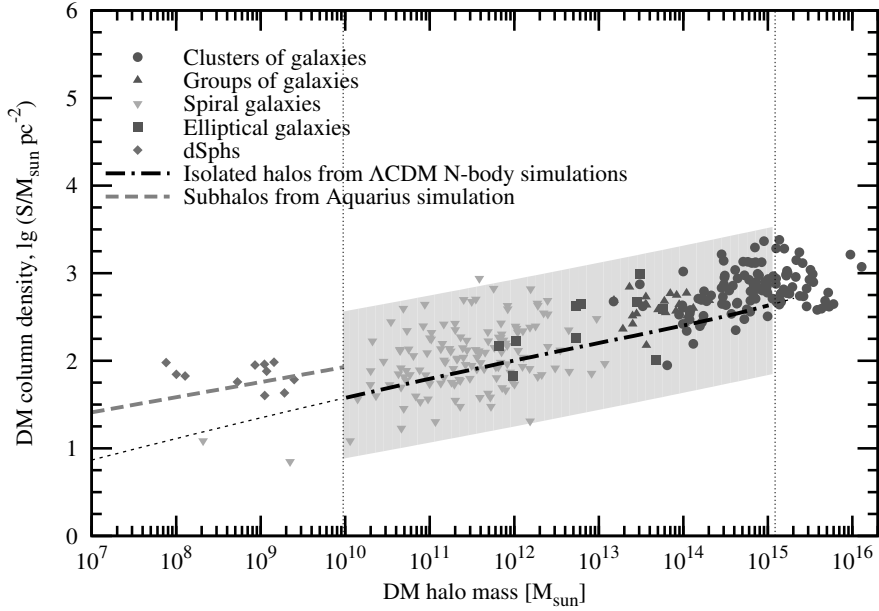
Figure 3.5: **Column density $\mathcal{S}$ as a function of halo mass $M_{\mathbf{halo}}$.** The black dashed-dotted line is the $S - M_{\mathrm{halo}}$ relation obtained from N-body simulations [307], using the WMAP fifth year cosmological parameters [309]. The shaded region shows the 3σ scatter in the simulation data. The vertical lines indicate the mass range probed by simulations. The dotted line is the theoretical prediction from the toy model for isolated halos [307, 311]. The gray dashed line shows the results from the Aquarius simulation for satellite halos [308].

Chapter 4

Detection strategy

The results of the previous Chapter demonstrate that the decaying dark matter would provide a unique all-sky signal, with a known slow-varying angular distribution, correlated with the matter distribution in the local Universe. Therefore *(a)* without sacrificing the expected signal one has a freedom of choosing observational targets, avoiding complicated astrophysical backgrounds; *(b)* if a candidate line is found, its surface brightness profile may be measured (as it does not decay quickly away from the centers of the objects) and distinguished from astrophysical lines that usually decay in outskirts of galaxies and clusters. Moreover, any tentative detection in one object would imply a signal of certain (comparable) signal-to-noise ratio from a number of other objects. This can be checked and the signal can either be unambiguously confirmed to be that of dark matter decay origin or ruled out. This allows to distinguish the decaying dark matter line from any possible astrophysical background and therefore makes astrophysical search for the decaying dark matter *another type of a direct detection experiment*.

In Sec. 4.1 we demonstrate the power of this approach. We check the claim of Ref. [316], that a spectral feature at 2.51 ± 0.07 keV in the spectrum of the Milky Way satellite known as Willman 1 [317]. By assuming that the reported signal comes from a dark matter decay line, we predict the parameters of corresponding decaying dark matter line in several local galaxies. After careful analysis of available X-ray observations of these objects, we find no significant line-like emission at ~ 2.5 keV range, which allows us to exclude the dark matter origin of this spectral feature at $\gtrsim 14\sigma$ level.

Then, we summarize all existing bounds on decaying dark matter lifetime

in the keV energy range in Sec. 4.2. These results are obtained from the analysis of medium exposure (about 100 kilo-seconds) X-ray observations of individual objects of different types. In Section 4.3 we discuss the best observational targets and possible ways to improve the existing bounds and probe the theoretically interesting regions of particle physics models.

We conclude that a combination of hundreds of archival observations of nearby galaxies, uniformly processed should in principle allow to increase the sensitivity for weak lines *and* study spatial dependence of each candidate line.

4.1 Verification of the dark matter origin of a spectral feature

A spectral feature at 2.51 ± 0.07 keV with the ux $(3.53\pm1.95)\times10^{-6}$ cts cm^{-2}s^{-1} (all errors at 68% confidence level) in the spectrum of Willman 1 was proposed in [316] as a candidate for a dark matter decay line. According to [316], the line with such parameters is marginally consistent the restrictions on decaying dark matter from some objects (see e.g. [318, 319] or the restrictions from the 7 ks observation of Ursa Minor dwarf spheroidal in [228]). The results of other works (e.g. [225, 227, 230]) are inconsistent at 3σ level with having 100% of decaying dark matter with the best-fit parameters of [316]. However, it is hard to exclude completely new unknown systematic uncertainties in the dark matter mass estimates and therefore in expected signal, from any given object. To this end, in this work we explicitly check for a presence of a line with parameters, specified above, by using archival observations by *XMM-Newton* of several objects, where comparable or stronger signal was expected. We compare the signals from several objects and show that the spatial (angular) behavior of the spectral feature is inconsistent with its dark matter origin so strongly, that systematic uncertainties cannot affect this conclusion. We also discuss a possible origin of the spectral feature of [316].

4.1.1 Choice of observational targets

Willman 1 signal. In [316] the signal was extracted from the central $5'$ of the Willman 1 observation. Assuming the dark matter origin of this sig-

nal, the observed flux $(3.53 \pm 1.95) \times 10^{-6}$ photons cm^{-2}s^{-1} corresponds to $F_{\mathrm{W1}} = (4.50 \pm 2.5) \times 10^{-8}$ photons cm^{-2}s^{-1}arcmin^{-2} flux per unit solid angle. The mass within the field-of-view (FoV) of the observation of Willman 1 was estimated in [316] to be $M_{\mathrm{W1}}^{\mathrm{fov}} = 2 \times 10^6 M_\odot$, using the best-fit values from [191]. Taking the luminous distance to the object to be $D_L = 38$ kpc, the average dark matter column density of Willman 1 is $\mathcal{S}_{\mathrm{W1}} \simeq 208.5\ M_\odot$ pc^{-2} (see however discussion in the Section 4.1.4 below). To check the presence of a dark matter decay line, we should look for targets with comparable signal.

The signal-to-noise ratio for a weak line observed against a featureless continuum is given by (see e.g. discussion in [229]):

$$(S/N) \propto \mathcal{S}\sqrt{t_{\mathrm{exp}}A_{\mathrm{eff}}\Omega_{\mathrm{fov}}\Delta E} \tag{4.1}$$

where $\mathcal{S}$ is the average dark matter column density within an instrument's field-of-view Ω_{fov}, t_{exp} is the exposure time, A_{eff} is an effective area of the detector and ΔE is the spectral resolution (notice that the line in question has a much smaller intrinsic width than the spectral resolution of *Chandra* and *XMM-Newton*). For the purpose of our estimate we consider the effective areas of *XMM-Newton* MOS cameras and *Chandra* ACIS-I (as well as their spectral resolutions) to be approximately equal, and effective area of PN camera is 2 times bigger, see Sec. 3.2.2 of [320] and [321].

Galactic contribution. The contribution of the Milky Way's dark matter halo along the line of sight should also be taken into account, when estimating the dark matter decay signal[1]. Using a pseudo-isothermal profile

$$\rho_{\mathrm{iso}}(r) = \frac{\rho_c}{1 + r^2/r_c^2}, \tag{4.2}$$

with parameters, adopted in [223, 228] ($r_c = 4$ kpc, $\rho_c = 33.5 \times 10^6 M_\odot/$ kpc^3, $r_\odot = 8$ kpc), the corresponding Milky Way column density in the direction of Willman 1 (120.7° off Galactic center) is $73.9 M_\odot$ pc^{-2}. As demonstrated in [231], the value of dark matter column density computed with this dark matter density profile coincides with the best-fit Navarro-Frenk-White [305, **NFW**] profiles of [194] and [195] within few % for the off-center angle $\phi \gtrsim 90°$. Other dark matter distributions produce systematically larger values of dark matter column density. For example, the best-fit pseudo-isothermal profile of [322] would corresponds to an additional Milky Way contribution

---

[1]Notice, that both in [316] and in this work only instrumental (particle) background has been subtracted from the observed diffuse spectra.
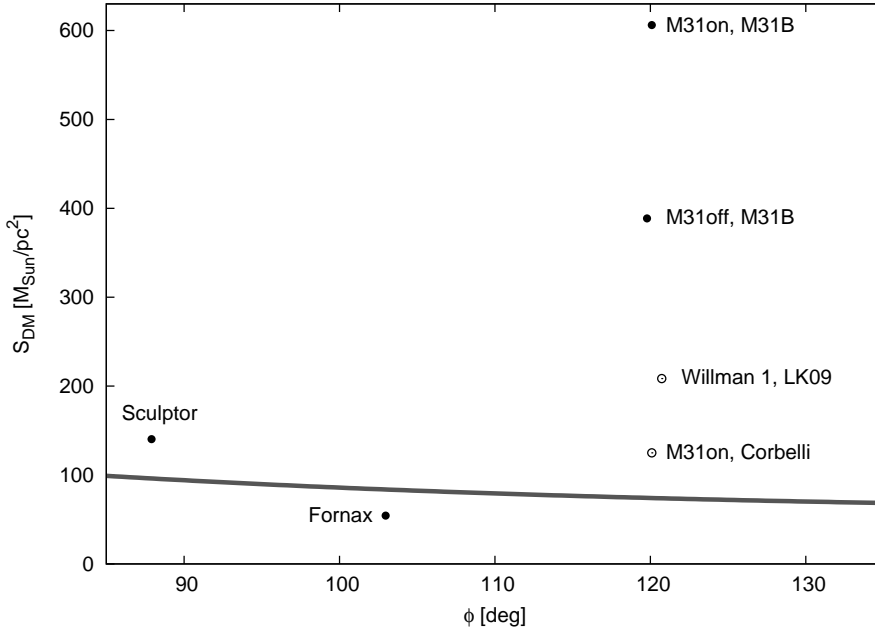
Figure 4.1: Comparison of dark matter column densities of the Milky Way (grey solid line) with the density profiles of M31, Fornax and Sculptor dSphs, discussed in the text. The dark matter column density estimate for Willman 1 is based on the "optimistic" dark matter density profile from [191], used in [316] (see [323] for discussion). The angle ϕ marks the direction off Galactic center (for an object with galactic coordinates (l, b) $\cos \phi = \cos l \cos b$).

$\sim 119 M_\odot \ \mathrm{pc}^{-2}$ in the direction of Willman 1. The comparison between the dark matter column densities of several objects with that of Milky Way in their directions is shown in Fig. 4.1.

4.1.2 *XMM-Newton* data analysis

For each *XMM-Newton* observation observation, we extracted both EPIC MOS and PN spectra.[2] According to standard recipies of *XMM-Newton* EPIC data analysis, we select only good events produced by photons from neighbouring pixels (for MOS cameras) and single pixel (for PN camera). We used the standard SAS task edetect_chain to exclude point sources, detected

---

[2]We use SAS version 9.0.0 and XSPEC 12.6.0.

with the likelihood values above 10 (about 4σ). For EPIC PN camera, bright strips with out-of-time events were also filtered out, following the standard procedure [324]. We imposed stringent flare screening criteria. To identify "good time intervals" we performed a light-curve cleaning, by analyzing temporal variability in the hard ($E > 10$ keV) X-ray band (as described e.g. in [325–327]). The resulting light curves were inspected "by eye" and additional screening of soft proton flares was performed by employing a method similar to that described in e.g. [328, 329] (i.e. by rejecting periods when the count rate deviated from a constant by more than 2σ). The extracted spectra were checked for the presence of residual soft proton contaminants by comparing count rates in and out of field-of-view [328, 330].[3] In all spectra that we extracted the ratio of count rates in and out of field-of-view did not exceed 1.13 which indicates thorough soft proton flare cleaning (c.f. [328]).

Following the procedure, described in [327] we extracted the filter-wheel closed background [332] from the same region as signal (in detector coordinates). The background was further renormalized based on the $E > 10$ keV band count rates of the extracted spectra. The resulting source and background spectra are grouped by at least 50 counts per bin using FTOOL [333] command grppha.

The extracted spectra with subtracted instrumental background were fitted by the powerlaw model of XSPEC in the energy range 2.1–8.0 keV data for MOS and 2.1–7.2 keV for the PN camera. This choice of the *baseline model* is justified by the fact that for all considered objects we expect no intrinsic X-ray emission above 2 keV and therefore the observed signal is dominated by the extragalactic diffuse X-ray background (XRB) with the power-law slope $\Gamma = 1.41 \pm 0.06$ and the normalization $(9.8 \pm 1.0) \times 10^{-7}$ photons cm^{-2} s^{-1} keV^{-1} arcmin^{-2} at 1 keV (90% confidence range errors) (see e.g. [326, 327, 330, 334–336]). Galactic contribution (both in absorption and emission) is negligible at these energies and we do not take it into account in what follows. For all considered observations powerlaw model provided a very good fit, fully consistent with the above measurements of XRB. The powerlaw index was fixed to be the same for all cameras (MOS1, MOS2, PN), observing the same spatial region, while the normalization was allowed to vary independently to account for the possible off-axis calibration uncertainties

---

[3]We use the public script [331] provided by the *XMM-Newton* EPIC Background working group and described in [330].

ObsID	PL index	PL norm, 10^{-4}ph. cm^{-2} s^{-1} keV^{-1}) at 1 keV (MOS1 / MOS2 / PN)	χ^2/dof
M31on observations:			
0109270101	1.33	5.71 / 5.80 / 7.88	1328/1363
0112570101	...	5.37 / 6.12 / 6.86	...
0112570401	...	6.13 / 6.66 / 6.37	...
M31off observation:			
0402560301	1.46	6.28 / 6.12 / 9.97	895/997
M31out observations:			
0511380101	1.53	2.75 / 2.88 / 3.89	875/857
0109270401	1.47	5.02 / 4.41 / 5.22	606/605
0505760401	1.27	1.91 / 2.04 / 2.47	548/528
0505760501	1.28	2.25 / 1.85 / 3.03	533/506
0402561301	1.57	2.94 / 3.10 / 3.95	489/515
0402561401	1.47	4.33 / 3.58 / 4.47	751/730
0402560801	1.55	5.22 / 4.49 / 5.83	902/868
0402561501	1.44	2.70 / 4.29 / 6.67	814/839
0109270301	1.39	4.29 / 4.58 / 3.75	413/436
Fornax observation:			
0302500101	1.52	4.46 / 4.02 / 3.78	938/981

Table 4.1: Best-fit values of `powerlaw` index and normalization for each *XMM-Newton* observation analyzed in this paper. The systematic uncertainty is included (see text). In `M31on` region, `powerlaw` index for different observations is chosen to be the same, because they point to the same spatial region.

between the different cameras, see e.g. [337, 338]. The best-fit values of the `powerlaw` index and normalizations are presented in Table 4.1.

To check for the presence of the [316] line in the spectra, we added a narrow ($\Delta E/E \sim 10^{-3}$) Gaussian line (XSPEC model `gaussian`) to the baseline `powerlaw` model. Assuming the dark matter origin of this line, we fix its normalization at the level F_{W1}, derived in [316], multiplied by the ratio of total (including Milky Way contribution) dark matter column densities and instrument's field-of-view. We vary the position of the line in the interval corresponding to the 3σ interval of [316]: 2.30 – 2.72 keV. Eq. (4.1) allows to estimate the expected significance of the line.

When searching for weak lines, one should also take into account uncertainties arising from the inaccuracies in the calibration of the detector response and gain. This can lead to systematic residuals caused by calibration inaccuracies, at the level $\sim 5\%$ of the model flux (some of them having edge-like or even line-like shapes) [see e.g. 339, 340] as well as discussion in [226] for similar uncertainties in *Chandra*. To account for these uncertainties we perform the above procedure with the 5% of the model flux added as a systematic error (using XSPEC command `systematic`).

4.1.3   Andromeda galaxy

4.1.3.1   Dark matter content of M31

The Andromeda galaxy is the closest spiral galaxy to the Milky Way. Its dark matter content has been extensively studied over the years [see e.g. 11, 12, 194, 197, 285, 298, 322, and references therein] for an incomplete list of recent works. The total dynamical mass (out to ~ 40 kpc) can be determined from the rotation curve measured from H I kinematics. The major uncertainty in determination of dark matter content is then related to a separation of contributions of baryonic (stellar bulge and especially, extended stellar disk) and dark components to the total mass.[4] The baryonic mass is often obtained from the (deprojected) surface brightness profile (optical or infrared), assuming certain mass-to-light ratio for the luminous matter in the bulge and the disk of a galaxy.

[230] analyzed dark matter distributions of M31, existing in the literature at that time in order to provide the most conservative estimate of the expected dark matter decay signal. The dark matter column density $\mathcal{S}$ in more than 10 models from the works [194, 197, 285, 298, 322] turns out to be consistent within a factor of ~ 2 for off-center distances greater than ~ 1 kpc (see gray lines in Fig. 4.2). The most conservative estimate of dark matter column density was provided by one of the models of [197] (called in that work M31B), marked as thick solid line on Fig. 4.2.

Recently two new H I surveys of the disk of M31 were performed [11, 12]

---

[4]Some works also take into account a presence of supermassive black hole in the center of a galaxy [see e.g 197] and additional contribution of a gaseous disk [c.f. 11, 12]. Their relative contributions to the mass at distances of interest turn out to be negligible and we do not discuss them in what follows.
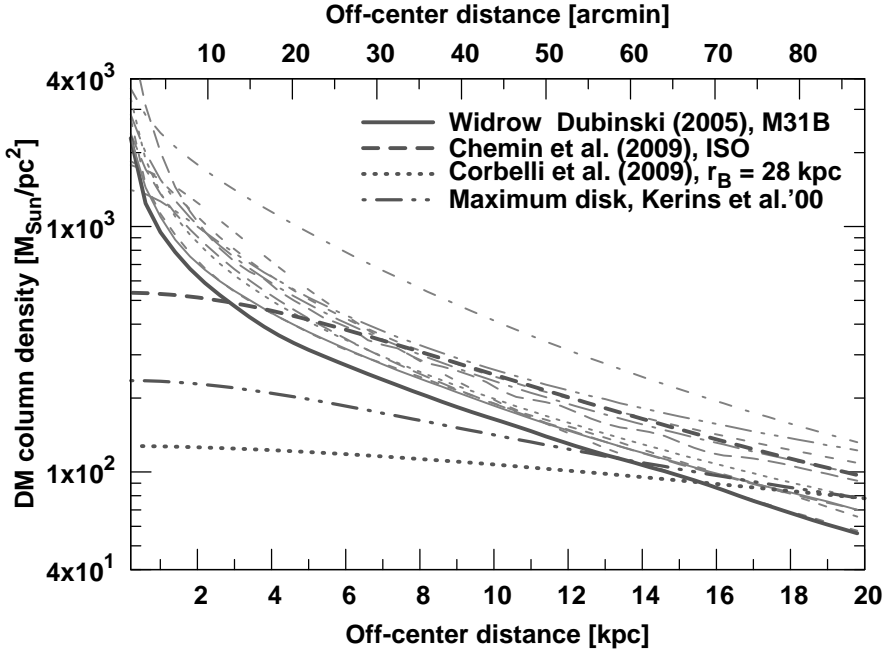
Figure 4.2: Dark matter column density of M31 as a function of off-center distance. The thin grey lines represent models from [194, 197, 285, 298, 322, 341] analyzed in [230]. The thick solid line represents the most conservative model M31B of [197]. The model of [12] (thick dashed line), the maximum disk model of [341] (thic dashed double-dotted line) and the "minimal" model ofk [11] (thick dotted line) (see text) are shown for comparison.

and new data on mass distribution of M31 became available.[5] In [12] modeling of H<small>I</small> rotation curve between ~ 0.3 kpc and 38 kpc was performed. [12] used *R-band* photometric information [343, 344] to determine the relative contribution of the stellar disk and the bulge. Based on this information and taking into account foreground and internal extinction/reddening effects [see section 8.2.2 in 12, for details] they determined mass-to-light ratio, using stellar population synthesis models [345] $\Upsilon_{disk} \simeq 1.7\Upsilon_\odot$ (in agreement with those of [197, 285]). Aiming to reproduce the data in the inner several kpc, they explored different disk-bulge decompositions with two values of the bulge's mass-to-light ratio $\Upsilon_{bulge} \simeq 0.8\Upsilon_\odot$ and $\Upsilon_{bulge} \simeq 2.2\Upsilon_\odot$ (all mass-

---

[5]We thank A. Kusenko and M. Loewenstein in drawing our attention to these works [342].

to-light ratios are in solar units). [12] analyzed several dark matter density profiles (NFW, Einasto, cored profile). According to their 6 best-fit models (3 dark matter density profiles times two choices of mass-to-light ratio) the dark matter column density in the Andromeda galaxy is higher than the one, adapted in [230] (model M31B) everywhere but inside the inner 1 kpc (see thick dashed line on Fig. 4.2).

[11] used circular velocity data, inferred from the HI rotation curves, also extending out to $\sim 37\,\mathrm{kpc}$. The authors exclude from the analysis the inner 8 kpc, noticing the presence of structures in the inner region (such as a bar), associated with non-circular motions. [11] also use optical data of [344] and determine an upper and lower bounds on the disk mass-to-light ratio using the same models [345, 346] as [12]. They obtain possible range of values of the *B-band* mass-to-light ratio $2.5\Upsilon_\odot \leq \Upsilon_\mathrm{disk} \leq 8\Upsilon_\odot$. These values do not take into account corrections for the internal extinction.[6] [11] fit the values of Υ_disk rather than fixing it to a theoretically preferred value. The mass-to-light ratio of the disk of a spiral galaxy is known to be poorly constrained in such a procedure since the contributions of the disk and dark matter halo are similar (see e.g. discussions in [12, 197]). [11] analyzed variety of dark matter models and mass-to-light ratios, providing good fit to the data. The mass model that maximizes the contribution of the stellar disk ($\Upsilon_\mathrm{disk} = 8$) has the core of the Burkert profile [306] $r_B = 28\,\mathrm{kpc}$ (if one imposes additional constraint on the total mass of M31 within several hundred kpc). The dark matter column density remains in this model remains essentially flat from the distance $\sim r_B$ inward (see Fig. 4.2). Notice, that the "maximum disk" fitting of [341] (blue dashed double-dotted line on Fig. 4.2) has higher dark matter content. Therefore in this work we will adopt the Burkert dark matter model of [11] as a *minimal* possible amount of dark matter, consistent with the rotation curve data on M31. The corresponding dark matter column density is factor 2–3 lower than the one given by the previously adapted model M31B in the inner 10 kpc. In what follows we will provide the restrictions for both M31B (as the *most conservative* among physically motivated models of dark matter distribution in M31) and Burkert model of [11].

---

[6]The correction for foreground extinction was taken into account in [11], using the results of [347]. The uniform disk extinction was not applied (which explains high values of Υ_disk). The authors of [11] had chosen not to include any uniform extinction corrections due to the presence of a gradient of B-R index (E. Corbelli, private communication).

ObsID	Cleaned exposure [ks] (MOS1 / MOS2 / PN)	FoV [arcmin^2] (MOS1 / MOS2 / PN)
0109270101	16.8 / 16.7 / 15.3	335.4/ 336.0 / 283.6
0112570101	39.8 / 40.0 / 36.0	332.9/ 333.1 / 285.9
0112570401	29.8 / 29.9 / 23.5	335.6/ 336.1 / 289.5

Table 4.2: Cleaned exposures and field-of-view after the removal of point sources and out-of-time events (calculated using BACKSCAL keyword) of three `M31on` observations.

4.1.3.2 M31 central part

Three observations of the central part of M31 (see Table 4.2 for details) were used in [230] to search for a dark matter decay signal. After the removal of bright point sources, the diffuse spectrum was extracted from a ring with inner and outer radii $5'$ and $13'$, centered on M31[7] (see [230] for details, where this region was referred to as `ring5-13`). We call these three observations collectively `M31on` in what follows. The baseline `powerlaw` model has the total $\chi^2 = 1328$ for 1363 d.o.f. (reduced $\chi^2 = 0.974$).

Below, we estimate the improvement of the signal-to-noise ratio (4.1), assuming the dark matter origin of [316] spectral feature. The average dark matter column density in the model M31B of [197]) is $\mathcal{S}_{\mathrm{M31on}} = 606\,M_\odot\,\mathrm{pc}^{-2}$. The dark matter column density from the Milky Way halo in this direction is $74.1\,M_\odot\,\mathrm{pc}^{-2}$.

The ratio of $t_{\mathrm{exp}} \times \Omega_{\mathrm{fov}} \times A_{\mathrm{eff}}$ of all observations of `M31on` (Table 4.2) and the [316] observation is 12.9. Thus one expects the following improvement of the S/N ratio:

$$\frac{(S/N)_{\mathrm{M31on}}}{(S/N)_{\mathrm{W1}}} = \frac{606 + 74.1}{208.5 + 73.9}\sqrt{12.90} \approx 8.65\;, \qquad (4.3)$$

i.e. the $\sim 2.5\sigma$ signal of [316] should become a prominent feature (formally about $\sim 21.6\sigma$ above the background) for the `M31on` observations. As described in Section 4.1.2 we add to the baseline powerlaw spectrum a narrow Gaussian line with the normalization fixed at $F_{\mathrm{M31on}} = \frac{606+74.1}{208.5+73.9}F_{\mathrm{W1}} \approx 1.08 \times 10^{-7}$ photons cm^{-2} s^{-1} arcmin^{-2}. The quality of fit becomes significantly worse (see Fig. 4.3). The increase of the total χ^2 due to the adding of

---

[7]We adopt the distance to M31 $D_L = 784$ kpc [348] (at this distance $1'$ corresponds to 0.23 kpc).

a line is equal to $(23.2)^2$, $(22.9)^2$ and $(22.2)^2$ for 1σ, 2σ and 3σ intervals with respect to the central respectively.

In addition to the `M31on` observations, we processed an *XMM-Newton* observation `0402560301`, positioned $\approx 22'$ off-center M31 (RA = 00h40m47.64s, DEC = +41d18m46.3s) – `M31off` observation, see Table 4.3. We collected the spectra from the central $13'$ circle. Several point sources were manually excluded from the source spectra. The rest of data reduction is described in the Section 4.1.3.2. The fit by the `powerlaw` model is excellent, the total χ^2 equals to 895 for 997 d.o.f. (the reduced $\chi^2 = 0.898$). Using the dark matter estimate based on the model M31B we find that the average dark matter column density for the `M31off` $\mathcal{S}_{\text{M31off}} = 388.6 M_\odot \, \text{pc}^{-2}$ plus the Milky Way halo contribution $74.3 M_\odot \, \text{pc}^{-2}$. The estimate of the line significance is similar to the previous Section and gives

$$\frac{(S/N)_{\text{M31off}}}{(S/N)_{\text{W1}}} = \frac{388.6 + 74.3}{208.5 + 73.9} \sqrt{8.76} \approx 4.85 \qquad (4.4)$$

and therefore, under the assumption of dark matter nature of the feature of [316], one would expect $\sim 12.1\sigma$ detection. After that, we add a narrow line with the normalization $F_{\text{M31off}} \approx 7.37 \times 10^{-8}$ photons $\text{cm}^{-2} \, \text{s}^{-1} \, \text{arcmin}^{-2}$ and perform the procedure, described in Section 4.1.2. The observation `M31off` rules out the dark matter decay line origin of the [316] feature with high significance (see Fig. 4.4): the increase of χ^2 due to the addition of this line has the minimum value $\Delta\chi^2 \simeq (10.4)^2$ at 2.44 keV, which is within 1σ interval of the quoted central value of the [316] feature.

We also perform the analysis, adding a line, whose flux is determined according to the dark matter density estimates based on the model of [11], that we consider to be a minimal dark matter model for M31 (as discussed in 4.1.3.1). For this model the column density in the central 1–3 kpc decreases by a factor ~ 3.4 as compared with the value, based on M31B. [342] claimed that in this case the [316] line becomes consistent with the `M31on` observations. However, our analysis shows that the total χ^2 *increases*, when adding the corresponding line to the model, by $(5.7)^2$ for 3σ variation of the position of the line. The corresponding increase of total χ^2 for `M31off` region is $(2.0)^2$. Combining `M31on` and `M31off` observations, one obtains $(6.2)^2$ increase of the total χ^2.

We conclude therefore that despite the uncertainties in dark matter modeling, the analysis of diffuse emission from the central part of M31 (1–8 kpc
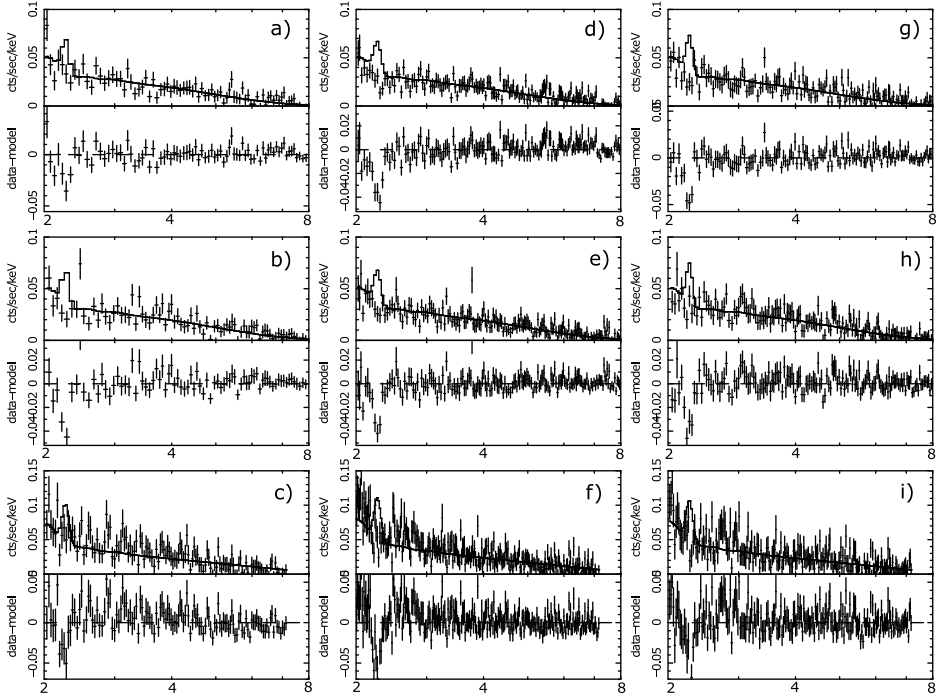
Figure 4.3: Spectra of three *XMM-Newton* observations of M31 (`M31on`, Sec. 4.1.3.2). The Gaussian line, obtained by proper scaling of the result of [316] is also shown. The top row is for MOS1, the middle row – for MOS2, and the bottom row for PN cameras. The spectra in the left column are for the observation `0109270101`, the middle column – `0112570101` and the right column – for `0112570401`. The error bars include 5% of the model flux as an additional systematic error. For all these spectra combined together, the χ^2 increases by *at least* 22.2^2, when adding a narrow Gaussian line in any position between $2.3\,\mathrm{keV}$ and $2.72\,\mathrm{keV}$ (see text).

off the center), as measured by *XMM-Newton*, disfavors the hypothesis that the spectral feature, observed in Willman 1, is due to decaying dark matter. Nevertheless, to strengthen this conclusion further we analyzed available *XMM-Newton* observations of M31 in the region 10–$20\,\mathrm{kpc}$ off-center, where the uncertainties in the mass modeling of M31 reduce significantly as compared with the central $5 - 8\,\mathrm{kpc}$ (c.f. [11, 12], see also Section 4.1.3.1, in particular Fig. 4.2).

ObsID	Cleaned exposure [ks] (MOS1 / MOS2 / PN)	FoV [arcmin^2] (MOS1 / MOS2 / PN)
0402560301	41.9 / 42.2 / 35.2	405.6/ 495.4 / 433.3

Table 4.3: Cleaned exposures and field-of-view (calculated using BACKSCAL keyword) of the observation `M31off` (obsID `0402560301`). The significant difference in FoVs between MOS1 and MOS2 cameras is due to the loss CCD6 in MOS1 camera.
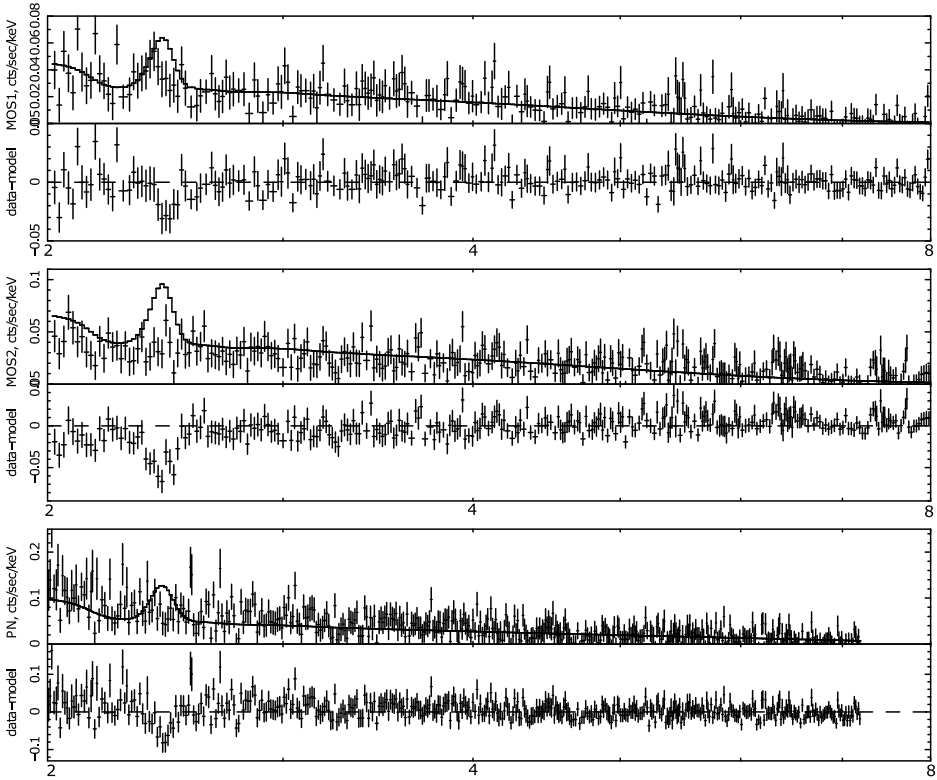

Figure 4.4: The spectra of off-center M31 observation `0402560301` (`M31off`, Sec.4.1.3.3). The decaying dark matter signal, obtained by proper scaling of the result of [316] is also shown. The error bars include 5% of the model flux as an additional systematic error. Fitting these spectra together excludes the properly scaled line of [316], at the level of at least 10.4σ (see text).

ObsID	Cleaned exposure [ks] (MOS1 / MOS2 / PN)	FoV [arcmin^2] (MOS1 / MOS2 / PN)
0511380101	44.3 / 44.5 / 37.6	356.2 / 400.4 / 333.3
0109270401	38.5 / 38.4 / 33.5	387.8 / 384.1 / 366.7
0505760401	26.0 / 26.0 / 21.7	330.5 / 374.1 / 325.0
0505760501	23.8 / 23.8 / 19.8	344.8 / 395.2 / 313.2
0402561301	22.7 / 22.7 / 20.1	367.2 / 419.5 / 382.6
0402561401	39.3 / 39.3 / 33.7	349.9 / 408.3 / 343.6
0402560801	42.6 / 42.6 / 36.6	373.6 / 435.8 / 393.7
0402561501	38.5 / 38.5 / 34.0	369.3 / 421.0 / 407.5
0109270301	24.4 / 24.6 / 22.2	443.4 / 439.6 / 405.0

Table 4.4: Cleaned exposures and field-of-view after the removal of point sources and out-of-time events (calculated using BACKSCAL keyword) of nine M31 observations off-set by more than 10 kpc from the center (`M31out` observations).

4.1.3.3 M31 off-center (10-20 kpc)

We selected 9 observations with MOS cleaned exposure greater than 20 ks (Table 4.4). The total exposure of these observations is about 300 ks. Based on the statistics of these observations one would expect a detection of the signal of [316] with the significance 12.1σ (for M31B) and 11.2σ (for [11]). The fit to the baseline model is very good, giving total χ^2 equal to 5931 for 5883 d.o.f. (the reduced $\chi^2 = 1.008$). However, adding the properly rescaled line significantly reduced the fit quality, increasing the total χ^2 by $(12.0)^2/(10.7)^2/(10.7)^2$ when varying line position within 1σ, 2σ and 3σ intervals (using M31B model) and by $(11.7)^2$, $(10.7)^2$ and $(10.6)^2$ for 1σ, 2σ and 3σ intervals (using the model of [11], which gives dark matter column density in `M31out` about $160 - 180 M_\odot \, \mathrm{pc}^{-2}$ (including Milky Way contribution), see Fig. 4.2).

4.1.3.4 Combined exclusion from M31

Finally, performing a combined fit to all 13 observations of M31 (`M31`, `M31off`, `M31out`) we obtain the exclusion of more than 26σ (using the dark matter model M31B of [197]) and more than 13σ for the minimal dark matter model of [11]. As described in Section 4.1.2, in deriving these results we allowed the normalization of the baseline `powerlaw` model to vary independently

for each camera, observing the same spatial region, added additional 5% of the model flux as a systematic uncertainty and allowed the position of the narrow line to vary within $2.3 - 2.72\,\mathrm{keV}$ interval.

4.1.4 Fornax dwarf spheroidal galaxy and Willman 1

We use dark matter distributions in Fornax dwarf spheroidal galaxy and Willman 1 presented in [323]. In this paper, it is shown that the mass distribution in Willman 1, as well as its galactic status (dwarf spheroidal galaxy vs metal-poor globular cluster) remain uncertain, mostly due to extreme smallness of available kinematic data. For example, [316] have used the dark matter distribution from [191] who used velocities of only 47 stars. In [323], the authors used even smaller published sample of 14 stars which does not allow to significantly constrain the dark matter distribution. For example, dark matter distribution in Fornax and Sculptor dwarf spheroidal galaxies, the brightest and most well-studied dSph satellites of the Milky Way, the availability of large kinematic data set of ~ 2600 and ~ 1400 members, respectively [349], allows to place relatively tight constraints on the dark-matter column densities with the help of Monte Carlo Markov chain analysis procedure of [196]. To characterize the dark matter halos of dSphs, [323] adopt the general dark matter halo model of [196], with density profile given by

$$\rho(r) = \rho_s \left(\frac{r}{r_s} \right)^{-\gamma} \left[1 + \left(\frac{r}{r_s} \right)^{\alpha} \right]^{\frac{\gamma-3}{\alpha}}, \tag{4.5}$$

where the parameter α controls the sharpness of the transition from inner slope $\lim_{r\to 0} d\ln(\rho)/d\ln(r) \propto -\gamma$ to outer slope $\lim_{r\to\infty} d\ln(\rho)/d\ln(r) \propto -3$. This model includes as special cases both *cored* ($\alpha = 1, \gamma = 0$) and NFW [305] ($\alpha = \gamma = 1$) profiles. The results are shown in Fig. 4.5 and have been used for the subsequent analysis.

4.1.4.1 *XMM-Newton* observation of Fornax dSph

Fornax is one of the most deeply observed dSphs in X-ray wavelengths. We have processed the 100 ks *XMM-Newton* observation (ObsID `0302500101`) of the central part of Fornax dSph. The data analysis is described in the Section 4.1.2. In each camera, we extract signal from the $14'$ circle, centered on the Fornax dSph. The cleaned exposure and corresponding fields of view
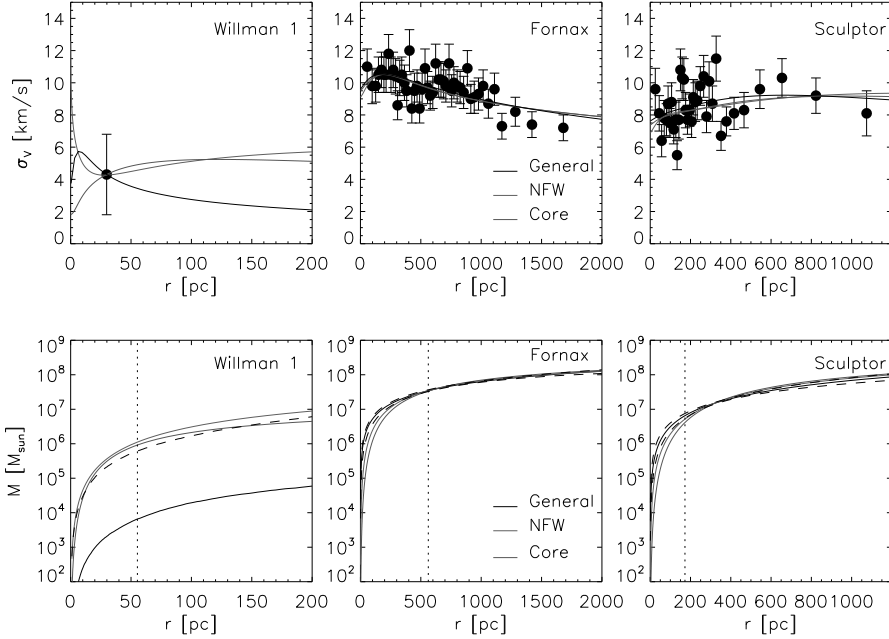
Figure 4.5: Dark matter mass modeling in Fornax and Willman 1 from [323]. Top panels display empirical velocity dispersion profiles as calculated by [196] for Fornax, Sculptor and from the Willman 1 data of [350] (for Willman 1, the small published sample of 14 stars allows for only a single bin). Overplotted are the median profiles obtained from the Monte-Carlo Markov chain analysis described by [196], using the general dark matter halo model (4.5), as well as the best-fitting NFW and cored halo models. Bottom panels indicate the corresponding spherically-enclosed mass profiles. In the bottom panels, dashed lines enclose the central 68% of accepted general models (for Willman 1, the lower bound falls outside the plotting window). Vertical dotted lines indicate the outer radius of the field of view of the X-ray observations ($14'$ for Fornax, $7.5'$ for Sculptor and $5'$ for Willman 1).

Chapter 4. Detection strategy

XMM-Newton ObsID	Cleaned exposure [ks] (MOS1 / MOS2 / PN)	FoV [arcmin^2] (MOS1 / MOS2 / PN)
0302500101	53.8 / 53.9 / 48.2	459.1 / 548.5 / 424.9

Table 4.5: Cleaned exposures of the *XMM-Newton* observation of Fornax dSph

(calculated using the BACKSCAL keyword) for all three cameras (after sub-traction of CCD gaps, out-of-time strings in PN camera and CCD 6 in MOS1 camera) are shown in Table 4.5. Based on the dark matter estimates, presented in [323] we expect the following improvement in S/N ratio

$$\frac{(S/N)_{\text{Forn}}}{(S/N)_{\text{W1}}} = \frac{54.4 + 83.2}{208.5 + 73.9}\sqrt{12.12} \approx 1.70 \qquad (4.6)$$

i.e. we expect a $\sim 4.2\sigma$ signal from Fornax, assuming dark matter decay line origin of the [316] feature.

The fit to the baseline model is very good, $\chi^2 = 955$ for 983 d.o.f. (reduced $\chi^2 = 0.972$). Note that the parameters are consistent with those of extragalactic diffuse X-ray background as it should be for the dwarf spheroidal galaxy where we do not expect any diffuse emission at energies above $2\,\text{keV}$ [see also 223, 228, 318, 319, 351].

After adding a narrow line with the normalization $F_{\text{Forn}} \approx 2.19 \times 10^{-8}$ photons cm^{-2} s^{-1} arcmin^{-2}, the χ^2 *increases*, the minimal increase is equal to $(5.1)^2$, $(4.2)^2$ and $(3.3\sigma)^2$ for a position of the line within 1σ, 2σ and 3σ intervals from [316] feature, respectively (after adding 5% of model flux as a systematic error). We see that adding a properly scaled Gaussian line worsens χ^2 by at least $\sim 3.3\sigma$ (instead of expected *improvement* of the quality of fit by a factor of about 16 if the [316] feature were the dark matter decay line), see Fig. 4.6 for details.

The combination of all *XMM-Newton* observations used in this work (M31on, M31off, M31out and Fornax) provide a minimum of 26.7σ exclusion at 2.35 keV (which falls into the 3σ energy range for the [316] spectral features), after adding a 5% systematic error. Within 1σ and 2σ energy intervals, the minimal increase of χ^2 is 29.0^2 and 27.3^2, correspondingly. Therefore, one can exclude the dark matter origin of the [316] spectral feature by 26σ. This exclusion is produced by using the most conservative dark matter model M31B of [197]. Using the minimal dark matter model of [11], one can exclude the [316] feature at the level more than 14σ.
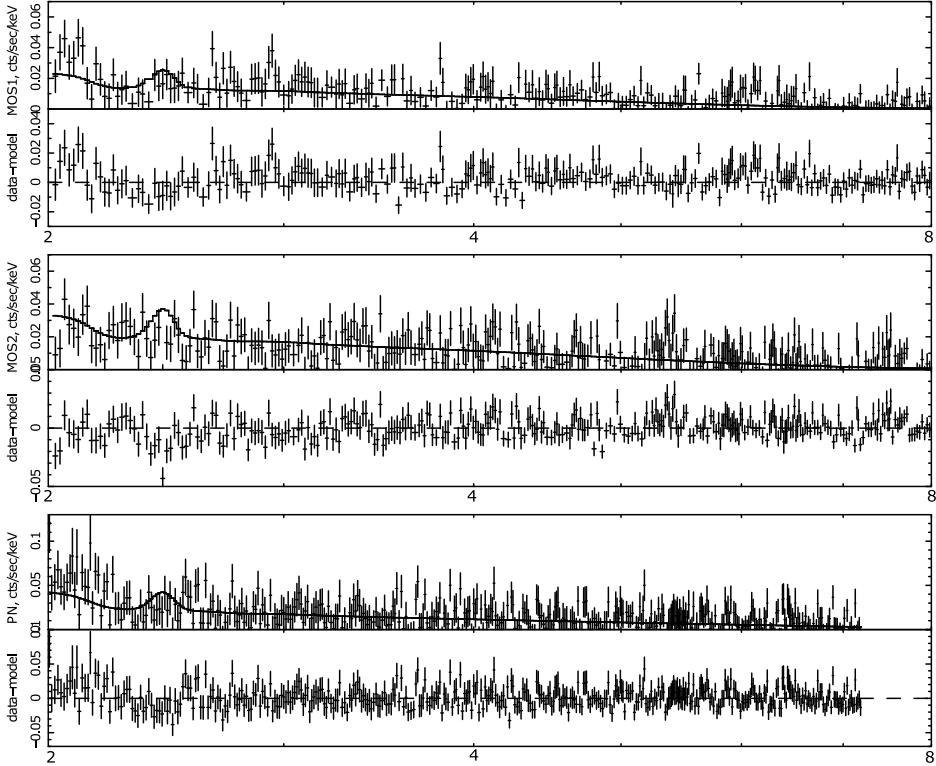
Figure 4.6: The spectra of the *XMM-Newton* observation `0302500101`, Sec. 4.1.4.1. The error bars include 5% of the model flux as an additional systematic error. Fitting these spectra together excludes the properly scaled [316] line at the level of at least 2σ (3.3σ if one restricts the position of the line to the interval $2.30 - 2.72$ keV) instead of expected improving of the quality of fit by about 4σ (if the line were of the dark matter origin).

Regions	PL index, best-fit	PL norm. best-fit	Line position	Line signif.	Line flux best-fit value	Line flux 3σ *upper* bound
M31on	1.32	1.66/1.82/2.39	2.55	1.7σ	7.35×10^{-9}	2.09×10^{-8}
M31off	1.42	1.51/1.19/2.22	2.47	2.3σ	6.69×10^{-9}	3.10×10^{-8}
M31out	...	.../.../...	2.52	1.6σ	3.76×10^{-9}	1.16×10^{-8}
Fornax	1.37	0.79/0.59/0.70	2.19	2.6σ	9.63×10^{-9}	2.11×10^{-8}

Table 4.6: Parameters of the best-fit `powerlaw` components (assuming the `powerlaw+gauss` model) and of the maximally allowed flux in the narrow Gaussian line in the interval $2.1 - 2.8$ keV. The normalization of the `powerlaw` is given in 10^{-6} photons cm^{-2} s^{-1} arcmin^{-2} keV^{-1}, line position – in keV, fluxes of `gaussian` – in photons cm^{-2} s^{-1} arcmin^{-2} keV^{-1}. The slight difference between these values and those of Table 4.1 is due to the presence of `gaussian` component and the proportionality of `powerlaw` normalization to field-of-view solid angle (for M31on); for each observation, the corresponding parameters coincide within 90% confidence range. The values of best-fit `powerlaw` parameters for M31out are not shown because they are different for different observations (see Table 4.1).

4.1.5 On a possible origin of a 2.5 keV feature

We provide more than 80 times improvement of statistics of observations, as compared to [316] (factor ~ 5 times larger total exposure time and factor ~ 4 improvement in both the effective area and the field-of-view). Even under the most conservative assumption about the dark matter column density such an improvement should have led to an about 14σ detection of the dark matter decay line. In our analysis no significant lines in the position, predicted by [316] were found. However, in the *XMM-Newton* observations that we processed there are several spectral features in the range $2 - 3$ keV (see Table 4.6). This is not surprising, as the *XMM-Newton* gold-coated mirrors have Au absorption edge at ~ 2.21 keV [339, 340] and therefore their effective areas possess several prominent features in the energy range $2 - 3$ keV. According to *XMM-Newton* calibration report [339, 340], there is about 5% uncertainty at the modeling of the effective area of both MOS and PN cameras at these energies. These uncertainties in the effective area can lead to artificial spectral features due to the interaction of the satellite with cosmic rays [352]. In particular, the solar protons with energies of few hundreds keV can be interpreted as X-ray photons (so called *soft proton flares*). The interaction efficiency of solar protons with the instrument is known to be totally different from that of real photons [329]. In particular, their flux is not af-

fected by the Au edge of the *XMM-Newton* mirrors. According to [329], the spectrum of soft proton flares for EPIC cameras is well described by the *unfolded* (i.e. assuming that the instrument's response is energy-independent) broken powerlaw model with the break energy around ~ 3.2 keV, `bknpow/b` in `XSPEC v.11`. Therefore, modeling the spectrum that is significantly contaminated with soft proton flares in a standard way (i.e. by using *folded* `powerlaw` model) will produce artificial residual excess at energies of sharp decreases of the instrument's effective area.

In our data analysis we performed both the standard flare screening [325–327] that uses the inspection of high-energy (10–15 keV) light curve and an additional soft proton flare cleaning. As found by [353], it is possible to screen out the remaining flares, e.g. by the visual inspection of the cleaned lightcurve at low and intermediate energies. To provide the additional cleaning after the rejection of proton flares at high energies, we followed the procedure of [329, 330], leaving only the time intervals, where the total count rate differs from its mean value by less than 2σ.

To test the possible instrumental origin of the features, discussed in this Section, we first performed only a high-energy light curve cleaning [325–327] and determined the maximally allowed flux in a narrow line in the energy interval of interest. After that we performed an additional soft proton cleaning. This procedure improved the quality of fit. The significance contours of the resulting "line" (for `M31out` region) are shown on the left panel in Fig. 4.7. In deriving these limits we allowed both the parameters of the background, the position of the line and its total normalization to vary (the latter from negative values). Finally, we added an unfolded broken powerlaw component `bknpow/b` to model a contribution of remaining soft proton flares (see e.g. [329]). The break energy was fixed as 3.2 keV so no degeneracy with the parameters of the `gaussian` is expected. The `bknpow/b` powerlaw indices at low and high energies were fixed to be the same for different cameras observing the same spatial region. further improved the quality of fit and made the line detection totally insignificant (see right Fig. 4.7 for details). Our analysis clearly suggests the instrumental origin of the line-like features at the energy range 2.1–2.8 keV.

As a final note, we should emphasize that the *Chandra* ACIS instrument used in [316] has the Ir absorption edges near 2.11 and 2.55 keV (see [354] for additional discussion). They also report negative result of searching for
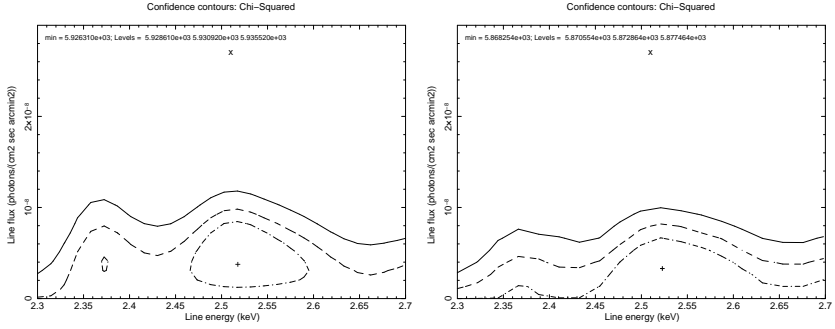
Figure 4.7: *Left:* $\Delta\chi^2 = 2.3$ (dashed-dotted), 4.61 (dashed) and 9.21 (solid) contours (corresponding to 68%, 90% and 99% confidence intervals) for a thin `gaussian` line allowed by the joint fit of `M31out` spectra used in this work. The resulting line normalizations are shown for an averaged dark matter column density in the `M31out` region (about $170 M_\odot \,\mathrm{pc}^{-2}$, including the Milky Way contribution). The rescaled [316] line is marked with a cross x; its normalization is therefore $4.50 \times 10^{-8} \times \frac{170}{208.5+73.9} = 2.71 \times 10^{-8} \mathrm{photons\ cm}^{-2}\ \mathrm{sec\ arcmin}^{-2}$. It is clearly seen that the hypothesis of dark matter origin for a [316] line-like feature is excluded at extremely high significance, corresponding to more than $\approx 10\sigma$ (see text). *Right:* The same as in the left figure but with an addition of a `bknpow/b` component to model the contribution of the remaining soft proton contamination (see text). The break energy is fixed as 3.2 keV so no degeneracy with the parameters of the `gaussian` is expected. The `bknpow/b` powerlaw indices at low and high energies are fixed to be the same for different cameras observing the same spatial region. The line significance drops below 1σ in this case.

the [316] feature, in agreement with our findings.

4.1.6 Conclusion

To summarize, by comparing the strength and position of the feature found by Loewenstein & Kusenko with observations of several dark matter-dominated objects (M31, Fornax and Sculptor[8] dSphs) we found that the hypothesis of dark matter origin of [316] is excluded with the combined significance exceeding 14σ even under the most conservative assumptions. This is possible because of the large increase of the statistics in our observations as compared with the observation used in [316].

[8]Non-detection of $\sim$2.5 keV line in *Chandra* observations of Sculptor dwarf spheroidal galaxy by [323] further strengthens our result.

4.2 Summary of existing X-ray bounds on decaying dark matter parameters

Table 4.7 summarizes existing works that put bounds on decaying dark matter from observations of individual objects. In this Table, we do not discuss the claim [355] that the intensity of the Fe XXVI Lyman-γ line at 8.7 keV, observed in [356] cannot be explained by standard ionization and recombination processes, and that the dark matter decay may be a possible explanation of this apparent excess. Spectral resolution of current missions does not allow to reach any conclusion. However, barring an *exact* coincidence between energy of decay photon and Fe XXVI Lyman-γ, this claim may be tested with the new missions, discussed in Chapter 6.

4.3 Strategy of further searches for decaying dark matter

Our results (Chapter 3, in particular Section 3.4) allow us to identify the best observational targets and the strategy of searches for decaying dark matter.

The objects with the largest dark matter decay signal turn out to be the nearby galaxy clusters. However, the detection of the dark matter decay line from galaxy clusters in X-rays is complicated by the fact that most of them show strong emission precisely in keV range.[9] Indeed, the virial theorem immediately tells us that the temperature of the intercluster medium is

$$T_{\text{gas}} \sim G_N \, m_p \, \mathcal{R} \rho_* r_*^2, \tag{4.7}$$

where ρ_*, r_* are characteristic density and size (see Section 3.1), $\mathcal{R}$ is a typical overdensity in objects of a given type, m_p is the proton mass. For galaxy clusters the overdensity $\mathcal{R} \sim 10^3$ and size $r_* \sim 1$ Mpc, the temperature T_{gas} is always in the keV range, which makes it hard to detect a dark matter decay line against a strong X-ray continuum.

The optimal targets for detection the dark matter line become X-ray faint objects, such as dwarf spheroidal galaxies which do not contain any X-ray

---

[9]When searching for decaying dark matter signatures in other energy ranges, e.g. in the GeV range, galaxy clusters become the best targets, see e.g. [364].

Reference	Object	Instrument	Cleaned exp, ks
[221]	Diffuse X-ray background	HEAO-1, *XMM-Newton*	224, 1450
[222]	Coma & Virgo galaxy clusters	*XMM-Newton*	20, 40
[223]	Large Magellanic Cloud	*XMM-Newton*	20
[224]	Milky Way halo	*Chandra*/ACIS-S3	Not specified
[225][a]	M31 (central 5′)	*XMM-Newton*	35
[357]	Abell 520 galaxy cluster	*Chandra*/ACIS-S3	67
[228]	Milky Way halo, Ursa Minor dSph	*XMM-Newton*	547, 7
[358]	Milky Way halo	*Chandra*/ACIS	1500
[226]	Galaxy cluster 1E 0657-56 ("Bullet")	*Chandra*/ACIS-I	450
[229]	Milky Way halo	X-ray microcalorimeter	0.1
[359][b]	Milky Way halo	INTEGRAL/SPI	5500
[230]	M31 (central $5 - 13'$)	*XMM-Newton*/EPIC	130
[231][b]	Milky Way halo	INTEGRAL/SPI	12200
[318]	Ursa Minor	*Suzaku*/XIS	70
[319]	Draco dSph	*Chandra*/ACIS-S	32
[316][c]	Willman 1	*Chandra*/ACIS-I	100
[323][d]	M31, Fornax, Sculptor	*XMM-Newton*/EPIC , *Chandra*/ACIS	400, 50, 162
[354][e]	Willman 1	*Chandra*/ACIS-I	100
[360]	Segue 1	Swift/XRT	5
[361]	M33	*XMM-Newton*/EPIC	20-30
[362]	M31 ($12 - 28'$ off-center)	*Chandra*/ACIS-I	53
[363]	Willman 1	*XMM-Newton*	60
[71]	Ursa Minor, Draco	*Suzaku*/XIS	200, 200

Table 4.7: Summary of existing X-ray observations of different objects performed by different groups.

[a] Mistakes on calculating the bound, see discussion in [230].

[b] INTEGRAL/SPI is sensitive at 20 keV–7 MeV.

[c] Claimed presence of 2.5 keV feature.

[d] Did not put any bounds, only checked of the origin of 2.5 keV feature.

[e] Re-analyzed the same observation of Willman 1, did not find 2.5 keV feature.

gas [223]. However archival observations of dwarf spheroidal galaxies have rather short exposure.

Objects with comparable column density and X-ray quiet (at least in energies above 1–2 keV) are the *nearby spiral galaxies*. Of these objects the Milky Way (including LMC and SMC satellites) and Andromeda galaxy had been observed for the longest (combined) time. In Fig. 2.2 it is shown that the strongest bounds on parameters of decaying dark matter particles come from either Milky Way halo [228] or the central part of the Andromeda galaxy [230].

The strongest existing bounds (those of [223, 228, 230]) used the X-ray observations of LMC, Milky Way and Andromeda galaxy whose effective exposure was below 200 ksec (see Table 4.7)[10]

In this situation the current generation of X-ray telescopes there are two possible ways to further improve the existing bounds and probe the theoretically interesting regions of particle physics models:

1. Deep (few mega-seconds)[11] observations of the most X-ray quiet objects. "*Classical*" dwarf spheroidal galaxies (Ursa Minor, Draco, Sculptor, Fornax), where the dark matter content can be determined robustly are the preferred targets. The problem with this approach is the limited visibility of some of these objects and large investment (about 10%) of the annual observational time of the satellite (total observational time available each year for *XMM-Newton* and *Chandra* satellites is about half of the calendar year, i.e. 14–15 Msec). Allocating time for such an observation in the absence of a candidate line is hardly possible. On the other hand, observations of these objects would provide an important confirmation of the signal, detected with some other means.

2. Total exposure of all observations of dark matter-dominated objects with the X-ray satellites is several orders of magnitude longer than any possible single observation. Therefore a possible way to advance with the existing X-ray instruments is *to combine a large number* of X-ray observations of different dark matter-dominated objects. The idea is that the spectral position of the dark matter decay line is the same for

---

[10]For Milky Way halo [228], total exposure of the combined blank sky dataset was ~ 547 ks, but due to subtraction of instrumental background with ~ 145 ks exposure, the errorbars of the subtracted spectrum were mainly defined by the exposure of the background.

[11]Even longer exposure will not improve the situation, as the error bars will begin to be dominated by systematic uncertainties, see the next Chapter for detailed discussion.

all these observations, while the astrophysical backgrounds in the combined spectrum would "average out", producing a smooth continuum against which a small line would become visible. Naively, such a data-set, uniformly processed, should allow to improve the existing bounds by at least an order of magnitude *and* study spatial dependence of each candidate line.

3. Finally, drastic improvement in the decaying dark matter search is possible with a *new generation of spectrometers*, having large field of view and energy resolution close to several eV [75, 229, 365, 366]. In Chapter 4, we discuss this possibility in more details.

Chapter 5

Analysis of combined dataset

In this Chapter we perform the search for dark matter decay lines in X-rays at energies 2.8 − 10.8 keV, by stacking the X-ray spectra of *nearby spiral and dwarf galaxies* observed with *XMM-Newton*. To this end we collect several hundreds observations of nearby galaxies. After careful data reduction (removing point sources, time variable component and other sources of contamination) we end up with the dataset of about 400 observations with the total *cleaned* (usable) exposure of about 6 Msec (about two orders of magnitude longer than any single observation with *XMM-Newton*). Large number of counts in each energy bin corresponds to the *statistical error* at the sub-per cent level. We build a spectrum of the combined dataset and demonstrate that we are able to describe it with a simple, physically motivated model, so that all the remaining residuals (i.e. systematic errors) remain at a comparable (sub-per cent) level. Careful analysis of this dataset reveals a number of line-like residuals at the level $2 - 3\sigma$. We investigate each of these candidates and demonstrate that none of them can be interpreted as an astrophysical line, originating from dark matter decays. The resulting limits on the flux in lines are at the level of about several $\times 10^{-6}$photons/sec/cm^2 (apart from the bins where strong instrumental lines are present), which constitute as much as an order of magnitude improvement compared to the existing bounds.

The rest of this Chapter is organized as follows. We discuss the choice of targets in Sections 5.1. Our data reduction technique is presented in Section 5.2. Section 5.3 is devoted to the description of the stacked spectrum of all galaxies. Section 5.3.1 describes in details our approach to modeling the spectrum. Finally, in Section 5.5 we discuss our results: detected weak lines,

their possible origin and resulting bounds on the line flux.

5.1 Selecting objects for the combined dataset

Using the archive of X-ray observations of the *XMM-Newton*, it is possible to collect about 20 Msec of the nearby spiral and irregular galaxies[1]. The choice of the objects was dictated by several considerations:

- the absence of too many bright point sources. Indeed, removal of each point source leads to the decrease of the field-of-view and of dark matter decay signal (proportional to the FoV) by about 0.5%.[2] Therefore, for the large amount of removed point sources the expected signal to noise starts to decrease (see e.g. the analysis of [230]).

- the absence of prominent diffuse emission at energies of interest. This requirement restricted our attention to galaxies, whose diffuse emission is concentrated in soft X-ray band (below $\sim 2\,\mathrm{keV}$), thus discarding not only observations of clusters, but also of giant elliptical galaxies.

- angular size of the object should be sufficiently large to cover the FoV of the *XMM-Newton* EPIC camera ($\sim 26'$ in diameter). If the solid angle spanned by the characteristic size of dark matter distribution r_* is much bigger than the FoV of the satellite, the uncertainty of exact modeling of dark matter distribution at the centers of galaxies become significant. If, on the other hand, the characteristic scale is much smaller than the FoV, one looses the signal (which scales as $\Omega_{\mathrm{fov}} \times \bar{\mathcal{S}}$, see Eq. (3.3)). Therefore, optimal objects are those whose characteristic radius of dark matter distribution is of the order of the radius of the FoV – the nearby galaxies.

We saw in Chapter 3 that the dark matter column density in of the Milky Way halo is comparable to the signal from other objects (see also [223, 228, 231, 367]). Therefore we start with collecting *recent* results on the Milky Way dark matter distributions and analyzing the uncertainties of the corresponding column density estimates. We then continue with identifying the galaxies, whose expected decay signal would be comparable (constitute a sizable fraction) of the Milky Way's contribution in their direction. Section 5.1.5 summarizes our dataset.

---

[1]We do not consider galaxy clusters, as their strong X-ray background would require a different type of analysis.

[2]The point spread function of the *XMM-Newton* (encircled 90% of photon energy) is 40-60 arcsec and we remove circle with the radius $1'$ around each point source.

Reference	Type	$\rho_s(\rho_c)$, $10^6 M_\odot/\mathrm{kpc}^3$	$r_s(r_c)$, kpc	$r_\odot$, kpc
[194]	NFW	4.9	21.5	8.0
[194][a]	NFW	0.60	46.1	8.5
[370]	NFW	13.3	14.7±0.7	8.0
[371]	NFW	27.2±15.0	10.2±6.1	7.5
[372][b]	NFW	4.74±0.57	21.0±3.2	8.0
[373]	ISO	24.5±2.5	5.5±0.6	8.0
[374]	NFW	20.4±2.6	10.8±3.4	8.33±0.35
[375]	NFW	12.5±6.0	17.0±3.9	8.33±0.35

Table 5.1: Parameters of dark matter profiles for Milky Way galaxy. Here, ρ_s (ρ_c) and r_s (r_c) denote the characteristic density and radius of the NFW (ISO) dark matter distributions, see Eq. 3.8 and Eq. 3.11, respectively, $r_\odot$ is the distance to Galactic Centre.

[a] Maximum disk profile.

[b] Mass-concentration relation between distribution parameters is assumed.

5.1.1 Milky Way galaxy

The mass modeling of the Milky Way is continuously updated and improved (see e.g. [194, 195, 368–375]). In Table 5.1 we summarize recent results. For each of the profiles the dark matter column density is calculated using the expression (3.5). The results are shown in Fig. 5.1. The behaviour of cored (ISO) and cusped (NFW) profiles differs at small ϕ. Notice that the difference becomes much less profound if the column density is averaged over the field of view of *XMM-Newton* (radius $15'$). In what follows we only consider observations with the off-center angle $\phi \gtrsim 45°$.

As we see from Fig. 5.1, *the most conservative values of dark matter column density in this region of ϕ is given by the NFW profile from [372]*. For comparison, we also show in Fig. 5.1 the most "extreme" case of Milky Way mass modeling — the maximal disk distribution of [194].[3] This model is highly implausible, in particular because the maximal disk would be unstable (see [194] for discussion). We do not use this profile in our calculations and keep it to demonstrate the level of uncertainties.

---

[3]In calculating the dark matter column density for this profile we did not take into account additional effect of adiabatic contraction, so the actual signal is stronger in the center.
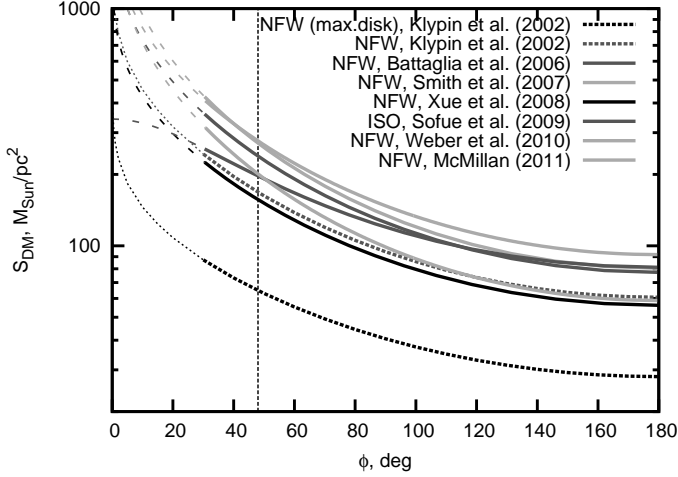
Figure 5.1: Comparison of different dark matter column density distributions of the Milky Way halo as a function of the off-centre angle ϕ (see Eq. (3.6) for its definition). All observations in our combined dataset have the angle $\phi > 48°$ (to the right of vertical line). We adopt profile "NFW, Xue et al. (2008)" [372] as the most conservative column density estimate. We also show (in black dotted line) the most extreme case – the maximal disk profile from [194]. This model is unphysical, designed solely to minimize the dark matter content, and is only showed for demonstrate the level of uncertainties, which is less than a factor of 2 even in this case.

5.1.2 Galaxies of the Local Group

Among all objects that we choose for the combined dataset, there are three objects that are parts of the Local group: Large and Small Magellanic Clouds and the Andromeda galaxy. These objects are special in a number of ways. First of all, their dark matter halos have size about several degrees – much larger than the *XMM-Newton* field-of-view. Therefore, if a candidate line is found, its surface brightness in these objects can be studied. Secondly, large X-ray surveys had covered significant fractions of these galaxies [376–378]. Finally, as we are going to see, these objects have dark matter column density similar (or greater) than the Milky Way's contribution in this direction, thus significantly increasing the expected signal.

Reference	Type	$\rho_s(\rho_c)$, $10^6 M_\odot/\mathrm{kpc}^3$	$r_s(r_c)$ kpc
[285]	NFW	37.0	8.18
[285]	NFW	47.1	7.63
[285][a]	NFW	2.11	28.73
[298]	BURK	57.2	6.86
[298]	NFW	17.4	12.5
[11][b]	BURK	2.915	28
[11][c]	NFW	4.81	22.952

Table 5.2: Parameters of dark matter profiles for M31 used in this Chapter.

[a] Maximum disk profile.

[b] Mass-radius relation between distribution parameters is assumed.

[c] Mass-concentration relation between distribution parameters is assumed.

5.1.2.1 Andromeda galaxy

The dark matter distributions for the Andromeda galaxy was extensively discussed in Sec. 4.1.3.1. We reproduce it here, adding several new profiles and discarding the dark matter distributions from [12] because of bad quality of fit. The results and their uncertainties are summarized in Table 5.2. We adopted the distance to M31 $D_{\mathrm{M31}} = 785$ kpc [379]. Dark matter column density profiles as a function of the off-center angle within Andromeda halo are shown in Fig. 5.2. The BURK profile from [11] is used as the most conservative one, similarly to Sec. 4.1.3.1.

5.1.2.2 Large and Small Magellanic Clouds

For LMC, we used the dark matter density distribution parameters from [380–382], see Table 5.3 for details. The results for dark matter column density are shown in Fig. 5.3.

For SMC, we used the dark matter density distribution parameters from [384], see Table 5.4 for details. The results for dark matter column density are shown in Fig. 5.4.

Our analysis shows that both LMC and SMC dark matter content is highly uncertain. Therefore, while it is natural to expect a significant boost of a signal (and thus include these objects as a part of the dataset), in deriving conservative bounds, one has to assume negligibly small content of
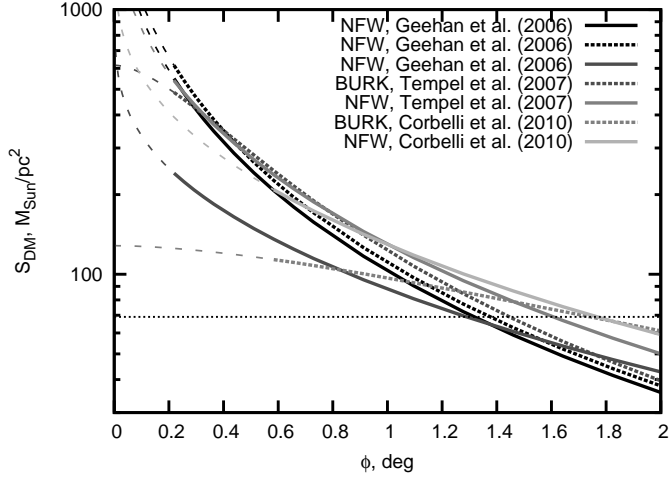
Figure 5.2: Dark matter column density in the Andromeda galaxy, based on the different dark matter distributions, described in Table 5.2. The BURK profile from [11] is the 'minimal' dark matter model used in [323], see also Sec. 4.1.3.1 for details. Here, we adopt this profile as the most conservative estimate. Horizontal line shows the minimal contribution from the Milky Way halo in direction of M31, the most conservative profile from [372], see Fig. 5.1 for details.
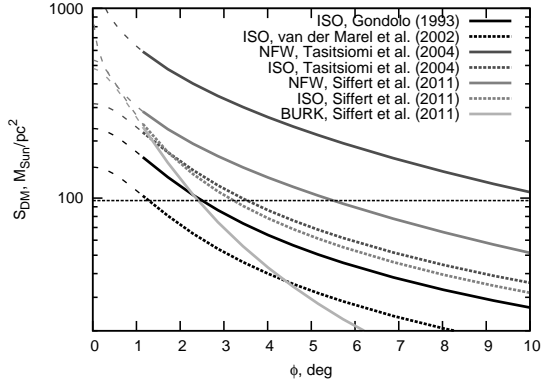

Figure 5.3: Comparison of different dark matter column density distributions of the Large Magellanic Cloud. The parameters of these profiles are described in Table 5.3. Horizontal line shows the minimal contribution from Milky Way halo in the direction of LMC, using the most conservative profiles from [372], see Fig. 5.1 for details.

Reference	Type	$\rho_s(\rho_c)$, $10^6 M_\odot/\mathrm{kpc}^3$	$r_s(r_c)$ kpc
[380][a]	ISO	74	1
[383]	ISO	46.3	1
[381][b]	NFW	16.6	9.16
[381]	ISO	100	1
[382]	NFW	8.18±2.67	9.04±2.43
[382][c]	ISO	326±65	0.52±0.076
[382][c]	BURK	289±51	1.06±0.13

Table 5.3: Parameters of dark matter profiles for LMC.

[a] Halo radius is uncertain $\lesssim 10$ kpc, only combination $\rho_c r_c^2$ is measured.

[b] Minimal disk assumption.

[c] Bad quality of fit.

Reference	Type	$\rho_s(\rho_c)$, $10^6 M_\odot/\mathrm{kpc}^3$	$r_s(r_c)$ kpc
[384][a]	NFW	4.1	5.1
[384][b]	BURK	21.4	3.2

Table 5.4: Parameters of dark matter profiles for SMC used in this Chapter.

[a] Bad quality of fit.

[b] Best-fit relation between distribution parameters is assumed.

dark matter, using only Milky Way's column density in the direction of these objects.

5.1.3 Galaxies with measured dark matter distribution

We collect the dark matter distributions of galaxies, using the catalogue compiled in Chapter 3. We derive the *average* dark matter column density inside a circle with radius $15'$, corresponding to the FoV radius for *XMM-Newton* imaging spectrometers. To be conservative, we use *truncation of cuspy profiles* (NFW). Namely for $r > r_s$ the average dark matter column density coincides with the NFW expression while for $r \leq r_s$ it remains *constant* (similar to cored profiles).
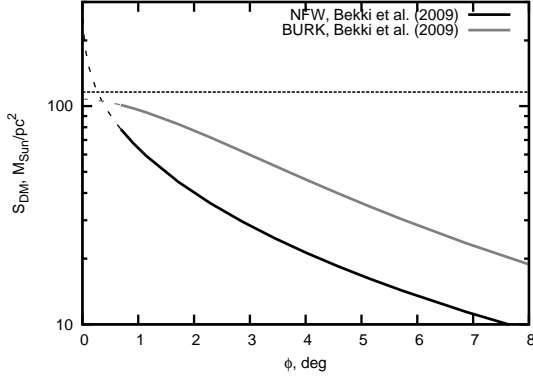
Figure 5.4: Comparison of different dark matter column density distributions for the Small Magellanic Cloud. The parameters of these profiles are described in Table 5.4. Horizontal line shows the minimal contribution from the Milky Way halo in the direction of SMC, using the most conservative profile from [372], see Fig. 5.1 for details.

5.1.4 Galaxies with unknown matter distribution

Apart of galaxies with known dark matter distributions, for a large number of nearby galaxies that fall within the FoV of *XMM-Newton* do not have available data for dark matter density profiles. To *estimate* the dark matter distribution parameters for these galaxies, we used the following procedure.

We took the values of galaxy optical radius r_{opt} obtained from the apparent angular diameter, `logdc` (corrected for the galactic extinction and inclination effect) from the `HyperLeda` database.[4] The distance to the galaxy was also obtained from HyperLeda database either from "true" distance modulus `mod0` (when available) or from redshift distance modulus `modz` for sufficiently distant galaxies (with $cz \geq 200$ km/s). This results in more than 5×10^4 galaxies with known `logdc` values.

Then, using the sample of 92 spiral and elliptical galaxies from our catalogue, complied in Chapter 3, we study log-log correlations of r_{opt} with r_* and $\mathcal{S} \propto \rho_* r_*$.[5] The best-fit parameters of the correlations (see also Fig. 5.5 for

---

[4] http://leda.univ-lyon1.fr

[5] Recall that the parameters ρ_* and r_* coincide with the parameters ρ_s and r_s correspondingly for the NFW distribution. For other distributions, see Section 3.12 for details.
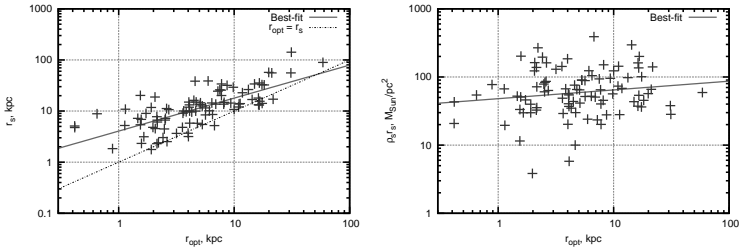
Figure 5.5: *Left:* Correlation between the optical radius r_{opt} defined with the help of HyperLeda database and characteristic size of galactic dark matter haloes r_* compiled from dark matter catalogue of Chapter 3. The best-fit values are presented in Eq. 5.1. Note that for most of the objects $r_* > r_{opt}$, in agreement with expectations. *Right:* The same correlation but with $\rho_* r_*$, a proxy for dark matter column density $\mathcal{S}$.

details) are:

$$\log_{10}\left(\frac{r_*}{1\,\mathrm{kpc}}\right) = 0.646 \times \log_{10}\left(\frac{r_{opt}}{1\,\mathrm{kpc}}\right) + 0.607;$$

$$\log_{10}\left(\frac{\rho_* r_*}{1 M_\odot/\,\mathrm{pc}^2}\right) = 0.129 \times \log_{10}\left(\frac{r_{opt}}{1\,\mathrm{kpc}}\right) + 1.68. \tag{5.1}$$

Finally, the correlations Eq. (5.1) are then used to determine the parameters of dark matter density distributions for about 5×10^4 galaxies not present in our dark matter distribution catalogue. Namely, we choose such objects for which angular size of $r_* \gtrsim 15'$ and then estimate its column density. We sub-select only those galaxies that have estimate $\mathcal{S} \geq 30 M_\odot\,\mathrm{pc}^{-2}$.

5.1.5 Combined dataset: summary

All together our procedures, outlined in Sections 5.1.1–5.1.4 resulted in the sample of **111** galaxies, see [385] for details. By using HEASARC browsing form [386], we selected all of them observed by *XMM-Newton* with a pointing centered inside a circle with the radius $r_*/D + 15'$ from the centre of a given galaxy. Such a selection finds observations covered the innermost part of the dark matter halo of the object. This results in 70 galaxies observed by *XMM-Newton*. 61 of them are included in our final dataset, see [387] for details.

Total *uncleaned XMM-Newton* exposure of these galaxies is ~ 19 Ms.

About 50% of this exposure is concentrated on three galaxies with the largest angular size of the dark matter halo – Large Magellanic Cloud (LMC), Small Magellanic Cloud (SMC) and Andromeda galaxy (M31).

5.2   Data processing

5.2.1   Downloading and preprocessing *XMM-Newton* data

We use the data obtained with the European Photon Imaging Camera (EPIC) of *XMM-Newton*, which consists of two MOS [388] and one PN [389] CCD cameras (sensitive in the 0.1-15 keV energy range) behind X-ray telescopes [390]. We download the basic Observation Data Files (ODF) for 725 publicly available (on April 16 2012) *XMM-Newton* observations for 70 galaxies selected in previous Sec. 5.1 using the web search form of NASA's High Energy Astrophysics Science Archive Research Center (HEASARC) [386]. In accordance with startard data analysis prescription, see e.g. Sec. 4.3 of [391], we produced *calibrated concatenated event*[6] *lists* using the standard data reduction procedures[7] `emproc` and `epproc` for MOS [388] and PN [389] cameras of *XMM-Newton*/EPIC, respectively. These procedures include combining data from all CCDs for each camera (MOS1, MOS2, PN), identification and rejection of bad CCD pixels, calculation of event coordinates using telescope attitude information and improving the quality of PN data at low energies.

The filtered event lists are then used for timing and spatial variability filtering described in the next Sec. 5.2.2 and Sec. 5.2.3. The main statistical properties event lists before and after the cleaning procedure are given in Table 5.5. The detailed parameters of the *filtered* event lists are presented in [387].

---

[6]Here, an "event" is a result of instantaneous positive detection in one or several adjacent CCD pixels. According to Sec.4.4 of [391], storing detector data in format of events is motivated by telemetry contraints of the *XMM-Newton* satellite. Indeed, according to [334] the procedure based on analysis of event patterns allows to reject of about 99% of events caused by high-energy (~ 100 MeV) cosmic rays thus significantly reducing the amount of data telemetry.

[7]These procedures are the part of the standard publicly available software of *XMM-Newton* data analysis, Science Analysis System (SAS) v.11.0.0 [392].

5.2.2 Removing time-variable component

Raw event lists, generated using the standard pipeline (see Sec. 5.2.1 for description), exhibits significant time variability, both in short ($\lesssim 10$ ks) and long ($\gtrsim 10$ ks) scale variability. According to [325], the short-scale time variability is caused by the soft solar protons with the energies about few 100 keV. The countrate spectrum of these *soft proton flares* has unpredictable shape although it can be approximated by broken powerlaw with $E_{break} \simeq 3.2$ keV [329]. Moreover, according to our findings in Sec. 4.1.5 (see also [323]), residual soft proton flare contamination is also responsible for (at least) the broad line-line feature at 2.5-2.6 keV, where the effective area has a local minimum due to Au K edge. The count rate of the decaying dark matter signal should be of course constant in time and therefore we aim to clean the time variability as much as possible.

A number of different methods of removing time-variable component has been developed (Appendix 8.4.1 provides a brief overview of available procedures). Here we apply the following procedure. First, by using the 60 s histogram for the whole energy range (0.2–12 keV for MOS and 0.15–15 keV for PN camera) we reject the countrates differing from the mean value at more than 1.5σ. This is done with the help of standard procedure `espfilt` [393]. This procedure removed 34%, 33% and 43% of total observation time for MOS1, MOS2 and PN cameras, respectively (see Table 5.5 for details). The subsequent visual inspection of cleaned lightcurves showed the absence of any significant time variability. To further clean the residual soft proton component, we apply the procedure of [330]. It is based on comparison of high-energy (6-12 keV for MOS, 5–7.3 and 10–14 keV for PN) countrates for "in-FoV" (10-15 arcmin off-center) and out-FoV CCD regions, using their public script [331][8]. Fig. 5.6 shows the obtained dependence on $F_{in} - F_{out}$ ratios from F_{in} in MOS and PN cameras. In accordance with [330], we selected observations with $F_{in} - F_{out}$ less than 1.50 (marked by horisontal line). In addition, we removed observations with $F_{in} \geq 0.35$ cts/s for MOS and 1.2 cts/s for PN camera (marked by vertical lines in Fig. 5.6) which show significant large-scale variability at high energies.

The final step of removing large-scale time variability is made after re-

---

[8]This script does not take into account the damage of MOS1 CCD6 on 09 March, 2005, see [394, 395] for details. According to [331], the relative error on MOS1 $F_{in} - F_{out}$ ratio after the damage is about 10 %.
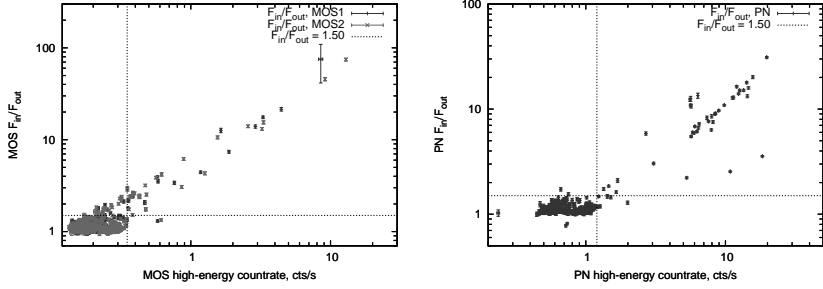
Figure 5.6: F_{in}/F_{out} for MOS (*left*) and PN (*right*) cleaned event lists as functions of F_{in}. The adopted selection criteria on $F_{in}/F_{out} \leq 1.30$ proposed by [330] are also shown. Additionally, we select observations having $F_{in} \leq 0.35$ cts/s for MOS and $F_{in} \leq 1.2$ cts/s for PN camera, shown by horizontal lines.

moving observations with significant changes of instrumental background flux [325, 352]. As a result, our filtering leaves 359 MOS1, 327 MOS2 and 321 PN cleaned event lists, see Tables 5.5 and [387] for details.

The mean value of $F_{in} - F_{out}$ ratio for our dataset is 1.13 ± 0.11 for MOS1, 1.10 ± 0.10 for MOS2 and 1.12 ± 0.10 for PN camera, see Table 5.5 for details. The histogram of observations basen on their $F_{in} - F_{out}$ ratios is shown in Fig. 5.7.
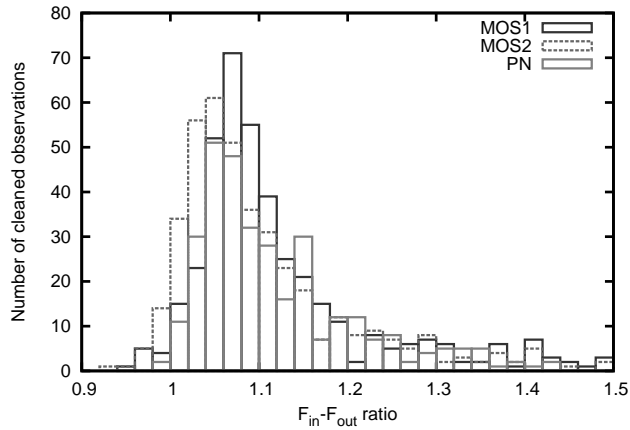
Figure 5.7: Histogram of the distribution of MOS1, MOS2 and PN observations as function of their $F_{in} - F_{out}$ ratio for dataset.

5.2.3 Filtering spatial variability.

Presence of spatial variability may significantly affect our results due to narrow emission lines from astrophysical sources. Indeed, as we see from left Fig. 5.8, the 2.5-6.0 keV brightness (flux per unit solid angle) *before* filtering spatial variability is about 4-72 (MOS) and 10-180 (PN camera). This is much larger compared to typical values for blank-sky dataset [327] (excluding Galactic Centre region): 5-10 (MOS) and 30-48 (PN camera). Therefore, additional cleaning of spatial variability should be performed.
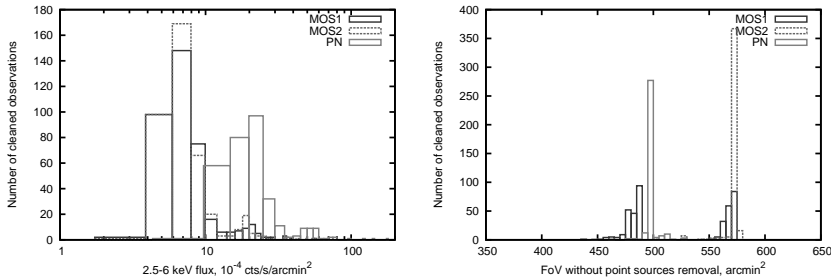
Figure 5.8: *Left*: histogram of the distribution of MOS1, MOS2 and PN observations as function of their 2.5-6.0 keV flux *before* spatial variability cleaning. These values are considerably larger than the typical values for blank-sky spectra, about $5\text{-}10\times10^{-4}$ cts/(s arcmin^2) for MOS and $30\text{-}48\times10^{-4}$ cts/(s arcmin^2) for PN camera (excluding Galactic Centre region), according to Table 3 of [327], so additional cleaning for spatial variability should be performed. *Right*: histogram of the distribution of MOS1, MOS2 and PN observations as function of the size of their field-of-view.

In the literature, we identifed the following sources of spatial variability:

1. Bright strips in PN camera caused by out-of-time events (see Sec.4.10 of [391]);

2. Anomalous CCD states [329, 353];

3. Point and extended astrophysical sources.

The *out-of-time events* are caused by photons coming during the CCD readout phase, see Sec. 4.10 of [391] for details. During the readout time, these events assign the wrong number of a detector coordinate RAWY and thus wrong energy correction value. As a result, out-of-time events form bright strips in images parallel to CCD borders. The fraction of out-of-time

events depends on observation mode according to Sec. 3.3.10 of [320], it is the largest for Full Frame (6.3 %) and Extended Full Frame (2.3 %) modes for PN camera. For these modes, we correct PN spectra with the standard procedure [324] by creating the simulated out-of-time event list, producing its properly scaled spectrum (using the same detector coordinates as in the source file) and subtracting it from the source spectrum.

Anomalous CCD state appears for some observations, where the countrate for some CCDs is significantly larger than for nearby CCDs. According to [329, 353], the anomalous states significantly affect the CCD countrate for $E \lesssim 1.0$ keV. Because here we concentrate on $\gtrsim 2.8$ keV energy range, we do not exclude the corresponding CCDs from the subsequent analysis.

Due to instrument diffraction and mirror defects, *astrophysical point sources* appear to have finite size. It is determined by the *point spread function* (PSF) [9] and is usually about several tens of arcsecs, much larger than the size of a CCD pixel. This allows to detect the point source by comparing the countrate in several adjacent pixels with that of background. However, this algorithmical procedure is complicated by the precence of CCD gaps, bad pixels, spatial vignetting[10]. We identified point astrophysical sources using standard *XMM-Newton* SAS metatask edetect_chain [396]. To increase the sensitivity with respect to point source detection, we used simultaneously MOS and PN cameras. We excluded all point sources detected in a circle with 14 arcmin radius[11] at $\gtrsim 4\sigma$ level together with 60-arcsec circular regions centered at the their positions. According to Sec. 3.2.1 of [320], such circle contains more than 90 % of source energy up to off-axis angle of 10 arcmin (MOS) or up to 3 arcmin (PN camera). Subsequent visual inspection has not found significant remaining point sources.

To check for *extended astrophysical sources*, we first calculated 2.5-6 keV brightness and compared it with *blank-sky* dataset of [327]. The solid angle covered by field-of-view is calculated with standard backscale procedure [397]. Before point source subtraction, the field-of-view solid angles are distributed according to right Fig. 5.8. Notably, all of them are somewhat smal-

---

[9]For the shapes and extents of the MOS and PN point spread functions, see Sec. 3.2.1 of [320].

[10]Due to vignetting effect, the off-axis effective area of a telescope significantly (up to 2-3 times) decreases with increase of off-axis angle. This effect also strongly depends on energy, see Sec. 3.2.2 of [320] for details.

[11]This is somewhat smaller than the radius *XMM-Newton* field-of-view ($\simeq 15$ arcmin) due to slightly different geometries of MOS and PN cameras.

ler than the naive estimate for a solid angle of a circle with 14 arcmin radius ($\pi \times 14^2 = 616$ arcmin^2) due to

- CCD gaps;

- bad pixels;

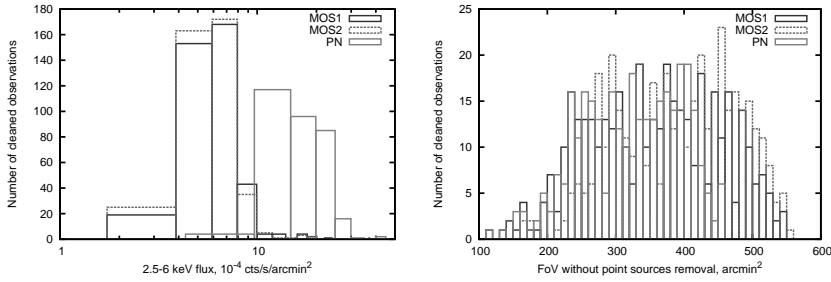- loss of MOS1 CCD6 since 09 March, 2005, see [394] for details.

Figure 5.9: *Left*: histogram of the distribution of MOS1, MOS2 and PN observations as function of their 2.5-6.0 keV brightness *after* spatial variability cleaning. The results are close to typical values for blank-sky spectra, about $5\text{-}10\times10^{-4}$ cts/(s arcmin^2) for MOS and $30\text{-}48\times10^{-4}$ cts/(s arcmin^2) for PN camera (excluding Galactic Centre region), according to Table 3 of [327]. *Right*: histogram of the distribution of MOS1, MOS2 and PN observations as function of their field-of-view *after* spatial variability cleaning.

The distribution of X-ray brightness in 2.5-6 keV *after* subtraction of point sources becomes consistent with expectations from blank-sky dataset of [327], see left Fig. 5.9. However, by looking at temporal variations of X-ray brightness, see Fig. 5.10 it is possible to select several dozens of clear "outliers".

5.2.4 Producing raw spectra and response files

Event lists filtered from time and spatial variability (see previous Sections 5.2.2 and 5.2.3 for detailed description of cleaning procedure) are then used to produce spectra of individual observations. In an event list, each event contains information about *Pulse Height Invariant* (PI) – corrected and recombined (for non-single events) event energy. The standard procedure `evselect` [398] creates a histogram of events using their PI values in a
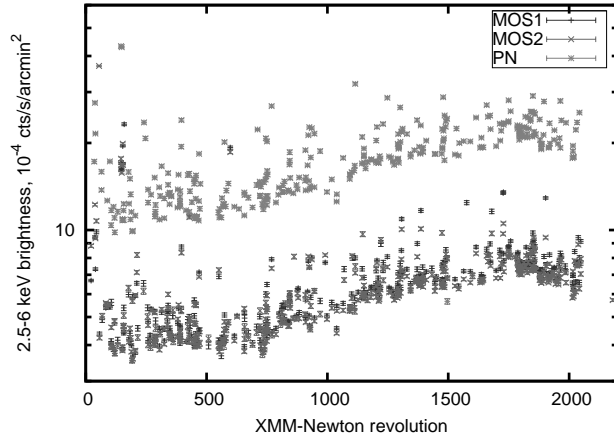
Figure 5.10: Temporal variation of X-ray brightness after subtraction of point sources (see Fig. 5.9), as a function of *XMM-Newton* revolution number. The errors are at 1σ level. Unlike Fig. 5.9, a number of "outlier" observations is clearly visible. For subseuqent analysis, we remove all these outlier observations.

pre-defined energy range with given binning interval. We use default values for energy ranges and binning intervals recommended by *XMM-Newton* SAS team. Namely, MOS spectra are binned by 15 eV in interval 0-11999 eV, PN spectra – by 5 eV in interval 0-20479 eV. This gives 800 energy channels for MOS and 4096 channels for PN camera.

In general, the difference between PI energy and actual photon energy includes the following effects:

1. Quasi-gaussian broadening of a narrow energy line with full width at half-maximum (FWHM) ~100-200 eV, see e.g. Sec. 3.3.4 of [391];

2. Low-energy tail probably caused by incomplete charge collection for X-rays absorbed near CCD surface layer, see e.g. [399, 400].

3. Si fluoresence (at 1.740 keV) and Si escape (at $E - 1.740$ keV) peaks for input energies larger than the Si K edge at 1.839 keV, see [389, 401] for details. The intensity of Si escape peak may be at the order of several % of the main peak [402].

To model these effects, the *redistribution matrix file (RMF)* should be created. It contains the probability of the photon with *physical* energy between
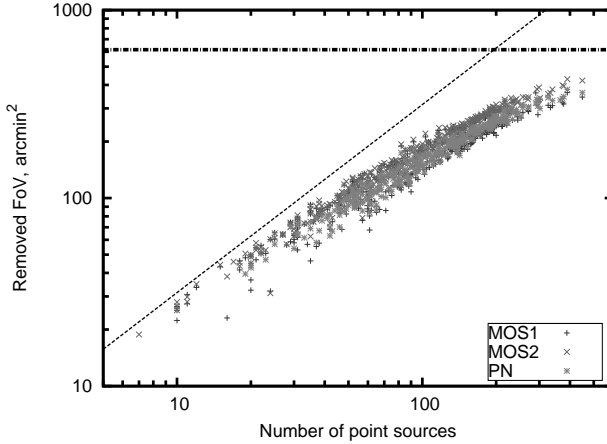
Figure 5.11: Part of the FoV, removed with point sources, as a function of the number of detected sources. Horizontal dashed-dotted line shows the full FoV of EPIC camera (circle with the radius of $13'$). Dashed line shows the upper bound of removed FoV fraction ($3.14\,\mathrm{arcmin}^2$ per source, provided that the $1'$ circles around sources do not overlap and there are no CCD gaps, bad pixels, etc.). As expected, for large number of removed sources, 1 arcmin circles around them overlap.

E and $E + \Delta$, where Δ is the size of the energy bin to be detected in spectral bin I. According for stardard prestrictions for analysis of extended sources, we simulated RMF files for each observation and camera (MOS1, MOS2, PN) using the standard *XMM-Newton* SAS task `rmfgen` [403] taking into account spatial distribution of the photons.

Then, to convert the obtained countrates (in cts/s) to fluxes (in cts/s/cm^2) we simulated files containing information about the effective area (ancillary response function, ARF) taking into account

1. Spatial distribution (to correct for PSF and telescope vignetting);

2. Quantum efficiency of the CCDs;

3. Presence of bad pixels;

4. Filter transmission efficiency [12];

[12]To attenuate the large photon countrates at low energies ($\lesssim 1$ keV), several filters (Thin, Medium, Thick) are used. According to Sec. 3.3.6 of [320] the difference between the effective area for different filters is $\lesssim 10\%$ for $E \gtrsim 2$ keV, so we do not make any differences between
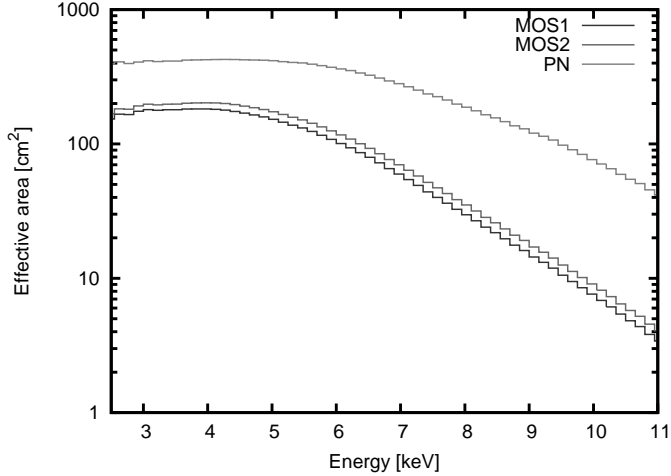
Figure 5.12: Exposure and FoV-weighted mean effective area for MOS1, MOS2 and PN cameras, as functions of energy. Note much larger effective area for PN camera at $E \gtrsim 5$ keV, compared to that of MOS cameras.

5. Correction for Out-of-time events (significant for PN Full Frame and Extended Full Frame observation modes).

Similar to RMF generation, we simulate ARF files for each observation and camera using the standard *XMM-Newton* SAS task `arfgen` [404].

The obtained spectra, together with RMF and ARF files, will be used for further modeling. The first step is to prepare combined spectrum of all observations for each of *XMM-Newton*/EPIC cameras (MOS1, MOS2, PN). Because the default size of binning intervals is much smaller than the energy resolution of the instrument, it lead this leads to significant oversampling of the data because the adjacent spectral bins are strongly correlated with each other. Therefore, we *rebin* the combined spectra into the larger bins. The size of the bin is a trade-off between oversampling (which is better with increasing the size of the bin) and better knowledge of the spectral line shape (which tends to decrease the size of the bin). As a result, we selected the size of the bin to be 60 eV for both MOS and PN cameras. The resulting spectra are shown in Fig. 5.13.

the observations with different filters.

	MOS1	MOS2	PN
Cleaned event lists	715	719	664
Raw exposure, ks	18756	19762	15908
Cleaned exposure, ks	12326	13193	9020
Fraction of exposure, affected by flares	34%	33%	43%
Small FoV cleaned event lists	175	167	138
Small FoV exposure, ks	2209	2374	1883
Short (< 5 ks) observations	113	104	154
Total exposure of short observations, ks	273	254	338
Full FoV Cleaned event lists	427	448	372
Full FoV exposure, ks	9844	10565	6799
Average $F_{in}-F_{out}$ of final dataset	1.13 ± 0.11	1.10 ± 0.10	1.12 ± 0.10
Average FoV before point sources removal, arcmin^2	518.0	566.4	498.4
Average FoV after point sources removal, arcmin^2	374.3	404.5	347.0
Number of event lists in the final dataset	359	327	321
Exposure of the final dataset, ks	8740	8241	5800

Table 5.5: Statistical properites of the combined dataset during the main stages of our analysis. See [387] for the basic properties of selected observations.

(a) Count rate per bin in each of the EPIC cameras (binned in 60 eV)

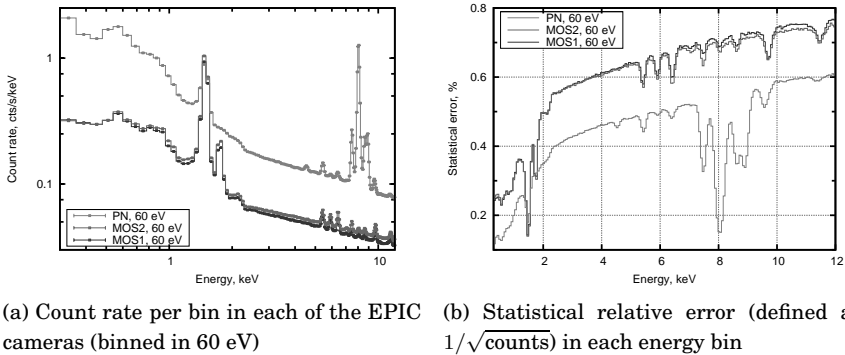(b) Statistical relative error (defined as $1/\sqrt{\text{counts}}$) in each energy bin

Figure 5.13: Combined spectra for MOS1, MOS2 and PN cameras for our final dataset (see Table 5.5 for details). Strong instrumental lines are clearly visible in spectra of all cameras. Right panel shows the statistical relative error in each bin.

## 5.3 Spectral analysis of combined dataset

In this Section, we construct a model of co-added spectrum of all observations for each of the *XMM-Newton* EPIC cameras (MOS1, MOS2, PN) , using a simple `powerlaw` continuum model with a sum of several finite width `gaussians` in positions of bright instrumental lines (Sec. 5.3.2). The model is compiled in such a way that the large ($\gtrsim 2\sigma$) *negative* residuals are absent in the spectrum. The value of the systematic error is then estimated in Sec. 5.3.5. According to obtained value of systematic errors, we determine our criterium for line candidates. The total list of line candidates passing our criterium is then discussed, including comparison between different cameras and with closed-filter dataset 5.5.

### 5.3.1 An overview of existing approaches to study weak diffuse X-ray signals

The resulting spectrum of our combined dataset (with counts co-added by PI channels and then grouped to get 60 eV energy bins) is shown in Fig. 5.13. It has a shape, qualitatively similar to that of the blank sky dataset (cf. e.g. [327]): a continuum component plus a number of prominent lines. It is known that there are three major components of the "blank sky" spectrum — Galactic diffuse background, extragalactic diffuse background and instrumental (particle) background [325–327, 329] — and it is clear that our
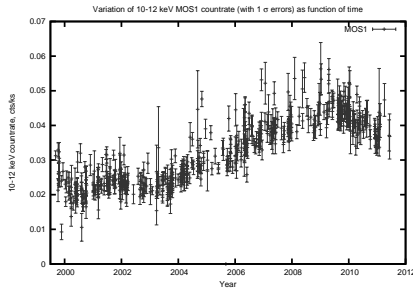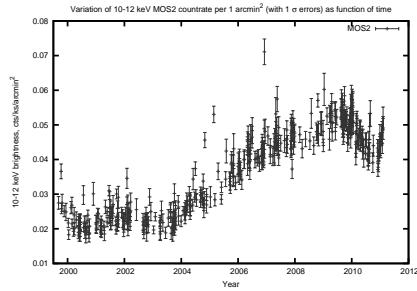
(a) Count rate for MOS1 camera in counts/sec
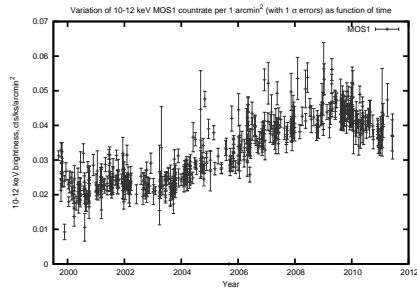
(b) Count rate per unit solid angle for MOS1 camera in counts/sec/arcmin^2
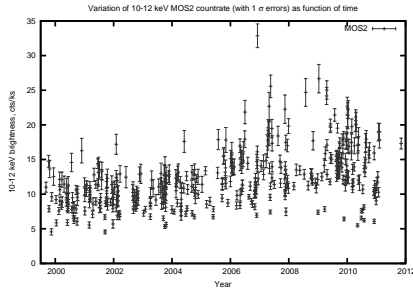
(c) Count rate for MOS2 camera in counts/sec

(d) Count rate per unit solid angle for MOS2 camera in counts/sec/arcmin^2

Figure 5.14: Count rate at high energies (interval 10–12 keV,*MOS1 and MOS2 cameras*) in counts/sec (left panels) and in counts/sec/arcmin^2 (right panels) as a function of revolution. Left panels may look like a random noise. However, in the panel (b) a clear long scale trend is visible. Notice that the same trend can be seen in both MOS1 and MOS2 cameras and therefore it is not related to the loss of the CCD6 by the MOS1 camera.

dataset has a similar structure. In particular, at energies below $\sim 1\,\mathrm{keV}$ the Galactic component dominates, while at energies above $\sim 2\,\mathrm{keV}$ the instrumental background becomes the dominant component.

Total cleaned exposure of the combined dataset that we have constructed is between 5.8 Ms (PN camera) and 8.7 Ms (MOS1 camera) (see Table 5.5). This large exposure (essentially two orders of magnitude longer than the exposure of a typical *XMM-Newton* observation) means that the statistical errors in each energy bin are extremely small (between 0.1% and 0.8% for 60 eV binning, as Fig. 5.13b demonstrates). To extract meaningful bounds

from such large-exposure dataset one should be able to control systematics at a comparable level.[13]

Usually to study the diffuse signals, one subtracts from the raw spectra either "closed filter" background (i.e. particle-induced background) or "blank-sky" background (i.e. a combination of many observations without prominent sources and low level of diffuse emission). In our case neither of these approaches are applicable.

Indeed, the blank sky data would contain decaying dark matter line originating from the decays in the Milky Way halo. This fact has been explored before (see [223, 228, 358]) to put the limits on the lifetime of decaying dark matter. Subtracting such data would reduce all the advantages of a large dataset by removing a dominant component of the expected signal and lowering statistics (as the exposure of the latest blank-sky co-added observations is $\sim 2 - 4$ Ms [327]).

An alternative possibility would be to subtract a closed filter observation (as was done e.g. in [228] in search for decaying dark matter). However the exposure of available observations with closed filter is 1.20 Msec, 1.12 Msec, 0.78 Msec (for MOS1, MOS2, and PN cameras correspondingly).[14] As a result, the *subtraction* of rescaled closed filter data would mean ~ 3 times larger errorbars due to larger errors of the closed filter dataset. Moreover, the instrumental component of the *XMM-Newton* background is self-similar only on average, as we can see by comparing high-energy (10–12 keV) count rates of different observations (Fig. 5.14).

Finally, modeling of each individual observation (including ESAS model of instrumental background [329]) looks like a prohibitively challenging task for such a large number of independent observations. Namely, finding un-

---

[13]The level of systematics of the *XMM-Newton* is usually quoted at the level $5-10\%$. Indeed, according to Fig. 8 of the recent EPIC calibration report [339], the energy resolution has been degraded since the instrument launch for ~ 5 % (MOS) and ~ 10 % (PN) camera. According to [337], the flux ratios between different cameras do not change more than by 5 % with time (except 0.2-0.5 keV band, which is due to the known gradual degradation of MOS response matrices with time at these energies) which is the indication of relative stability of the ARF. Absolute effective area is now known with roughly 10 % precision, see [339]. In addition, a known problem with temporal and spatial variations of the MOS responses at energies below 0.5 keV has been fixed several years ago, see [245] for details. The emission of "standard candles" such as e.g. ζ Puppis [405] also remains constant at the level of 5-10%, which is also indication of the ARF stability from observation to observation.

[14]For PN camera we take a *combination* of Full Frame and Extended Full Frame modes as closed filter spectra are essentially the same in these two modes.

derlying spectral models for 399 observations (including parameters of the particle-induced instrumental background that are variable, as we discussed above) is extremely difficult. Moreover, fitting a thin Gaussian line simultaneously to all these observations would not be possible as the relative intensity of such a line is not known (due to the unknown dark matter content of different observed objects).

In this work we adopt a different approach, that allows us to find weak lines in the combined datasets at desired level. We develop a simple phenomenological model of the combined spectra. We then demonstrate that a weak line, present in all observations of the dataset can be successfully recovered at the expected level. Finally, we produce upper limits on flux of such a line from MOS and PN observations and discuss the origin of several candidate lines.

5.3.2 Constructing a spectral model of the combined dataset

For each EPIC camera the data can be described by a simple phenomenological model. A step-by-step construction procedure for individual cameras is discussed below in the Sections 5.3.3–5.3.4.

We model *count rates, normalized per energy bin*. Instead of using standard `RMF` and `ARF` response files we model them ourselves.[15] For each camera we model count rates by a simple `powerlaw` continuum model with a sum of several finite width `gaussians` modeling bright instrumental lines (see e.g. Table 5.6) for details). The resulting model possess the following properties:

1. The number of model free parameters is much smaller than the number of energy bins.
2. Residuals are distributed in such a way that roughly 68% of residuals are smaller than 1σ and roughly 95% of residuals are smaller than 2σ). However, the distribution of our residuals is deliberately skewed towards the increase of positive residuals (see below).
3. There are no significant *negative* residuals (at more than 2σ level in a single or adjacent 60 eV bins).
4. There are no broad *positive* residuals (several bins in a row), however, line-like residuals can remain.

---

[15]For MOS cameras we are using *diagonal RMF* matrices, relating bin numbers with energy as $E_i = 0.06 \times (N_{bin} - 0.5)$ since the width of the bin is 60 eV. For PN camera this turns out to be not enough for strong instrumental lines, see below Sec. 5.3.3.

Element	Energy (keV)	MOS	PN
K Kα	3.314	–	+
Ca Kα	3.692	–	+
Ti Kα	4.511	–	+
V Kα	4.952	–	+
Cr Kα	5.415	+	+
Mn Kα	5.899	+	+
Fe Kα	6.404	+	+
Fe Kβ	7.058	+	–
Ni Kα	7.478	+	+
Cu Kα	8.048	+	+
Zn Kα	8.639	+	+
Cu Kβ	8.905	–	+
Zn Kβ	9.572	–	+
Au Lα	9.713	+	+

Table 5.6: Known instrumental lines for the EPIC MOS and PN cameras in the energy range 2.5–10.8 keV, [329, 389, 406, 407]. The symbols + or – marks whether such a line has been previously detected in the spectrum of the corresponding camera. Some of these lines are actually several narrow lines from the same series with slightly different positions (for example, Kα_1 and Kα_2, see Table V of [408] for details), so we use the position of the strongest line (Kα_1 in our example). First three lines (K Kα, Ca Kα and V Kα) are detected by [389] by using special *calibration closed filter* background spectrum obtained by irradiating the instrument by ^{55}Fe radioactive calibration source. As a result, the intensities of the flourescent lines in calibration closed filter background are much higher compared to usual closed-filter background, so one can easily observe faint instrumental lines. The Fe Kβ line has been previously detected for MOS cameras only, see e.g. Fig. 2 of [329]. Our work find this line for PN camera, see Table 5.7 below (although with much lower significance compared to MOS cameras).

Finally, we lower the level of continuum to reduce the number of negative residuals (all of which then become less than 2σ). In this way we deliberately bias our procedure towards finding small line-like features in out combined dataset.

5.3.3 Constructing a spectral model for the PN combined dataset

In this Section, we describe a step-by-step procedure for constructing a phenomenological model for combined PN dataset binned by 60 eV. The procedure we use for constructing the model is the following

1. The spectrum of the PN camera is dominated by three strong instrumental lines at 8.045, 8.613 and 8.895 keV (with count rates exceeding $1\,\mathrm{cts/sec/cm^2}$, while the average level of continuum in the energy range 2.8–10.8 keV is at the level $0.1 - 0.3\,\mathrm{cts/sec/cm^2}$). Therefore, we start by excluding the 7.56–9.30 keV energy range (this energy range is also excluded from the final restrictions based on PN spectrum extremely low sensitivity). Due to extremely high statistics, the deviations of the shapes of these lines from purely Gaussian form is very large compared to statistical error and therefore they are difficult to model properly. On the other hand, these residuals are not typical for the whole spectrum, so we do not treat them as a systematic error.

2. We use the energy ranges free from the prominent emission lines (2.70–4.35 and 10.05–11.1 keV) to determine parameters of the `power law` continuum component, see Fig. 5.15 for details.

3. We add instrumental lines with the known positions (see Table 5.6) to the `powerlaw` continuum model, with *fixed* parameters, determine line dispersions and normalizations using best-fit procedure. The results is shown in Fig. 5.16a.

4. We compensate two evident line-like residuals by adding two line candidates at 5.0 and 7.075 keV. The fit quality becomes somewhat better, see Fig. 5.16b for details. The significance of these lines is 7.8σ (for 5.0 keV line) and 3.6σ for 7.075 keV line.[16]

5. At this stage we see that there are systematically positive residuals in many consecutive bins, adjacent (left) to the instrumental lines. We assume this extra continuum to be non-Gaussian tails strong instrumental lines at energies. To demonstrate this we generate (using `fakeit` command of `Xspec` three instrumental lines at positions 6.42, 7.456 and 8.045 keV. We use response matrices (RMF) of actual PN observations to reconstruct the correct non-Gaussian shape of the lines.

---

[16]Significance of these lines is defined as $\sqrt{\Delta\chi^2}$ when adding 1 extra degree of freedom (line normalization) to the fit model.

The result is shown in Figs. 5.17. Each of these lines is well described as

$$F(E) = n_1 \times e^{-\frac{(E-E_1)^2}{2\sigma_1^2}} + n_2 \times e^{-\frac{(E-E_2)^2}{2\sigma_2^2}} + n_{\mathrm{br}} F_{\mathrm{br}}(E), \qquad (5.2)$$

where $F_{\mathrm{br}}(E) = (E/E_{\mathrm{br}})^{\alpha_{\mathrm{low}}}$ at $E < E_{\mathrm{br}}$ and $F_{\mathrm{br}}(E) = (E/E_{\mathrm{br}})^{\alpha_{\mathrm{high}}}$ at $E \geq E_{\mathrm{br}}$. The model contains 10 parameters.

6. Next we try to model continuum excess at 5–6 keV (see Fig. 5.16b for details) as a low-energy tail of the non-Gaussian shaped (5.2) of strong instrumental lines at 6.4, 7.5 and 8.0 keV. The results of the modeling are shown in Fig. 5.17. The details of narrow line simulation are described in Sec. 8.4.3. The results are shown in Fig. 5.18.

7. As we can see from Fig. 5.18, extra continuum from instrumental lines is *not* enough to model the 5-6 keV spectrum continuum. The fit can be significantly improved by allowing normalizations of different components in Eq. 5.2 to vary. This results in 6 extra parameters (2 extra normalizations for each of three modeled instrumental lines) but allowing them to very improves the fit quality very significantly. Fig. 5.20 shows that resulting best-fit continuum for instrumental lines is about an order of magnitude higher than in Fig. 5.17.

8. The resulting fit is shown in Fig. 5.19. Now, fit quality becomes much more reasonable than in previous fits, so we improve the residual local excesses by rebinning nearby bins. The goal is to remove all local negative residuals at the level higher than 2σ.[17] For 4.5 and 5.4 keV lines, we rebinned central 3 bins (180 eV) such that central bin has now 120 eV, and off-center – 30 eV each. We have not done it for 9.6 keV bump because it is known that there are two close instrumental line. For $3.12 - 3.24$, $3.24 - 3.36$, $3.36 - 3.48$, $3.54 - 3.66$, $3.78 - 3.90$, $3.96 - 4.08$, $6.00 - 6.12$, $6.48 - 6.60$, $9.72 - 9.84$, $9.84 - 9.96$, $9.96 - 10.08$ keV we combine adjacent 60 eV bins to produce single 120 eV bins. Similarly, we combine bins in $5.49 - 5.64$ keV in a single 150 eV bin.

9. For additional increase of negative residuals, we use slightly (0.5 %) smaller normalization of powerlaw continuum. The powerlaw index remains the same. Such renormalization allows us to obtain more conservative constraints for normalization of the narrow line candidates.

---

[17]This is done because our goal is not construct the best fit model of the underlying dataset, but to optimize the model that would not "hide" weak residual lines.
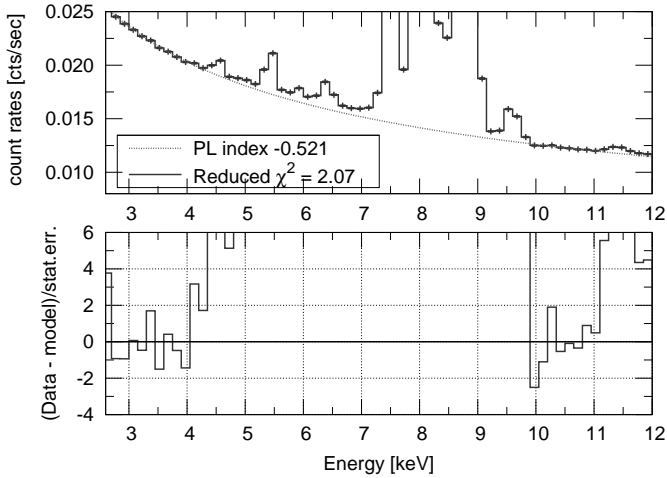
Figure 5.15: Conservative continuum powerlaw model for PN spectrum binned by 150 eV obtained by fitting at 2.70–4.35 and 10.05–11.1 keV energy ranges which are free from lines. Significant positive residuals are clearly visible in the positions of the instrumental lines.

The obtained best-fit reference model is shown in Fig. 5.21. It is reasonable as the number of free parameters (16) is much smaller than the number (92) of the energy bins.

5.3.4 Constructing a spectral models for MOS combined datasets

Best-fit reference models for MOS1 and MOS2 cameras are built in the same way as for PN camera, see Sec. 5.3.2. The major difference is that we cannot adequately fit the continuum with a single `powerlaw` and thus produced a combination of two `powerlaw` models with different indices and normalizations at $\lesssim 5$ keV and $\gtrsim 6$ keV energies. The transition between these two powerlaw models is modeled with a step function at ~ 5.4 keV. Due to relative weakness of MOS instrumental lines (compared to PN camera) we model all instrumental lines with the help of pure `gaussian` model.

The resulting fit is shown in Fig. 5.22.

Chapter 5. Analysis of combined dataset
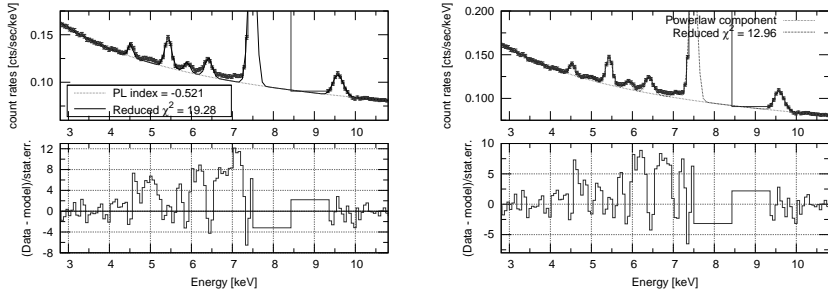
(a) Adding several gaussians to power-law model from Fig. 5.15 corresponding to *bright instrumental lines*. Their positions are fixed according to Table 5.6, but dispersion and normalizations are determined via χ^2 fitting procedure.

(b) The same as in Fig. 5.16a, but with two extra gaussian at 5.0 and 7.075 keV corresponding to *line candidates*. The fit quality is now significantly better though there are still some residuals at 6.7-7.0 keV.

Figure 5.16: Accounting for the line-like residuals in the model of the combined PN spectrum. In Fig. 5.16a, we add to the `powerlaw` model (shown as pink dotted line) several `gaussians` in the positions of well-established *instrumental lines* (Table 5.6). Energy range 7.56-9.30 keV around three most prominent instrumental lines (8.045, 8.613 and 8.895 keV) is not used in this modeling. Significant decrease of line residuals compared to previous Fig. 5.15 is shown. In Fig. 5.16b, we add two extra gaussians corresponding to *line candidates* at 5.0 and 7.075 keV. In both figures, 3σ error bars are shown for convenience.

5.3.5 Estimating systematic errors

According to Figs. 5.21 and 5.22, the fit quality is statistically unacceptable. The fact that reduced χ^2 is significantly larger than 1 means that the average residuals are systematically larger compared to statistically acceptable fit. For such a fit, we expect 68% of all residuals have absolute values smaller than 1σ, 95% – smaller than 2σ. In reality, for PN camera 68% of all residuals have absolute values larger than 0.81 statistical errors, 95% of residuals – larger than 2.20 statistical errors, so the average residual value is estimated as $(0.81 + 2.20/2)/2 = 0.96$ (in units of statistical errors). Because the fit of PN data have used 90 energy bins, and the model has 18 free parameters, the expected average value of residual is only $1 - 18/90 = 0.80$ (in units of statistical errors). To increase the average residual from 0.80 to 0.96 statistical error, we need to add some systematical error in quadratures. The necessary value of systematic error should be $\sqrt{0.96^2 - 0.80^2} = 0.53$ (in units
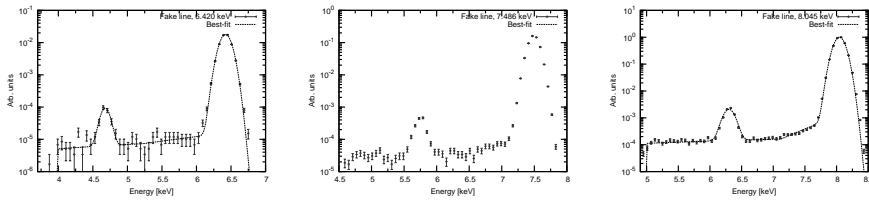
(a) Shape of strong instrumental line at 6.420 keV.

(b) Shape of strong instrumental line at 7.456 keV.

(c) Shape of strong instrumental line at 8.045 keV.

Figure 5.17: Determining (non-Gaussian) shapes of strong instrumental lines for the PN camera. Using `fakeit` procedure from `Xspec` and actual response matrices of the EPIC PN camera, we modeled long exposure observation of instrumental lines at positions 6.420, 7.456 and 8.045 keV. Line normalizations are shown in arbitrary units (*the units are same across all panels*, i.e. the leftmost line is the weakest and the rightmost line is the strongest). Clearly seen are second Gaussian peaks and low-energy continuum tails. Error bars are statistical, green solid lines are best fit models (using Eq. (5.2)). Each line is described by 10 parameters (instead of 3 in the Gaussian case).
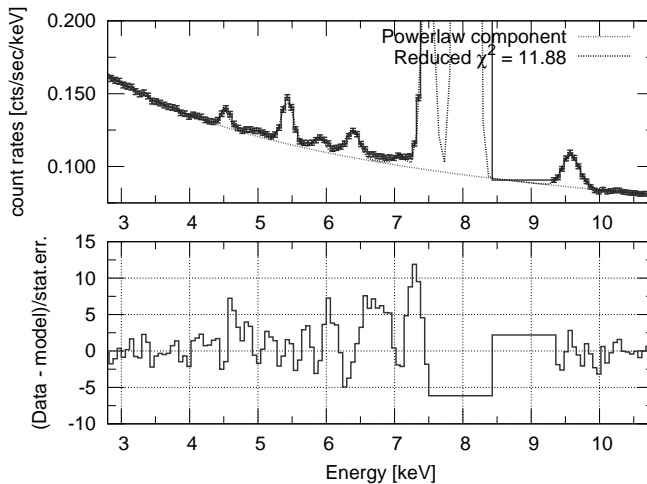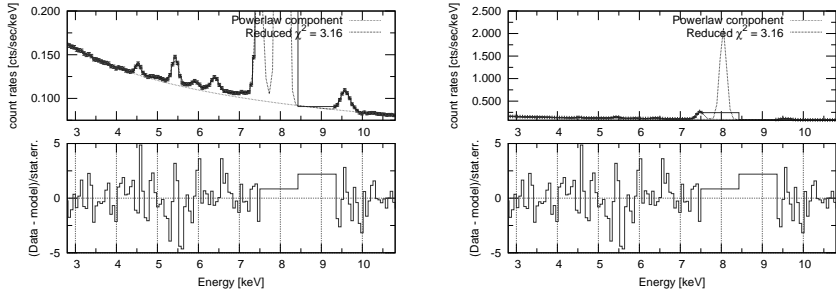

Figure 5.18: The same as in Fig. 5.16b but with modification of three instrumental lines at 6.420, 7.456 and 8.045 keV according to their modeling in Fig. 5.17. In this figure, 3σ error bars are shown for convenience.

of statistical errors), or (by assuming mean statistical error for PN camera equal to 0.48%), $0.53 \times 0.48 = 0.25\%$ (in absolute value). Similar calculations

(a) The same as in Fig. 5.18 but now the relative contribution of primary gaussian, continuum and secondary gaussian is not fixed and determined from the least-squares method.

(b) The same as is Fig. 5.19a but scaled for better visualization of high-energy line.

Figure 5.19: PN spectra modeled with fake gaussians at 6.420, 7.456 and 8.045 keV. Compared to Fig. 5.18, now the relative contribution of primary gaussian, continuum and secondary gaussian is not fixed and determined from the least-squares method. The resulting fit quality is much better than for our previous attempt, see Fig. 5.18 for details. In both figures, 3σ error bars are shown for convenience.
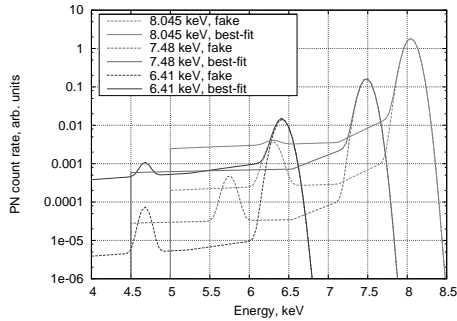

Figure 5.20: Comparison of the best-fit fake Gaussian models (solid) used in previous Fig. 5.19 with initial fake Gaussian models from Fig. 5.17 (dashed), see Eq. (5.2).

of absolute value for systematic errors for MOS1 and MOS2 camera give 0.19% and 0.41%, respectively.
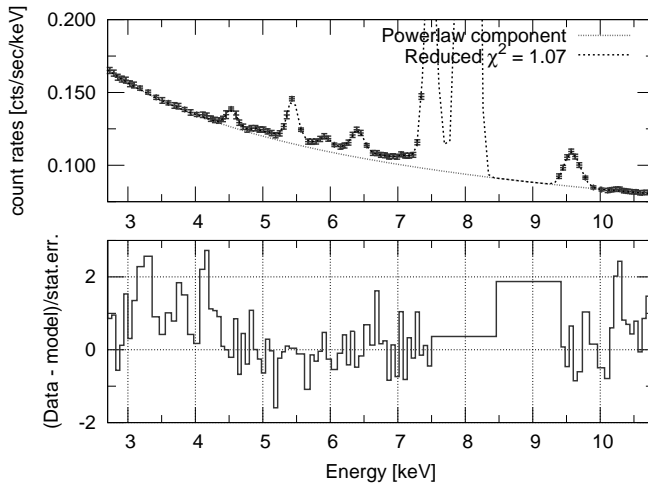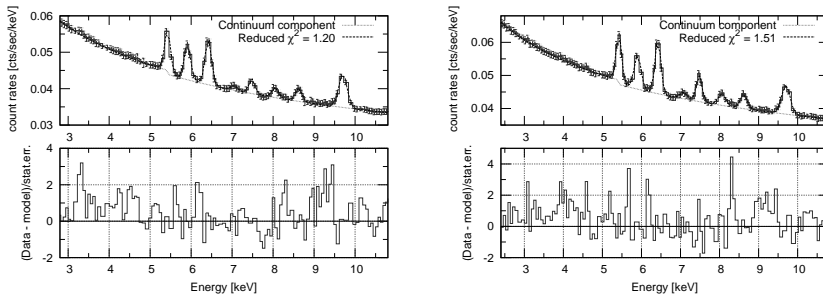
Figure 5.21: Resulting fit of PN combined dataset (see text). Most of the bins have 60 eV width, some of bins have been rebinned by 30, 120 and 150 eV in order to decrease the narrow negative residuals. To further reduce the negative residuals, we decreased the normalization of the powerlaw continuum by 0.5%. *For better error visualisation, 3σ error bars are shown.*

(a) Modeling total (2.8-10.8 keV) spectra for continuum model (consisting of two power-laws connected with a step function) plus several gaussian lines. Similar to modeling of PN spectrum shown in Fig. 5.21, we decrease the normalization of MOS continuum by 0.5%. For better error visualisation, 3σ error bars are shown.

(b) The same as in the left part but for MOS2 camera.

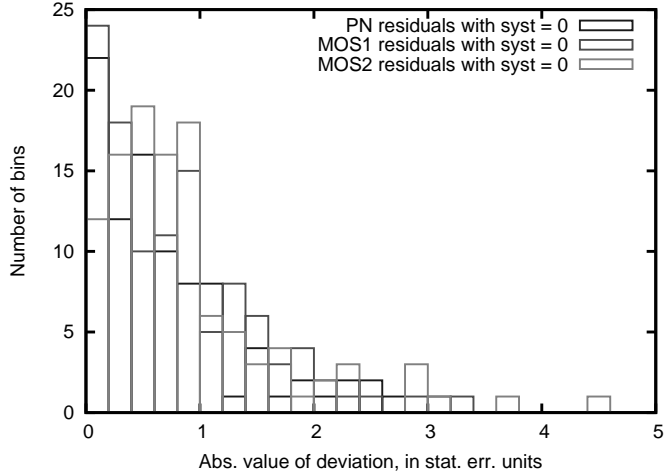Figure 5.22: Modeling of MOS1 and MOS2 count rates at 2.8-10.8 keV.

Figure 5.23: Distribution of residuals for MOS (Fig. 5.22, upper panels) and PN (Fig. 5.21, upper panel) cameras in the final dataset. The distribution is slightly non-Gaussian, especially due to presence of several large residuals. By adding a systematic error (0.19% for MOS1, 0.41% for MOS2 and 0.21% for PN camera) in quadratures we increase total error so the distribution (in units of total errors) becomes close to Gaussian, see Sec. 5.3.5 for calculation details.

5.4   Detection of faint lines

To search for faint narrow lines, we use the reference models (described in details in Sec. 5.3.2 and 5.3.4) shown in Figs 5.21 and 5.22. The extra Gaussian line with fixed position and small dispersion is added to our reference model in some particular energy bin. We specify the line's dispersion as fixed function of energy, defined by the central values (see the left panel Fig. 5.24, see Section 5.4.1.1 for details). To account for possible negative residuals, we allow the normalization of the extra line to be negative. Then, by using least-squares fitting procedure, we define the best-fit value of the normalization of the extra line (allowing all other model parameters, except position and dispersion of the extra line to vary). By changing line position in 10 eV increments (much smaller than the energy resolution of the instrument) this procedure is repeated for the energy ranges of our interest (2.8-10.8 keV).

5.4.1 Verification of line detection procedure.

Due the presence of various sources of systematic error, it is crucial to perform extensive tests checking validity of our procedure of line detection. Namely, by adding faint narrow line with certain intensity our procedure of line detection should detect this line at a given position and intensity (within the confidence ranges).

5.4.1.1 Simulations of narrow lines.

We simulate a narrow `gaussian` line (with $\sigma_E = 0.001$ keV) for each observation combining it with appropriate RMF and ARF constructed with `rmfgen` and `arfgen`, respectively. We use the same value of initial line normalization for each camera. The simulations were performed with the `fakeit` command, a part of `Xspec` spectral fitting package [409]. Then, the simulated spectra were combined together for each camera (MOS1, MOS2, PN) and modeled with the help of `gaussian` model having 2 free parameters: energy dispersion σ and fraction F of counts contributing to `gaussian`,

$$f(E) = \frac{F \times N_{counts}}{\sqrt{2\pi\sigma^2}} \exp\left(-\frac{(E - E_0)^2}{2\sigma^2}\right).\qquad(5.3)$$

The central energy E_0 was kept fixed to the initial central energy of the line.

The results are shown in Fig. 5.24. As we expect, $F \lesssim 1$. The obtained values of σ correspond to $\Delta E \simeq 100 - 200$ eV, consistent with values known from literature[18], see e.g. Figs 25-26 of [320].

To calculate intensity of the recovered line, one should divide the obtained countrate (in cts/s) by the effective area of the corresponding instrument. To calculate the effective area, we used the following procedure. For each observation, we used the actual effective area (binned by 5 eV bins) produced by `arfgen` procedure. Then, for each energy bin we calculate the exposure and FoV-weighted mean for each observation. Finally, to account the finite energy resolution of the cameras (with FWHM = 100-200 eV depending on energy, see e.g. left Fig. 5.24 for details), we rebin the obtained effective area by 150 eV bins. The results are shown in Fig. 5.12.

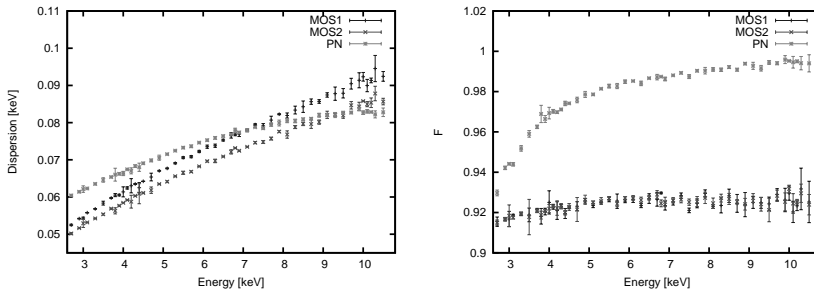[18]Note that $\Delta E \equiv 2\sigma\sqrt{2\log(2)} \simeq 2.35\sigma$, according to definition of FWHM.

Figure 5.24: *Left*: Dispersion σ_E of a narrow line with energy E (note that FWHM for a Gaussian line is $2.35 \times \sigma_E$). The internal dispersion of the line is 1 eV. *Right*: Fraction F of a photons contributing to narrow gaussian with dispersion σ_E (see left Figure).

5.5 Results

5.5.1 Identifying lines

The procedure, described in Section 5.4 led to identification of a number of line-like residuals in our datasets.

The properties of instrumental lines identified with our procedure are shown in Table 5.7.

5.5.2 Upper limits on the flux in narrow line

The 3σ upper bounds on intensities of extra narrow lines (per unit solid angle) are presented in Fig. 5.26. To obtain these bounds, we used "statistical" method described e.g. in [46]. Namely, we add a narrow line at fixed energy to combined dataset. The value of line dispersion is fixed equal to its expectation, see Fig. 5.24 for details. Then, we calculate the intensity which increases total χ^2 by 3^2 (which corresponds to 3σ bound). To calculate the values of χ^2 we add systematical errors obtained in Sec. 5.3.5. The "gaps" on the upper bounds are due to strong instrumental lines. To account possible uncertainties on line determination, see Fig. 5.25 for details, we weaken our bounds by multiplying the limiting intensities by 1.05 and 1.3 for energies below and above 5.3 keV, respectively. For comparison, we show corresponding bounds obtained from central part of Andromeda galaxy, see Fig. 8 of [230] for details. From Eq. 4.1 we expect the increase of sensitivity
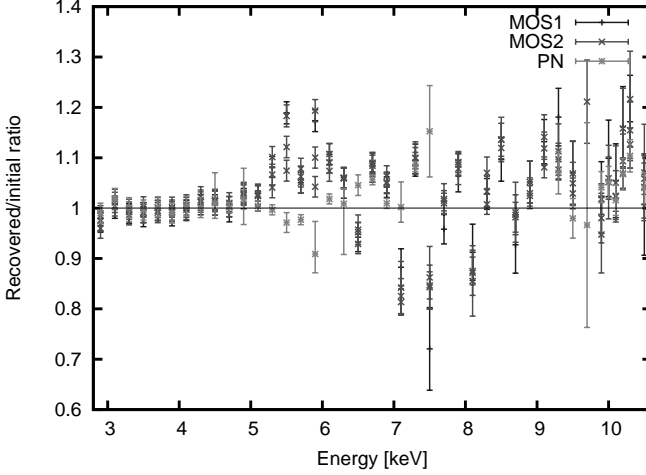
Figure 5.25: Ratios between intensities of initial and recovered lines, together with 1σ errors. Below ~ 5.3 keV, the ratio deviates from 1 within 5%, above ~ 5.3 keV – within 30%. As a result, in Fig. 5.26 we weaken our bounds by multiplying the limiting intensities by additional factors 1.05 and 1.3, respectively.

equal to ratios of $\sqrt{t_{exp} \times \Omega_{\text{fov}}}$, or $\sim$8.7, $\sim$8.7 and $\sim$6.3 for MOS1, MOS2 and PN cameras, respectively. Indeed, as we see from Fig. 5.26, such an improvement is close to observed one at $\lesssim 5$ keV. At larger energies, the improvement is significantly smaller, due to contribution from strong instrumental lines.

To check the validity of our bounds presented in Fig. 5.26, we use the following procedure. After adding a simulated narrow line with fixed intensity to our combined dataset, see Sec. 5.4.1 for details, we try to detect the simulated line in a obtained spectrum. The results for PN camera are shown in Fig. 5.27. The lines detected at $\geq 3\sigma$ level and not detected are marked by the crosses and multiplication signs, respectively. As we expected, all crosses are located below the bounds. This means that are procedure does not produce any "spurious" line candidates, and the obtained bounds are very conservative.

Finally, we produce new bounds on sterile neutrino dark matter parameters – mass of dark matter particle M_{DM} and mixing angle $\sin^2(2\theta)$. To do that, we first calculate the expected dark matter signal. Milky Way contribution is estimated using the conservative dark matter profile from [372], see Table 5.1 and Fig. 5.1 for details. This gives the exposure-weighted mean

MOS1 (keV/ cts/sec/cm^2/ is known?)	MOS2 (keV/ cts/sec/cm^2/ is known?)	PN (keV/ cts/sec/cm^2/ is known?)	Possible line (keV)
—/—/—	—/—/—	$4.532/5.2 \times 10^{-6}$/+	4.511 (Ti Kα)
—/—/—	—/—/—	$4.917/1.4 \times 10^{-6}$/+	4.952 (V Kα)
$5.428/1.6 \times 10^{-5}$/+	$5.426/1.7 \times 10^{-5}$/+	$5.439/1.3 \times 10^{-5}$/+	5.415 (Cr Kα)
$5.910/1.8 \times 10^{-5}$/+	$5.901/1.8 \times 10^{-5}$/+	$5.927/2.7 \times 10^{-6}$/+	5.899 (Mn Kα)
$6.419/2.8 \times 10^{-5}$/+	$6.422/3.1 \times 10^{-5}$/+	$6.420/9.2 \times 10^{-6}$/+	6.404 (Fe Kα)
$7.052/4.2 \times 10^{-6}$/+	$7.079/7.1 \times 10^{-6}$/+	$7.091/9.0 \times 10^{-7}$/−	7.058 (Fe Kβ)
$7.484/1.6 \times 10^{-5}$/+	$7.477/2.7 \times 10^{-5}$/+	$7.486/1.5 \times 10^{-4}$/+	7.478 (Ni Kα)
$8.054/1.9 \times 10^{-5}$/+	$8.066/2.5 \times 10^{-5}$/+	$8.045/2.1 \times 10^{-3}$/+	8.048 (Cu Kα)
$8.623/3.7 \times 10^{-5}$/+	$8.619/4.1 \times 10^{-5}$/+	$8.626/2.2 \times 10^{-4}$/+	8.639 (Zn Kα)
—/—/—	—/—/—	$8.904/2.8 \times 10^{-4}$/+	8.905 (Cu Kβ)
—/—/—	—/—/—	$9.553/5.2 \times 10^{-5}$/+	9.572 (Zn Kβ)
$9.703/2.5 \times 10^{-4}$/+	$9.701/2.1 \times 10^{-4}$/+	$9.698/2.0 \times 10^{-5}$/+	9.713 (Au Lα)

Table 5.7: Parameters of instrumental lines for the EPIC MOS and PN cameras identified with our procedure (first 3 columns). Each column shows: **(i)** *energy of detected line* [keV] / **(ii)** *intensity of detected line* [cts/sec/cm^2] / **(iii)** whether the line has been previously known as an instrumental one (sign "+" or "–") for the corresponding camera. For PN line at ~ 4.95 keV, the corresponding V Kα instrumental line has been observed in the mode with significantly enhanced intensity of instrumental lines (the *CalClosed* mode), see [389] for details. The initial energies of fluorescence lines are taken from Table V of [408], similar to previous Table 5.6. We do not put here K Kα and Ca Kα lines because they are not detected in our datasets. All line positions are reconstructed with precision ≤ 40 eV, much better that the energy resolution of EPIC cameras.

column density 130 M$_\odot$/pc^2. We also added exposure-weighted contribution from Andromeda galaxy using the most conservative profile of [11], see Fig. 5.2. Because M31 exposure is only $\sim 1/5$ of total, the corresponding column density contribution from M31 is about 20 M$_\odot$/pc^2. To be conservative, we did not add contribution from other galaxies. This gives us the total exposure-weighted mean column density for our combined dataset equal to 150 M$_\odot$/pc^2.

The resulting bounds on sterile neutrino parameters obtained from combination of all 3 cameras are shown in Fig. 5.28. We strenghen previous
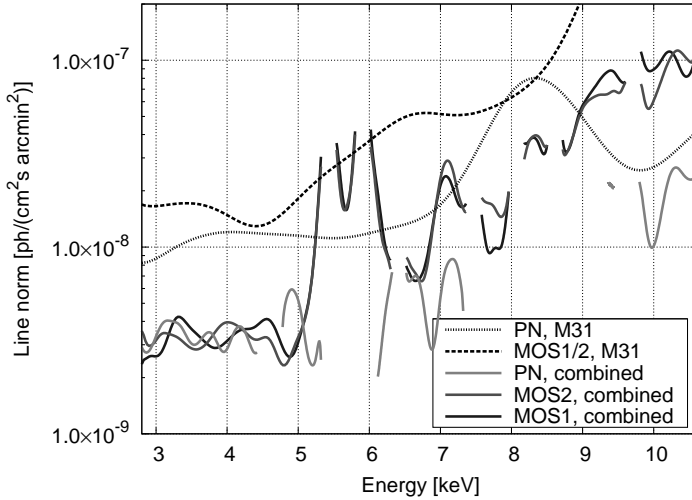
Figure 5.26: 3σ upper bounds on intensities (per unit solid angle) of a narrow line (grey solid lines). The parameter space *above* the lines is excluded. The errorbars are discussed in Sec. 5.3.5. To account possible uncertainties on line determination, see Fig. 5.25 for details, we weaken our bounds by multiplying the limiting intensities by 1.05 and 1.3 for energies below and above 5.3 keV, respectively. For comparison, we show smoothed bounds for MOS1/MOS2 and PN cameras from Fig. 8 of [230]. Due to larger statistics of our dataset, we expect the improvement of our bounds with respect to M31 by about 8.7 (for MOS cameras) and about 6.3 for PN camera. The gaps are at the positions of strong instrumental lines, where the sensitivity of our method is low.

X-ray bounds (shaded region in the upper right corner on Fig. 5.28) above ~ 5.5 keV (excluding several energy ranges dominated by instrumental lines) up to a factor 5-6. This is possible due to large (for a factor of ~ 50) increase of exposure for our combined dataset, and the specially method of data analysis allowing to control systematic errors at the sub-% level (i.e. close to statistical errors).
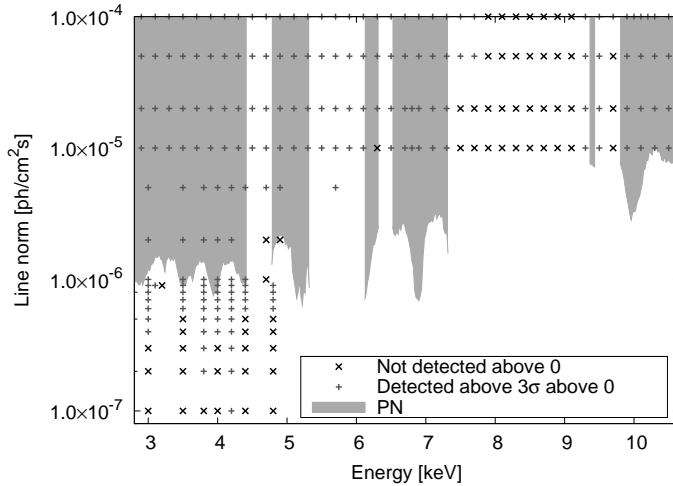
Figure 5.27: Verification of the sensitivity of our method. To check the reliability of the bounds of Fig. 5.26, we add to the PN combined dataset simulated lines with central energies and normalizations and check whether these lines are detected at $\geq 3\sigma$ level. During the simulations, the statistical fluctuations of number of counts are taken into account. Those lines that are detected at $\geq 3\sigma$ level are marked by the crosses, those are not – by multiplication signs. The correct bounds should have crosses inside the shaded area and, more importantly, multiplication signs outside the shaded region. This is what one indeed sees in this Figure. The fact that in most cases crosses continue to be detected below the shaded area means that our bounds are very conservative.

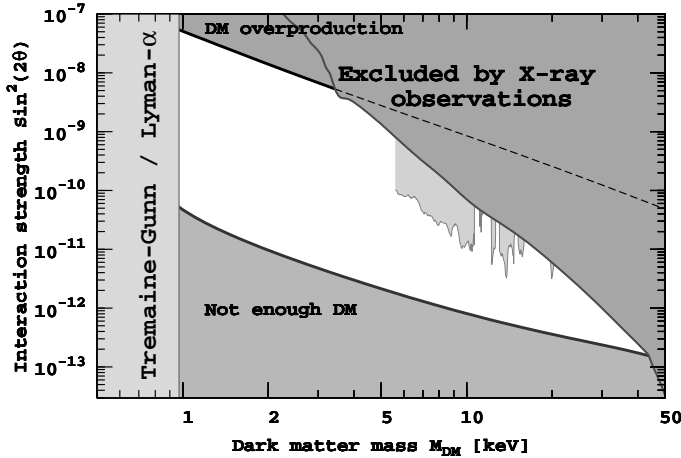Figure 5.28: The allowed region of parameters of sterile neutrino dark matter in the νMSM (white unshaded region) confronted with existing and projected experimental bounds. For any combination of mass and mixing angle between two black curves the necessary amount of dark matter can be produced (given the presence of certain amount of lepton asymmetry in the plasma, generated by two other sterile neutrinos). The shaded region in the upper right corner is excluded by the non-observation of decaying dark matter line in X-rays [221, 223–225, 228, 230, 231, 318, 357, 358]. Grey regions between $\sim 5\,\text{keV}$ and $\sim 20\,\text{keV}$ are excluded from analysis of combined dataset described in this thesis (Chapter 5). The gaps are due to the presence of strong instrumental lines at certain energies (where the combination method does not provide any improvement over earlier bounds). The lower limit of $\sim 5\,\text{keV}$ is due to the presence of instrumental lines and absorption edge at energies $1-2.5\,\text{keV}$ and emission of the Milky Way, dominating at lower energies. In the region below $1\,\text{keV}$ sterile neutrino dark matter is 'too light' and is ruled out based on 'Tremaine-Gunn' like arguments [46] and on the Lyman-α analysis [99, 131].

Chapter 6

Future prospects

Really significant progress (that allows, for example, to cover the whole region of parameter space in Fig. 5.28) in searching for decaying dark matter cannot be achieved with the existing instruments by simply increasing the exposure of observations. Indeed, the width of the dark matter decay line, $\Delta E/E_\gamma$ is determined by the virial velocities of dark matter particles in halos and ranges from $\mathcal{O}(10^{-4})$ for dwarf spheroidal galaxies to $\mathcal{O}(10^{-3})$ for the Milky Way-size galaxies to 10^{-2} for galaxy clusters. If the spectral resolution is much bigger than the width of the line, one averages the photons from the line with the background photons over a large energy bin. This is the case for all existing X-ray missions, whose detectors are based on CCD technology (c.f. [410]) and where the spectral resolution is at the level $\Delta E/E \gtrsim 10^{-2}$, see Fig. 6.1. Therefore, *an X-ray spectrometer with the energy resolution at least $\Delta E/E \sim 10^{-3}$ is crucial for detection of a decaying dark matter line.*

The technology behind such spectrometers (known as *X-ray micro-calorimeters*, see e.g. [411, 412]) has been actively developed by the high-energy astrophysical community in the last decades. There is a strong interest for building such a spectrometer, and different versions of high resolution X-ray missions had been proposed in response to the ESA and NASA calls (including the ESA's call for Fundamental Physics Roadmap), see e.g. [75, 365, 413–415]. Astrophysical interest to X-ray spectrometer is motivated by a number of important applications to observational cosmology, providing crucial insight into the nature of dark matter by studying the structure of the "cosmic web". In particular, (i) search for *missing baryons* in the cosmic filaments;
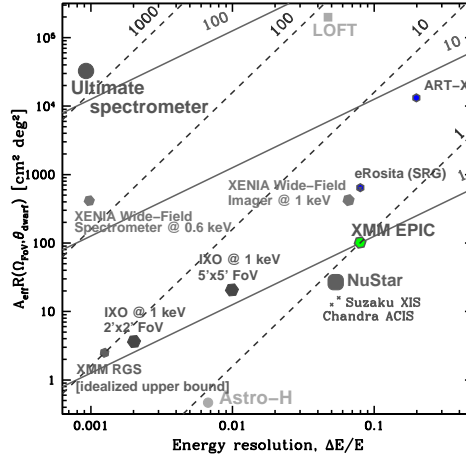
Figure 6.1: Comparison of sensitivities of existing and proposed/planned X-ray missions for the detection of the dark matter decay line in a nearby dwarf spheroidal galaxy of the angular size of $1°$. The sensitivity of XMM-Newton EPIC camera is taken as a reference. Solid lines indicate improvement of the sensitivity by factors of 1, 10 and 100 (the top left is the most sensitive). The dashed lines show the improvement of the sensitivity towards the detection of a strong line (in an effectively background free regime). See also [75, 229]

through their emission and absorption ; (ii) trace the evolution and physics of clusters out to their formation epoch; (iii) use gamma-ray bursts as back-light to observe the warm-hot intergalactic media in absorption; (iv) study the evolution of massive star formation using Gamma Ray Bursts to trace their explosions back to the early epochs of the Universe ($z \sim 6$) (see e.g. [365, 414, 415]).

The first spectrometer based on this technology was flown (albeit unsuccessfully) on *Suzaku* mission [416] and another one is being planned for the Astro-H [413, 417] (to be launched in 2014). However, currently planned and proposed X-ray micro-calorimeter missions (Astro-H [413], Athena [415], ORIGIN [414], etc.) are not optimal for the purpose of decaying dark matter search. These missions are optimized for the astrophysical goals and have limited field-of-view (usually, much below $1 \deg^2$), good angular resolution and narrow energy range.

On the contrary, the *key parameters* that determine the sensitivity of the proposed instrument for decaying dark matter search are (see Fig. 6.1):

- a spectral resolution $\Delta E/E \lesssim 10^{-3}$ over the range of energies $0.5 - 25 \, \mathrm{keV}$ (this is the minimal energy range, that would allow to probe the parameter space of our baseline model, the νMSM);
- large '*grasp*' $\sim 10^3 - 10^4 \, \mathrm{cm}^2 \times \mathrm{deg}^2$. There are essentially two possibilities to achieve such a grasp. One can either launch a non-imaging spectrometer (with a 'collimator' having a field-of-view as large as $\sim 10^2 \, \mathrm{deg}^2$)[1]; or install mirrors (thus increasing the effective area beyond the geometric size of the detectors, probably to as much as $10^3 \, \mathrm{cm}^2$). The latter option allows to have also imaging capabilities, however, it is usually extremely costly to cover the required energy range and to have sufficiently large (at least $1° \times 1°$) field of view.

Fig. 6.1 summarizes sensitivity of existing and proposed missions and demonstrates that none of them would provide a sufficient improvement with respect to the existing constraints (see [75, 229] for discussion).

Currently, there exists a project (the *X-ray quantum calorimeter*, XQC [418]) that can be considered a prototype of the proposed mission. It has the field of view of about $1 \, \mathrm{sr}$ ($3.5 \times 10^3 \, \mathrm{deg}^2$), an effective area of $\sim 1 \, \mathrm{cm}^2$ and the energy resolution of $10 \, \mathrm{eV}$ over the energy range $0.1 - 4 \, \mathrm{keV}$ [418].[2] This calorimeter has been flown several times on sounding rockets [418]. Although each flight had been very short (about 100 seconds), it allowed to demonstrate that the Milky Way emission in the energy range $0.1 - 1 \, \mathrm{keV}$ (which looks as a continuum in the spectra obtained with X-ray imaging instruments, see e.g. [327, 419] is actually a "forest" of thin lines (see Fig. 6.2). Because of its superior spectral resolution, decaying dark matter bounds based on the $\sim 100 \, \mathrm{sec}$ exposure of the flight of this spectrometer [418] are comparable with $10^4 \, \mathrm{sec}$ of the *XMM-Newton* exposure [229].

To detect a dark matter decay line, that is much weaker than the lines resolved with the XQC spectrometer, a significantly longer exposure ($\sim 1 \, \mathrm{year}$)

---

[1]Making field-of-view significantly large than about $10° \times 10°$ would of course further increase the sensitivity towards the line detection. However, in this case it would become challenging to identify the nature of the candidate line (if found), as in this case none of the nearby dark matter dominated objects with large angular size (Andromeda galaxy, Large and Small Magellanic clouds, Virgo cluster) will look like 'hot spots' of dark matter decays. Moreover, in this case it will not be possible to build a dark matter surface brightness profile as one varies the directions off the Galactic Center and investigate whether it is consistent with dark matter distribution in the Milky Way.

[2]A similar calorimeter used in Suzaku was capable of delivering a similar resolution up to the maximal energy range of $12 \, \mathrm{keV}$ [416].
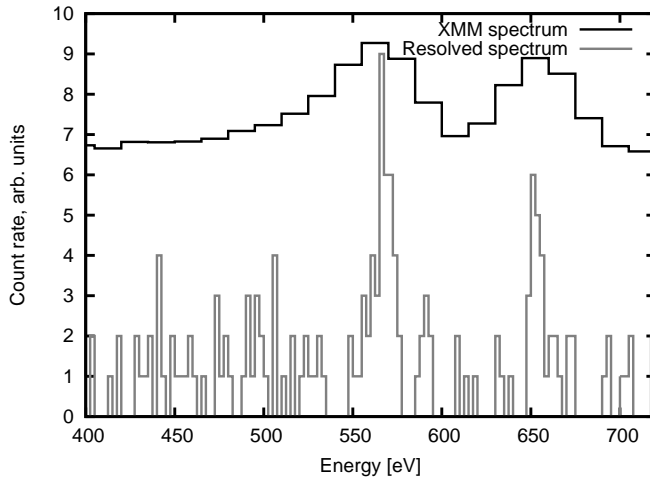
Figure 6.2: Galactic diffuse background (observed with *XMM-Newton* (black) and the same data, observed with the X-ray spectrometer (XQC project [418]).

would be required. The requirement to keep the cryostat of such a spectro-meter in the stable regime, means that one cannot use the sounding rockets, but rather needs to use a satellite (probably, staying in Low Earth Orbit, unlike *XMM-Newton* or *Chandra*). The project therefore becomes a small-to-medium scale cosmic mission.

Chapter 7

Conclusions

In this thesis, we *undertook a systematic model-independent program of studying the properties of decaying dark matter*. We do not limit ourselves by any particular model, and are agnostic about the mass and the interaction type/interaction strengths of dark matter. We concentrate on limiting possible lifetime and decay rate of dark matter particles, as a function of the mass, by performing searches for the signatures of decays of dark matter particles.

We have revised the existing theoretical approaches and developed a new method that allows to derive strong yet robust bounds on the mass of dark matter particles. By analyzing the experimental data for the objects with the largest dark matter phase-space density – dwarf spheroidal galaxies – it was shown that the mass of dark matter fermion should exceed ∼0.4 keV, and therefore *the X-ray energy range is a preferred region when searching for radiatively decaying dark matter*.

By analyzing dark matter distribution in different types of galaxies and in galaxy clusters it was shown that the expected dark matter decay signal increases slowly with the mass of the object. We demonstrate that the average central dark matter column density, defining the expected signal, follows, as a function of total halo mass a universal scaling law. This result allowed us to select dwarf and spiral galaxies as the observational targets with the optimal signal-to-noise ratio.

When taking into account the existing bounds on dark matter decay lifetime our results imply that it would be very challenging to obtain robust improvements on the existing constraints (even by as little as a factor of

2) by individual observations of dark matter dominated objects. Therefore *to further improve the existing bounds and probe the theoretically interesting regions of particle physics models we performed a combined analysis of a very large dataset of archival XMM-Newton observations* of galaxies. Extremely large combined exposure of this dataset (two orders of magnitude longer than a typical single observation) requires a very good control of systematic errors and of the instrumental backgrounds and does not allow to use the standard tools of data analysis. To tackle these problems, we developed a novel method of data reduction, constructing the largest to-date dataset of *XMM-Newton* observations.

Our method had revealed several new narrow line candidates. After careful analysis, all these candidates were quantified as faint instrumental lines that have not been observed previously. No "suspicious" lines at more than 2σ level had been detected.

Non-observation of candidate lines allowed us to improve the existing bounds by more than a factor of 8 at some energies. (Formally, such an improvement would require increase of exposure of an individual observation from $\sim 100\,\mathrm{ksec}$ to $\sim 6.5\,\mathrm{Msec}$ – half of the annual observation programme of *XMM-Newton*). Our results are summarized in Fig. 5.26, page 116.

To understand the significance of our results, we converted the upper bound on the flux in line into the bounds on the interaction strength of sterile neutrino dark matter in our baseline model. We were able to advance into the cosmologically interesting region of parameter space for masses between 5 and 20 keV (see Fig. 5.28, page 118). The significant part of the parameter space, nevertheless, remains unexplored. We were not able to probe cosmologically interesting region at masses below ~ 4 keV (upper gray region in Fig. 5.28) and did not probe the parameter range above ~ 22 keV (while the allowed mass range goes all the way to 50 keV).

At first sight it may seem that the searches for decaying dark matter using existing X-ray missions (*XMM-Newton*, *Chandra*, *Suzaku*) had reached their limit. Indeed, significant (factor of few) increase of exposure beyond that of our combined dataset (6–9 Msec) seems unrealistic. This is however, not true and *below we discuss the further possible directions to improve our results*.

First of all, as Fig. 5.27 demonstrates, our bounds are overly conservative at some energies, especially between 3 and 5 keV, where crosses extend

down below the pink shaded region. The reason for this has not been understood yet and we expect that eventually we will be able to improve our upper bounds by a factor of few at these energies.

Secondly, when converting upper limits on the line flux into the interaction strength of dark matter models, we have conservatively included only the signals from the Milky Way halo and the halo of Andromeda galaxy for appropriate observations. The total dark matter content in our field of view is much higher (as all observations contain at least one nearby galaxy in its field of view). Proper estimates of dark matter contributions of about 100 galaxies, used in this dataset, should further increase our bounds on the interaction strength of sterile neutrino dark matter in the whole range of probed masses.

Thirdly, the gaps (in positions of strong instrumental lines) can be filled (at least partially) by doing similar analysis with the different instrument. As Table 7.1 demonstrates the positions of strong instrumental lines differ between different instruments and therefore similar analysis with *Chandra* or *Suzaku* could help to increase the sensitivity. Notice, however, that among all these missions the grasp (product of the effective area and of the field of view, controlling the total statistics for diffuse sources) of *XMM-Newton* is *at least factor of 5 larger*, than for *Chandra* and/or *Suzaku* and therefore the loss of statistics should be compensated by a longer exposure. Reaching the sensitivity, comparable to our results with e.g. *Suzaku* observations would require about 5 times bigger collection of observations of dark matter-dominated objects (i.e. at least 30 Msec of cleaned exposure). While total archival of observations with *Suzaku* is about 85 Msec, we found only 10 Msec of observations of galaxies from our dataset, (as described in the Section 5.1). On the other hand, the instrumental background of *Suzaku* is significantly lower, than that of *XMM-Newton* (as *Suzaku* is flying on a low earth orbit).

An improvement of bounds for masses lower 5 keV is extremely challenging. First of all, at energies $2.3 - 2.5$ keV the mirrors of all X-ray satellites have an absorption edge, and the effective area is highly uncertain. Next, all instruments possess several strong instrumental lines at energies ~ 1.5 keV (see Table 7.1). Finally, at even lower energies emission of the Milky Way is the dominant signal, which may allow to reach a similar sensitivity with a somewhat lower exposure.

Finally, we discussed an ultimate way to probe the whole parameter

Energy (keV)	*XMM-Newton* EPIC	*Chandra* ACIS	*Suzaku* XIS
1.486 (Al Kα)	+	+	+
1.740 (Si Kα)	+	+	+
2.123 (Au Mα)	–	+	+
4.511 (Ti Kα)	+		–
5.415 (Cr Kα)	+	–	–
5.895 (Mn Kα)	+	–	+
6.404 (Fe Kα)	+	–	–
6.490 (Mn Kβ)	–	–	+
7.470 (Ni Kα)	+	+	+
8.048 (Cu Kα)	+	–	–
8.265 (Ni Kβ)	–	–	+
8.639 (Zn Kα)	+	–	–
8.905 (Cu Kβ)	+	–	–
9.572 (Zn Kβ)	+	–	–
9.671 (Au Lα)	+	+	+
11.51 (Au Lβ)	+	+	+

Table 7.1: Prominent instrumental lines for *XMM-Newton*/EPIC, *Chandra*/ACIS and *Suzaku*/XIS cameras. Shaded rows show energy intervals at which *Chandra* and/or *Suzaku* do not have strong instrumental lines, while *XMM-Newton* does. Notice, however, that the grasp of *Chandra* is inferior to that of *XMM-Newton* by the factors ranging from 10 at 1 keV, 20 at 5 keV and as large as 50 at 10 keV. The grasp of *Suzaku* is factor 5–6 worse than that of *XMM-Newton* over the whole energy range (meaning that the exposure should be increased by the same factor to arrive to the similar restrictions.

space of minimal models of decaying dark matter, including the region of soft, (~ 1 keV) X-rays. We argue that a new X-ray telescope with the energy resolution comparable to the intrinsic width of the dark matter decay line is needed for that. Such a mission would include an X-ray microcalorimeter with ~ 10 deg field-of-view and large grasp. Parameters of such a mission and possible observational programme is discussed.

Chapter 8

Appendixes

8.1   Abbreviations used in this thesis

Below, we collect the full list of abbreviations, used throughout this thesis.

ΛCDM — standard cosmological model

νMSM — Neutrino Minimal Standard Model

ACIS — Advanced Advanced CCD Imaging Spectrometer on-board *Chandra*

ARF — ancillary response function (effective area)

BBN — Big Bang Nucleosynthesis

BOSS — Baryon Oscillation Spectroscopic Survey, a part of SDSS-III

BURK — Burkert density distribution

CCD — charge coupled device

CDM — cold dark matter

Chandra — Chandra X-ray observatory

CMB — cosmic microwave background radiation

CWDM — cold plus warm dark matter

DM — dark matter

dSph — dwarf spheroidal galaxy

EPIC — European Photon Imaging Camera on-board *XMM-Newton*

FoV — field-of-view

FSH — free-streaming horizon

FWHM — full width at half-maximum

HDM — hot dark matter

HEASARC — High-Energy Astrophysics Science Archive Research Center

IS2 — modified pseudo-isothermal density distribution

ISO — pseudo-isothermal density distribution

KiDS — Kilo-Degree Survey

LHC — Large Hadron Collider

LMC — Large Magellanic Cloud

LSS — Large Scale Structure of the Universe

LSST — Large Synoptic Survey Telescope

M31 — Andromeda galaxy

MOS — Metal Oxide Semiconductor camera. Two EPIC cameras (MOS1 and MOS2) on board of *XMM-Newton*

MW — Milky Way galaxy

NFW — Navarro-Frenk-White density distribution

NRP — production of sterile neutrinos through non-resonant oscillations of active neutrinos

PN — p-n (positive-negative) transition. One of the EPIC cameras on board of *XMM-Newton*

RMF – redistribution matrix file (energy resolution)

RP — production of sterile neutrinos through resonant oscillations of active neutrinos

SDSS — Sloan Digital Sky Survey

SMC — Small Magellanic Cloud

TG — Tremaine-Gunn

VLT — Very Large Telescope of European Southern Observatory

WDM — warm dark matter

WFIRST — Wide-Field Infrared Survey Telescope

WIMP — weakly interacting massive particle

WMAP — Wilkinson Microwave Anisotropy Probe

XIS – X-ray Imaging Spectrometer on-board *Suzaku*

XMM-Newton SAS — *XMM-Newton* Science Analysis Software

XMM — *XMM-Newton*, X-ray Multi-Mirror X-ray mission

XRB – cosmic X-ray background

XSPEC — X-Ray Spectral Fitting Package

8.2   Appendixes for Chapter 2

8.2.1   Entropy for different distributions

In this Appendix we will calculate the entropy for several phase-space distributions, including those of (2.4), (2.20), (2.5), and explore its relation with the quantity Q, defined in (2.7).

The entropy of an ideal Fermi gas is given by the expression [420]

$$S = -\int d^3p d^3r f(r,p) \log\left(\frac{(2\pi\hbar)^3 f(r,p)}{g}\right) + \tag{8.1}$$
$$+ \left(\frac{g}{(2\pi\hbar)^3} - f(r,p)\right) \log\left(1 - \frac{(2\pi\hbar)^3 f(r,p)}{g}\right).$$

If the distribution function $f(r,p) \ll \frac{g}{(2\pi\hbar)^3}$, we obtain the expression for the entropy of a non-degenerate ideal gas:

$$S = -\int d^3p d^3r f(r,p) \left[\log\left(\frac{(2\pi\hbar)^3 f(r,p)}{g}\right) - 1\right]. \tag{8.2}$$

8.2.1.1   Ideal Boltzmann gas

We start with the case of ideal Boltzmann gas:

$$f(r,p) = f_0 e^{-\frac{p^2}{2mT}}. \tag{8.3}$$

Substituting it into Eq. (8.2), we arrive to the well-known expression (c.f. e.g. Sec. 42 of [420]):

$$\frac{S}{N} = \frac{5}{2} + \log\left(\frac{gV}{N}\frac{(mT)^{3/2}}{(2\pi\hbar^2)^{3/2}}\right), \tag{8.4}$$

where V is the volume of the system, N is a number of particles. Expressing S/N as a function of $\bar\rho$ and $\langle v^2\rangle$, we finally obtain relation between the entropy and Q in the form (2.10)

$$\frac{S}{N} = \log C_B - \log\frac{Q\hbar^3}{m^4},\ C_B = g\frac{e^{5/2}}{(6\pi)^{3/2}} \approx g \times 0.1489\ldots \tag{8.5}$$

8.2.1.2   Isothermal phase-space density distrubution

Next, we consider the case when the phase-space density distribution can be approximated by (pseudo)-isothermal sphere (c.f. (2.5)):

$$f_{iso}(r,p) = \frac{9\sigma^2}{4\pi G_N (2\pi m^2\sigma^2)^{3/2}(r^2 + r_c^2)} e^{-\frac{p^2}{2m^2\sigma^2}}. \tag{8.6}$$

The number of particles in such a system, as well as the total entropy, diverges for large r, however the entropy per particles grows logarithmically at large r and therefore the exact value of cut-off is not important.

Truncating the expression for the entropy at some r_{max} and taking $r_{max} \gg r_c$, we obtain

$$\frac{S}{N} = -\log \frac{Q\hbar^3}{m^4} + \log C_{iso}, \quad C_{iso} = \frac{g \exp(1/2)}{\sqrt{3}(2\pi)^{3/2}} \approx g \times 0.0604 \ldots \quad (8.7)$$

8.2.1.3 Non-resonantly produced sterile neutrinos

Next, we analyze the case of primordial momentum distribution, which has the form of (rescaled) relativistic Fermi-Dirac.

$$f(p) = \frac{g}{(2\pi\hbar)^3} \frac{F}{e^{\epsilon(p)/T} + 1}, \quad \epsilon(p) = p. \quad (8.8)$$

For now we keep both F and T to be arbitrary. The distribution in the form (8.8) accounts for both (2.4) and (2.20) cases. The entropy of N particles with distribution (8.8) is given by the expression (8.1), which reduces to

$$S = \frac{gVT^3}{2\pi^2\hbar^3} I(F), \quad (8.9)$$

where function $I(F)$ is given by

$$I(F) \equiv -\int_0^\infty dz z^2 \left[\frac{F}{e^z + 1} \log \left(\frac{F}{e^z + 1} \right) + \left(1 - \frac{F}{e^z + 1} \right) \log \left(1 - \frac{F}{e^z + 1} \right) \right]. \quad (8.10)$$

The integral (8.10) can be computed numerically. At $F \ll 1$ the expression (8.10) can be approximated by

$$I(F) \approx \frac{3}{2} \zeta(3) \left(F - F \log F \right) + F \int_0^\infty \frac{dz z^2}{e^z + 1} \log(e^z + 1). \quad (8.11)$$

The specific entropy S/N equals to

$$\frac{S}{N} = \frac{gm^4 I(F)}{2\pi^2\hbar^3} \left(\frac{\zeta(3)}{15\zeta(5)} \right)^{3/2} \frac{\langle v^2 \rangle^{3/2}}{\bar{\rho}} = \frac{g I(F)}{2\pi^2} \left(\frac{\zeta(3)}{15\zeta(5)} \right)^{3/2} \frac{m^4}{Q\hbar^3}. \quad (8.12)$$

Therefore, we see that for the distributions of the form (8.8) *relation between the entropy per particle and Q is not given by the simple expression* (2.10).

Up until this moment we kept parameters F and T in (8.8) independent. However, we are mostly interested in two particular cases: (i) $F = 1$ while

$T = T_{\mathrm{FD}}$ – arbitrary (distribution (2.4)); and (ii) $F < 1$ having arbitrary value, while T being fixed to T_ν – the temperature of neutrino background, related to the temperature of the cosmic microwave background today via $T_{\nu_0} = (4/11)^{1/3} T_{\mathrm{CMB},0}$ (distribution (2.20)).

We start with the case (i). Expressing ρ as a function of T_{FD}, we obtain

$$Q = \frac{gm^4}{\hbar^3} \mathbf{q} \,, \tag{8.13}$$

where numerical constant $\mathbf{q}$ is given by (c.f. [175]):

$$\mathbf{q} = \frac{\zeta^{5/2}(3)}{20\pi^2\sqrt{15}\zeta^{3/2}(5)} \approx 1.96... \times 10^{-3} \,. \tag{8.14}$$

As a result for the distribution (2.4) and fixed number of particles, the quantity $\mathbf{Q}$ is independent on T_{FD}, volume or N. The entropy per particle is also independent on both T_{FD} and V and is given by

$$\frac{S}{N} = \mathbf{s} = I(1)\frac{2}{3\zeta(3)} \approx 4.20\ldots \tag{8.15}$$

Although both quantities S/N and $\mathbf{Q}$ are simply constants, we find it convenient to choose them in the form (2.10):

$$\frac{S}{N} = -\log\left(\frac{Q\hbar^3}{m^4}\right) + \log C_{\mathrm{FD}}, \quad C_{\mathrm{FD}} = g \cdot \mathbf{q} \cdot e^{\mathbf{s}} \approx g \times 0.1311\ldots \tag{8.16}$$

In case (ii) when $F \ll 1$ we obtain for S/N:

$$\frac{S}{N} = \frac{2}{3\zeta(3)}\frac{I(F)}{F} \simeq (1 - \log F) + \frac{2l}{3\zeta(3)} \,. \tag{8.17}$$

Similarly to (8.13)–(8.14)

$$\frac{Q\hbar^3}{m^4} = g\,\mathbf{q}\,F \,. \tag{8.18}$$

Combining (8.17)–(8.18) we can write

$$\frac{S}{N} = -\log\left(\frac{Q\hbar^3}{m^4}\right) + \log C_{\mathrm{NRP}}, \quad C_{\mathrm{NRP}} = g\,\mathbf{q}\exp\left(1 + \frac{2l}{3\zeta(3)}\right) \approx g \times 0.137\ldots \tag{8.19}$$

8.2.2 Mass bounds from the average phase-space density evolution

For illustration purposes we provide in Table 8.1 the average phase-space density estimator Q for all the dSphs, considered in this work, as well as

dSph	Q_f $\left[\frac{M_\odot}{\mathrm{pc}^3}\left(\frac{\mathrm{km}}{\mathrm{sec}}\right)^{-3}\right]$	$m_{\mathrm{FD,HD}}$ [keV]	$m_{\mathrm{NRP,HD}}$ [keV]
Sextans	$5.68^{+10.67}_{-3.07}\cdot10^{-6}$	$0.324^{+0.098}_{-0.057}$	$1.04^{+0.44}_{-0.24}$
Fornax	$8.86^{+12.77}_{-4.40}\cdot10^{-6}$	$0.362^{+0.091}_{-0.051}$	$1.20^{+0.42}_{-0.25}$
Leo I	$1.55^{+3.08}_{-0.85}\cdot10^{-5}$	$0.416^{+0.131}_{-0.075}$	$1.45^{+0.64}_{-0.34}$
UrsaMinor	$1.78^{+2.70}_{-0.90}\cdot10^{-5}$	$0.431^{+0.112}_{-0.070}$	$1.52^{+0.55}_{-0.32}$
Bootes	$3.78^{+2.24}_{-1.48}\cdot10^{-5}$	$0.520^{+0.064}_{-0.061}$	$1.95^{+0.33}_{-0.30}$
Draco	$3.21^{+1.27}_{-0.82}\cdot10^{-5}$	$0.499^{+0.044}_{-0.036}$	$1.85^{+0.22}_{-0.17}$
Carina	$2.60^{+3.42}_{-1.25}\cdot10^{-5}$	$0.474^{+0.111}_{-0.072}$	$1.72^{+0.56}_{-0.34}$
Sculptor	$5.93^{+4.30}_{-2.35}\cdot10^{-5}$	$0.582^{+0.085}_{-0.069}$	$2.27^{+0.45}_{-0.35}$
Leo II	$6.39^{+6.60}_{-2.73}\cdot10^{-5}$	$0.593^{+0.115}_{-0.077}$	$2.32^{+0.62}_{-0.40}$
Canes Venatici I	$6.16^{+4.11}_{-1.94}\cdot10^{-6}$	$0.330^{+0.045}_{-0.030}$	$1.07^{+0.20}_{-0.13}$
Ursa Major I	$1.94^{+1.74}_{-0.84}\cdot10^{-5}$	$0.440^{+0.077}_{-0.058}$	$1.56^{+0.37}_{-0.27}$
Hercules	$2.68^{+4.45}_{-1.53}\cdot10^{-5}$	$0.477^{+0.132}_{-0.091}$	$1.74^{+0.67}_{-0.43}$
Leo T	$6.26^{+9.78}_{-3.16}\cdot10^{-5}$	$0.590^{+0.157}_{-0.095}$	$2.31^{+0.85}_{-0.48}$
Ursa Major II[1]	$1.13^{+1.61}_{-0.55}\cdot10^{-4}$	$0.685^{+0.169}_{-0.104}$	$2.81^{+0.96}_{-0.55}$
Leo IV	$3.35^{+40.91}_{-2.27}\cdot10^{-4}$	$0.898^{+0.814}_{-0.221}$	$4.04^{+5.51}_{-1.27}$
Canes Venatici II	$5.91^{+10.61}_{-3.16}\cdot10^{-4}$	$1.03^{+0.30}_{-0.18}$	$4.88^{+1.99}_{-1.10}$
Coma Berenices	$5.46^{+8.96}_{-2.61}\cdot10^{-4}$	$1.01^{+0.28}_{-0.15}$	$4.75^{+1.82}_{-0.92}$

Table 8.1: The mass bounds, based on the evolution of the average phase-space density Q [175, 176]. The bound is provided for illustration purposes only (see Appendix 8.2.2 for discussion).

the lower mass bounds, based on the inequality (2.9) for Q during the evolution [175, 176] (for detailed discussion see Section 2.2). The value of Q_f, shown in the second column of the Table 8.1 is calculated from the data in the columns (3–4) of the Table 2.4, using formula (2.26) (with $\eta = 1$) and Q_i is defined via (2.8) for the momentum distributions (2.4) and (2.20) (for the bounds $m_{\mathrm{FD,HD}}$ and $m_{\mathrm{NRP,HD}}$ correspondingly). The results for Leo IV are quoted in (2.43) (Section 2.6).

8.3 Appendixes for Chapter 3

8.3.1 Selection criteria for dark matter distributions

We have collected from the literature 1095 dark matter profiles for 357 objects (from dwarf spheroidal galaxies to galaxy clusters, see Table 3.1 below). For each dark matter profile in our sample we have performed a number of checks. Those profiles have not passed these checks were rejected from subsequent analysis. As a result of the selection process we were left with 805 dark matter profiles for 289 objects.

– When analysing the data, we realized that for some objects the value of $r_\star$ lies well outside the region covered by the observational data, R_{data}. Such objects systematically show extremely high values of $r_\star$. For example, we found 37 galaxy profiles having $r_\star > 100$ kpc, while their kinematic data usually extends only up to $R_{\text{data}} \sim 10 - 30$ kpc.

Therefore, we select only dark matter profiles having $r_\star < 2.75 R_{\text{data}}$. The coefficient 2.75 is justified by the following argument. The circular velocity in an NFW halo is given by

$$v_c^2(r) = \frac{G_N M_{\text{NFW}}(< r)}{r} = 4\pi G_N \rho_s r_s^3 \frac{\log(1 + \frac{r}{r_s}) - \frac{r}{r+r_s}}{r}. \qquad (8.20)$$

For $r \ll r_s$ this function can be approximated as

$$v_c^2(r) \approx 2\pi G_N \rho_s r_s \left(r - \frac{4r^2}{3r_s} + \dots \right) \qquad (8.21)$$

In the part of the velocity curve where $\frac{4r^2}{3r_s}$ is much less than the errors on the velocity dispersion one cannot reliably determine r_s and ρ_s (since $v_c^2(r)$ is indistinguishable from a straight line, proportional to $\rho_s r_s$). It is important to have data points in the region where the contribution of the quadratic term becomes noticeable to reliably extract both NFW parameters. We chose to set $2.75 R_{\text{data}} \geq r_\star$, which corresponds to a $\sim 50\%$ contribution from the second (quadratic) term to $v_c^2(r)$. Similar criteria are used for ISO and BURK profiles. This reduces the number of considered profiles from 1095 to 891.

– For 76 objects both NFW and ISO (or BURK) dark matter profiles were available. For these objects we checked the relation between the parameters of these profiles against the results shown in Eq. (3.16) (or Eq. (3.18)

for BURK). Results of this comparison for the NFW and ISO profiles are shown in Fig. 3.4. This figure shows that there is indeed a maximum in the region defined by Eq. (3.16) but also that the scatter around this maximum is pretty large and that the difference between measured and expected ratios of NFW and ISO parameters can be as large as a factor of ten. Therefore we decided to exclude from our sample all objects with a ratio ρ_s/ρ_c, r_s/r_c, (or ρ_s/ρ_B, r_s/r_B for BURK profiles) larger than a factor 5 with respect to the theoretical prediction shown in Eq. (3.16) or (3.18).

– Finally, in several cases parameters of dark matter density profiles were quoted with very large uncertainties. We decided to select only those profiles for which the ratio between the 1σ upper and lower bounds of quoted parameters (radius $r_\star$ or the density $\rho_\star$) was smaller than a factor of 10.

To compare the $\mathcal{S} - M_{\mathrm{halo}}$ relation for selected objects with N-body simulations, we used the results from [307]. This suit of ΛCDM numerical simulations probed the halo mass range $10^{10} - 10^{15} M_\odot$. For each simulated halo of [307] we computed M_{halo}, fit the particle distribution to the NFW density profile and calculate $\mathcal{S}$ using Eqs.(3.9) and the definition (3.7). The observational data together with results from simulations is plotted of the Fig. 8.1. The small scatter of the simulation points at $M_{\mathrm{halo}} \gtrsim 10^{14} M_\odot$ is explained by the finite size of the simulation box. The simulations with the large box size (e.g. [310]) verify that the scatter does not reduce at large masses (c.f. the pink shaded region on the Figure 1).

8.3.2   Summary of collected dark matter distributions

We collected from the literature 1095 dark matter density profiles for 357 unique objects ranging from dSphs to galaxy clusters. For each dark matter profile found in our sample we have applied uniform selection criteria:

– If for an object several independently determined profiles were available and all of them but one agreed in the values of $r_\star$ and $\rho_\star$ within a factor of 5, we rejected the outlier.

– For some objects the best-fit value of the characteristic radius $r_\star$ was extrapolated well outside the region covered by the observational data, R_{data}. In this case the parameters of the density profile had extremely large uncertainties. We have thus rejected objects with $r_\star < 2.75 R_{\mathrm{data}}$.
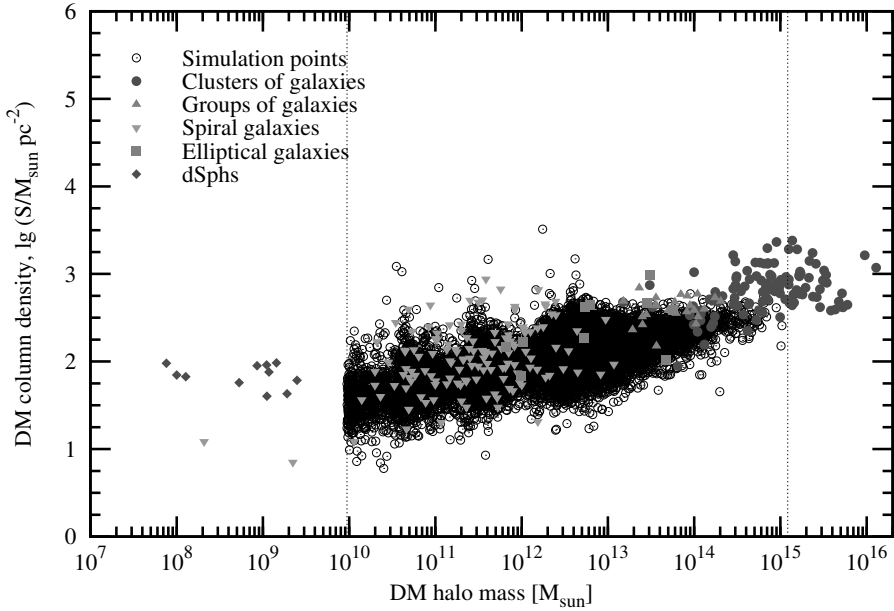
Figure 8.1: **Dark matter column density as a function of the halo mass.** Similar to the Figure 1, we plot 289 objects, selected in Section 8.3.1 above (coloured shapes) superimposed on the simulation data for isolated halos [307] (open black circles).

– We rejected profiles for which the uncertainty in any quoted parameter ($r_\star$ or $\rho_\star$) was higher than a factor of 10.

– For objects with more than one profile selected, the average value of $\mathcal{S}$ and M_{halo} was used in the subsequent analysis.

– When processing the data of N-body simulations we used the fit of particle distribution by the NFW density profile and computed $\mathcal{S}$, using equation (3.7).

– If *the same* observational data is fit by several different dark matter profiles (e.g. NFW, ISO, and BURK), one can then find a relation between characteristic scales $r_\star$ and densities $\rho_\star$ of these profiles. Provided such a relation holds, the difference between the column densities $\mathcal{S}_{\mathrm{NFW}}$, $\mathcal{S}_{\mathrm{BURK}}$ and $\mathcal{S}_{\mathrm{ISO}}$ turns out to be less than 10%. Qualitatively, this can be un-

derstood as follows: to explain the same velocity data, two dark matter profiles should have roughly the same mass within some radius R_0. If both profiles happen to have the same behaviour at large distances, their $\mathcal{S}$ values, averaged over R_0 will be essentially equal. This explains the use of $\mathcal{S}$ as a characteristic of dark matter halos.

8.4   Appendixes for Chapter 5

8.4.1   Cleaning of soft proton flares

EPIC external "flaring" background is caused by protons of energies less than a few $\times 100\,\mathrm{keV}$, collected by the X-ray mirrors. These protons originate in the Earth's magnetosphere. During the flaring periods, the background level increases by one-two orders of magnitude. According to [329] they have very hard and unpredictable spectral shape usually dominating at high energies which makes their modeling technically challenging. In addition to that, due to their different convolution with effective area comparing to X-ray photons they are responsible for some artificial line-like features, for instance at ∼2.5 keV [323].

 Several different procedures have been developed by different authors. For completeness we present their brief overview here.

1. The "standard" method used by [334] is based on the construction of ≥ 10 keV lightcurves for single pixel events binned by 100 s. The intervals having more 0.2 cts/s for MOS1/MOS2 and 0.45 cts/s for PN cameras in this energy range are rejected. However, the authors find that some flares "survive" after this procedure creating the variability in 1-10 keV band. This effect is attributed to the existence of lower energy protons at the edges of the encountered proton "clouds". Therefore, the additional screening at 1-10 keV range (allowing MOS countrates to be smaller than 1.15 cts/s) is performed.

2. In [330], the authors developed an algorithm to obtain an automated and homogeneous screening from the flaring non-X-ray background. During the first step, the 0.4-12 keV MOS lightcurves were extracted from events coming to the instrument's FoV and binned by 30 s intervals. Then, the histogram of count rates is created. After fitting this histogram with a Gaussian function, the intervals having the countrate

more than 3.3 σ larger than the mean value are rejected. After the rejection, additional test of the high-energy countrates is performed by using the events from parts of MOS CCDs located *not* in the instrument's FoV. Because at high energies ($\gtrsim 5\,\mathrm{keV}$) the blank-sky spectrum is dominated by the instrumental background [326, 334], comparison of in-FoV and out-FoV countrates at these energies may idenfity the additional in-FoV high-energy component caused by soft proton flares passed through their 3.3 σ filter.

3. In [326], the authors used the "double filtering" procedure removing time intervals with either high-energy (9.5-12 keV for MOS, 10-14 keV for PN) and low-energy (1-5 keV) countrates deviating more than by 20 % for the average values. Such a filtering removed ~ 35 % of MOS and ~ 45 % of PN uncleaned exposure.

4. In [353], the authors first apply the lightcurve filtering in a wide band (0.2-12 keV for MOS) camera. After removing time intervals with countrate above 2-2.5σ above the mean level, they perform the point source detection procedure. After removal the point sources, they again perform the lightcurve cleaning. Due to removal of point sources, the sensitivity for for faint flare search is significantly increased allowing them to exclude additional $\sim$10 % of exposure affected by the smallest flares.

5. In [329], the authors idenfitied the flaring intervals using the procedure similar to [330]. By cleaning time intervals with 2.5-8.0 keV MOS countrates exceeding more than by 2.5 σ the mean value, they remove ~ 36 % of MOS uncleaned exposure. In addition, the authors model the remaining soft proton component with the broken powerlaw (without convolving with the instrument effective area) with $E_{br} \simeq 3.2$ keV.

6. In [328], the authors first exclude time bins where the high-energy (10-12 keV) MOS countrate is larger than 0.2 cts/s (for 100 s bins). After that, a 2-5 keV histogram is produced and modeled similar to [330] and all bins with countrates more than 3σ above the mean value are also rejected. Finally, $F_{in} - F_{out}$ diagnostic of [330] is used to estimate the residual soft proton flare contamination. All observations with $F_{in} - F_{out}$ less than 1.5 were used for subsequent analysis.

7. In [421, 422], the authors use the procedure `mos-filter`, developed

by the authors of [329] as a part of *XMM-Newton* Extended Sources Analysis Software (XMM-ESAS), now the part of XMM SAS. In this procedure, 2.5-12 keV lightcurve is binned by 1 s intervals and all intervals with count rates different from mean value more than by 1.5 σ were rejected.

8.4.2 Modeling closed-filter spectra.

In this Section, we model closed-filter spectrum in Xspec using very simple powerlaw model in 2.3-10.0 keV energy range. The energy bins around strong instrumental lines (namely, 5.3-5.7, 5.8-6.0, 6.3-6.6, 7.4-7.7, 8.0-8.2, 8.5-8.8, 9.5-9.8 keV for MOS cameras and 5.3-5.7, 5.8-6.0, 6.3-6.6, 7.0-9.1, 9.3-9.7 keV) are removed. The results of fit are very good, see Table 8.2 and Fig. 8.2 for details. The measurements of the powerlaw index are consistent with previous results of [334] (who obtained $\alpha_{hard} \sim 0.2$, $\alpha_{soft} \sim 0.8$ and $E_{br} \sim 1$ keV for MOS cameras) and [326] (who obtained $\alpha_{soft} = 0.7 - 0.8$, $E_{br} = 1.3 - 1.5$ keV and $\alpha_{hard} = 0.4$ for PN and $\alpha_{hard} = 0.1 - 0.2$ for MOS cameras). The large difference between the values α_{hard} between MOS and PN cameras is *not* unexpected. According to [334], about ~ 99 % of cosmic rays are rejected by internal electronics by using multiple pixel analysis (due to large energy deposition of cosmic rays they mostly interact with several adjacent CCD pixels). The sizes of CCD pixels for MOS (1.1 arcsec) and PN (4.1 arcsec) are very different, so we expect the very different outcome of internal rejection of cosmic rays in these cameras.

	MOS1	MOS2	PN
Fit quality, total χ^2/d.o.f.	360.5/369	373.6/369	831.0/849
Powerlaw index	0.183±0.007	0.177±0.007	0.402±0.010
Norm., cts/s/keV at 1 keV	0.0480±0.0006	0.0464±0.0006	0.090±0.002

Table 8.2: Model parameters of closed filter background on powerlaw continuum (without RMF or ARF).

8.4.3 Adding simulated lines to the combined dataset

Line simulations are performed using standard routine fakeit, a part of Xspec spectral fitting package [409]. We adopt the following procedure of
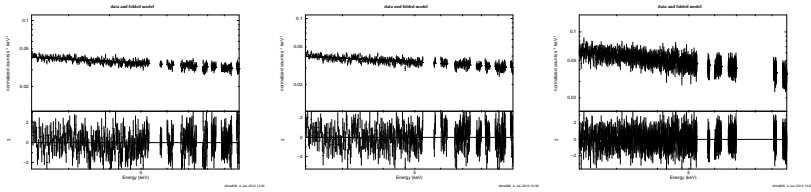
Figure 8.2: Best-fit continuum model and fit residuals for closed-filter background spectra from MOS1 (*left*), MOS2 (*centre*) and PN (*right*) cameras. The energy ranges containing strong instrumental lines are excluded from the fit, see text for details. The resulting energy bins are well modeled with simple `powerlaw` continuum, see 8.2 for details. This result ensures that we may really use *modeling* of closed-filter background, instead of *subtracting* it.

line simulation. First, we simulated a narrow line for each observation having the same flux (in photons $cm^{-2}s^{-1}$). The initial line energy and dispersion (set to 1 eV)[2] are kept the same. We repeat many times, adding the line to each individual observation, prior to stacking them together. In each energy bin (15 eV for MOS camera and 5 eV for PN camera) the total number of counts is allowed to vary according to Poisson distribution allowing to create different realizations of the line. The actual shapes of line broadening and effective area is taken into account by using instrument responses for each observation contained in RMF and ARF files, see Sec. 5.2.4 for details. After simulating spectra for each observation of our combined dataset, the spectra from each camera (MOS1, MOS2, PN) are dumped to text format using FTOOL `fdump`, binned by 60 eV per bin.

---

[2]Predicted internal dispersion of dark matter decay line due to Doppler broadening is about 10^{-3} times line energy for galaxies [229]. However, because total dispersion is the root of the squared sum of initial dispersion ($\lesssim 10$ eV) and line broadening ($\gtrsim 50$ eV), the corresponding error on total dispersion does not exceed 2% and is neglected henceforth.

References

[1] Zwicky, F. Die Rotverschiebung von extragalaktischen Nebeln. *Helvetica Physica Acta* **6**, 110–127 (1933).

[2] Einasto, J. Dark Matter. *Baltic Astronomy* **20**, 231–240 (2011). `1109.5580`.

[3] Einasto, J. Dark Matter. *ArXiv e-prints* (2009). `0901.0632`.

[4] Roos, M. Astrophysical and Cosmological Probes of Dark Matter. *Journal of Modern Physics* **3**, 1152–1171 (2012). `1208.3662`.

[5] Massey, R., Kitching, T. & Richard, J. The dark matter of gravitational lensing. *Reports on Progress in Physics* **73**, 086901 (2010). `1001.1739`.

[6] Walker, M. G. Dark Matter in the Milky Way's Dwarf Spheroidal Satellites. *ArXiv e-prints* (2012). `1205.0311`.

[7] Dekel, A. *et al.* Lost and found dark matter in elliptical galaxies. Nature **437**, 707–710 (2005). `arXiv:astro-ph/0501622`.

[8] Noordermeer, E., van der Hulst, J. M., Sancisi, R., Swaters, R. S. & van Albada, T. S. The mass distribution in early-type disc galaxies: declining rotation curves and correlations with optical properties. MNRAS **376**, 1513–1546 (2007). `arXiv:astro-ph/0701731`.

[9] Coccato, L. *et al.* Kinematic properties of early-type galaxy haloes using planetary nebulae. MNRAS **394**, 1249–1283 (2009). `0811.3203`.

[10] Gilmore, G. *et al.* The Observed Properties of Dark Matter on Small Spatial Scales. ApJ **663**, 948–959 (2007). `arXiv:astro-ph/0703308`.

[11] Corbelli, E., Lorenzoni, S., Walterbos, R., Braun, R. & Thilker, D. A wide-field H I mosaic of Messier 31. II. The disk warp, rotation, and

the dark matter halo. A&A **511**, A89 (2010). `0912.4133`.

[12] Chemin, L., Carignan, C. & Foster, T. HI kinematics and dynamics of Messier 31. *Astrophys. J.* **705**, 1395–1415 (2009). `0909.3846`.

[13] Sarazin, C. L. X-ray emission from clusters of galaxies. *Reviews of Modern Physics* **58**, 1–115 (1986).

[14] Einasto, J. & Einasto, M. Dark Matter in Groups and Clusters of Galaxies. In Valtonen, M. J. & Flynn, C. (eds.) *IAU Colloq. 174: Small Galaxy Groups*, vol. 209 of *Astronomical Society of the Pacific Conference Series*, 360 (2000). `arXiv:astro-ph/9909437`.

[15] Evrard, A. E., Metzler, C. A. & Navarro, J. F. Mass Estimates of X-Ray Clusters. ApJ **469**, 494 (1996). `arXiv:astro-ph/9510058`.

[16] Buote, D. A. X-Ray Constraints on Dark Matter in Galaxy Clusters and Elliptical Galaxies: A View from Chandra and XMM. In Ryder, S., Pisano, D., Walker, M. & Freeman, K. (eds.) *Dark Matter in Galaxies*, vol. 220 of *IAU Symposium*, 149 (2004). `arXiv:astro-ph/0310579`.

[17] Refregier, A. Weak Gravitational Lensing by Large-Scale Structure. ARA&A **41**, 645–668 (2003). `arXiv:astro-ph/0307212`.

[18] Bergström, L. Non-baryonic dark matter: observational evidence and detection methods. *Reports on Progress in Physics* **63**, 793–841 (2000). `arXiv:hep-ph/0002126`.

[19] Massey, R. *et al.* Dark matter maps reveal cosmic scaffolding. Nature **445**, 286–290 (2007). `arXiv:astro-ph/0701594`.

[20] Fu, L. *et al.* Very weak lensing in the CFHTLS wide: cosmology from cosmic shear in the linear regime. A&A **479**, 9–25 (2008). `0712.0884`.

[21] Komatsu, E. *et al.* Seven-year Wilkinson Microwave Anisotropy Probe (WMAP) Observations: Cosmological Interpretation. ApJS **192**, 18–+ (2011). `1001.4538`.

[22] Rozo, E. *et al.* Cosmological Constraints from the Sloan Digital Sky Survey maxBCG Cluster Catalog. ApJ **708**, 645–660 (2010). `0902.3702`.

[23] Reid, B. A. *et al.* Cosmological constraints from the clustering of the Sloan Digital Sky Survey DR7 luminous red galaxies. MNRAS **404**,

60–85 (2010). `0907.1659`.

[24] Mantz, A., Allen, S. W., Rapetti, D. & Ebeling, H. The observed growth of massive galaxy clusters - I. Statistical methods and cosmological constraints. MNRAS **406**, 1759–1772 (2010). `0909.3098`.

[25] Tinker, J. L. *et al.* Cosmological Constraints from Galaxy Clustering and the Mass-to-number Ratio of Galaxy Clusters. ApJ **745**, 16 (2012). `1104.1635`.

[26] Frenk, C. S. & White, S. D. M. Dark matter and cosmic structure. *Annalen der Physik* **524**, 507–534 (2012). `1210.0544`.

[27] Gates, E. I., Gyuk, G. & Turner, M. S. The Local Halo Density. ApJ **449**, L123 (1995). `arXiv:astro-ph/9505039`.

[28] Lasserre, T. *et al.* Not enough stellar mass Machos in the Galactic halo. A&A **355**, L39–L42 (2000). `arXiv:astro-ph/0002253`.

[29] Alcock, C. *et al.* Binary Microlensing Events from the MACHO Project. ApJ **541**, 270–297 (2000).

[30] Moniez, M. Microlensing as a probe of the Galactic structure: 20 years of microlensing optical depth studies. *General Relativity and Gravitation* **42**, 2047–2074 (2010). `1001.2707`.

[31] Dar, A. Baryonic Dark Matter and Big Bang Nucleosynthesis. ApJ **449**, 550–+ (1995). `arXiv:astro-ph/9504082`.

[32] Carr, B. J. Primordial Black Holes: Do They Exist and Are They Useful? *ArXiv Astrophysics e-prints* (2005). `arXiv:astro-ph/0511743`.

[33] Capela, F., Pshirkov, M. & Tinyakov, P. Constraints on Primordial Black Holes as Dark Matter Candidates from Star Formation. *ArXiv e-prints* (2012). `1209.6021`.

[34] Wojtak, R., Hansen, S. H. & Hjorth, J. Gravitational redshift of galaxies in clusters as predicted by general relativity. Nature **477**, 567–569 (2011). `1109.6571`.

[35] Dodelson, S. The Real Problem with MOND. *International Journal of Modern Physics D* **20**, 2749–2753 (2011). `1112.1320`.

[36] Bekenstein, J. D. & Sanders, R. H. TeVeS/MOND is in harmony with gravitational redshifts in galaxy clusters. MNRAS **421**, L59–L61

(2012). `1110.5048`.

[37] Moffat, J. W. & Toth, V. T. Comment on "The Real Problem with MOND" by Scott Dodelson, arXiv:1112.1320. *ArXiv e-prints* (2011). `1112.4386`.

[38] Bertone, G., Hooper, D. & Silk, J. Particle dark matter: evidence, candidates and constraints. Phys. Rep. **405**, 279–390 (2005). `arXiv: hep-ph/0404175`.

[39] Bertone, G. *Particle Dark Matter : Observations, Models and Searches* (Cambridge University Press, 2010).

[40] Taoso, M., Bertone, G. & Masiero, A. Dark Matter Candidates: A Ten-Point Test. *JCAP* **0803**, 022 (2008). `0711.4996`.

[41] Drees, M. & Gerbier, G. Mini–Review of Dark Matter: 2012. *ArXiv e-prints* (2012). `1204.2373`.

[42] Fogli, G. L., Lisi, E., Marrone, A. & Palazzo, A. Global analysis of three-flavor neutrino masses and mixings. *Progress in Particle and Nuclear Physics* **57**, 742–795 (2006). `arXiv:hep-ph/0506083`.

[43] Lesgourgues, J. & Pastor, S. Massive neutrinos and cosmology. *Phys. Rept.* **429**, 307–379 (2006). `astro-ph/0603494`.

[44] Nakamura, K. *et al.* Review of particle physics. *J.Phys.G* **G37**, 075021 (2010).

[45] Tremaine, S. & Gunn, J. E. Dynamical role of light neutral leptons in cosmology. *Physical Review Letters* **42**, 407–410 (1979).

[46] Boyarsky, A., Ruchayskiy, O. & Iakubovskyi, D. A lower bound on the mass of dark matter particles. *Journal of Cosmology and Astro-Particle Physics* **3**, 5–+ (2009). `0808.3902`.

[47] Davis, M., Efstathiou, G., Frenk, C. S. & White, S. D. M. The evolution of large-scale structure in a universe dominated by cold dark matter. ApJ **292**, 371–394 (1985).

[48] Madsen, J. Phase-space constraints on bosonic and fermionic dark matter. *Physical Review Letters* **64**, 2744–2746 (1990).

[49] Madsen, J. Generalized Tremaine-Gunn limits for bosons and fermions. Phys. Rev. D **44**, 999–1006 (1991).

[50] Boyarsky, A. & Ruchayskiy, O. Bounds on Light Dark Matter. *ArXiv e-prints* (2008). `0811.2385`.

[51] Feng, J. L. Dark Matter Candidates from Particle Physics and Methods of Detection. ARA&A **48**, 495–545 (2010). `1003.0904`.

[52] Lee, B. W. & Weinberg, S. Cosmological lower bound on heavy-neutrino masses. *Physical Review Letters* **39**, 165–168 (1977).

[53] Saab, T. An Introduction to Dark Matter Direct Detection Searches and Techniques. *ArXiv e-prints* (2012). `1203.2566`.

[54] Lavalle, J. & Salati, P. Dark matter indirect signatures. *Comptes Rendus Physique* **13**, 740–782 (2012). `1205.1004`.

[55] Bergstrom, L. Saas-Fee Lecture Notes: Multi-messenger Astronomy and Dark Matter. *ArXiv e-prints* (2012). `1202.1170`.

[56] Dodelson, S. & Widrow, L. M. Sterile neutrinos as dark matter. *Physical Review Letters* **72**, 17–20 (1994). `arXiv:hep-ph/9303287`.

[57] Asaka, T., Blanchet, S. & Shaposhnikov, M. The numsm, dark matter and neutrino masses. *Phys. Lett.* **B631**, 151–156 (2005). `hep-ph/0503065`.

[58] Lattanzi, M. & Valle, J. W. F. Decaying Warm Dark Matter and Neutrino Masses. *Physical Review Letters* **99**, 121301–+ (2007). `0705.2406`.

[59] Wilczek, F. Problem of strong P and T invariance in the presence of instantons. *Physical Review Letters* **40**, 279–282 (1978).

[60] Weinberg, S. A new light boson? *Physical Review Letters* **40**, 223–226 (1978).

[61] Holman, R., Lazarides, G. & Shafi, Q. Axions and the dark matter of the Universe. Phys. Rev. D **27**, 995–997 (1983).

[62] Pagels, H. & Primack, J. R. Supersymmetry, cosmology, and new physics at teraelectronvolt energies. *Physical Review Letters* **48**, 223–226 (1982).

[63] Haber, H. E. & Kane, G. L. The search for supersymmetry: Probing physics beyond the standard model. Phys. Rep. **117**, 75–263 (1985).

[64] Covi, L., Kim, J. E. & Roszkowski, L. Axinos as Cold Dark Matter. *Physical Review Letters* **82**, 4180–4183 (1999). `arXiv:hep-ph/9905212`.

[65] Takayama, F. & Yamaguchi, M. Gravitino dark matter without R-parity. *Physics Letters B* **485**, 388–392 (2000). `arXiv:hep-ph/0005214`.

[66] Covi, L., Kim, H. B., Kim, J. E. & Roszkowski, L. Axinos as dark matter. *Journal of High Energy Physics* **5**, 33 (2001). `arXiv:hep-ph/0101009`.

[67] Feng, J. L., Rajaraman, A. & Takayama, F. Superweakly Interacting Massive Particles. *Physical Review Letters* **91**, 011302–+ (2003). `arXiv:hep-ph/0302215`.

[68] Feng, J. L., Su, S. & Takayama, F. SuperWIMP gravitino dark matter from slepton and sneutrino decays. Phys. Rev. D **70**, 063514–+ (2004). `arXiv:hep-ph/0404198`.

[69] Buchmüller, W., Covi, L., Hamaguchi, K., Ibarra, A. & Yanagida, T. T. Gravitino dark matter in R-parity breaking vacua. *Journal of High Energy Physics* **3**, 37–+ (2007). `arXiv:hep-ph/0702184`.

[70] Conlon, J. P. & Quevedo, F. Astrophysical and cosmological implications of large volume string compactifications. *Journal of Cosmology and Astro-Particle Physics* **8**, 19–+ (2007). `0705.3460`.

[71] Kusenko, A., Loewenstein, M. & Yanagida, T. T. Moduli dark matter and the search for its decay line using Suzaku X-ray telescope. *ArXiv e-prints* (2012). `1209.6403`.

[72] Bezrukov, F. & Shaposhnikov, M. Searching for dark matter sterile neutrinos in the laboratory. Phys. Rev. D **75**, 053005–+ (2007). `arXiv:hep-ph/0611352`.

[73] Dolgov, A. D. & Hansen, S. H. Massive sterile neutrinos as warm dark matter. *Astroparticle Physics* **16**, 339–344 (2002). `arXiv:hep-ph/0009083`.

[74] Abazajian, K., Fuller, G. M. & Tucker, W. H. Direct Detection of Warm Dark Matter in the X-Ray. ApJ **562**, 593–604 (2001). `arXiv:astro-ph/0106002`.

[75] den Herder, J. W. *et al.* The search for decaying Dark Matter. *ArXiv e-prints* (2009). `0906.1788`.

[76] Abazajian, K. N. *et al.* Light Sterile Neutrinos: A White Paper. *ArXiv e-prints* (2012). `1204.5379`.

[77] Supper, R. *et al.* ROSAT PSPC survey of M 31. A&A **317**, 328–349 (1997).

[78] Shi, X. & Fuller, G. M. New Dark Matter Candidate: Nonthermal Sterile Neutrinos. *Physical Review Letters* **82**, 2832–2835 (1999). `arXiv:astro-ph/9810076`.

[79] Abazajian, K., Fuller, G. M. & Patel, M. Sterile neutrino hot, warm, and cold dark matter. Phys. Rev. D **64**, 023501 (2001). `arXiv:astro-ph/0101524`.

[80] Asaka, T. & Shaposhnikov, M. The nuMSM, dark matter and baryon asymmetry of the universe. *Phys. Lett. B* **620**, 17–26 (2005). `arXiv:hep-ph/0505013`.

[81] Asaka, T., Shaposhnikov, M. & Laine, M. Lightest sterile neutrino abundance within the νMSM. *Journal of High Energy Physics* **1**, 91–+ (2007). `arXiv:hep-ph/0612182`.

[82] Boyarsky, A., Ruchayskiy, O. & Shaposhnikov, M. The Role of Sterile Neutrinos in Cosmology and Astrophysics. *Annual Review of Nuclear and Particle Science* **59**, 191–214 (2009). `0901.0011`.

[83] Kusenko, A. Sterile neutrinos: The dark side of the light fermions. Phys. Rep. **481**, 1–28 (2009). `0906.2968`.

[84] Boyarsky, I. D., A. & Ruchayskiy, O. Next decade of sterile neutrino studies (2012). `http://dx.doi.org/10.1016/j.dark.2012.11.001`.

[85] Cho, A. Physicists' nightmare scenario: The higgs and nothing else. *Science* **315**, 1657–1658 (2007). URL `http://www.sciencemag.org/content/315/5819/1657.short`. `http://www.sciencemag.org/content/315/5819/1657.full.pdf`.

[86] Asaka, T., Laine, M. & Shaposhnikov, M. On the hadronic contribution to sterile neutrino production. *Journal of High Energy Physics* **6**, 53 (2006). `arXiv:hep-ph/0605209`.

[87] Shaposhnikov, M. The nuMSM, leptonic asymmetries, and properties of singlet fermions. *Journal of High Energy Physics* **8**, 8 (2008). `0804.4542`.

[88] Laine, M. & Shaposhnikov, M. Sterile neutrino dark matter as a consequence of nuMSM-induced lepton asymmetry. *Journal of Cosmology and Astro-Particle Physics* **6**, 31–+ (2008). `0804.4543`.

[89] Minkowski, P. mu → e gamma at a rate of one out of 1-billion muon decays? *Phys. Lett.* **B67**, 421 (1977).

[90] Ramond, P. The family group in grand unified theories (1979). `hep-ph/9809459`.

[91] Mohapatra, R. N. & Senjanovic, G. Neutrino mass and spontaneous parity nonconservation. *Phys. Rev. Lett.* **44**, 912 (1980).

[92] Yanagida, T. Horizontal gauge symmetry and masses of neutrinos. *Prog. Theor. Phys.* **64**, 1103 (1980).

[93] Boyarsky, A., Neronov, A., Ruchayskiy, O. & Shaposhnikov, M. Masses of active neutrinos in the nuMSM from x-ray astronomy. *Soviet Journal of Experimental and Theoretical Physics Letters* **83**, 133–135 (2006). `arXiv:hep-ph/0601098`.

[94] Gorbunov, D. & Shaposhnikov, M. How to find neutral leptons of the numsm? *JHEP* **10**, 015 (2007). `arXiv:0705.1729[hep-ph]`.

[95] Gorbunov, D. & Shaposhnikov, M. Search for GeV-scale sterile neutrinos responsible for active neutrino masses and baryon asymmetry of the universe. Submitted to European Strategy Preparatory Group. Available at `http://indico.cern.ch/contributionDisplay.py?contribId=17&confId=175067`.

[96] Hewett, J. L. *et al.* Fundamental Physics at the Intensity Frontier. *ArXiv e-prints* (2012). `1205.2671`.

[97] Canetti, L., Drewes, M. & Shaposhnikov, M. Sterile Neutrinos as the Origin of Dark and Baryonic Matter. *ArXiv e-prints* (2012). `1204.3902`.

[98] Pal, P. B. & Wolfenstein, L. Radiative decays of massive neutrinos. Phys. Rev. D **25**, 766–773 (1982).

[99] Boyarsky, A., Lesgourgues, J., Ruchayskiy, O. & Viel, M. Lyman-α constraints on warm and on warm-plus-cold dark matter models. *Journal of Cosmology and Astro-Particle Physics* **5**, 12–+ (2009). `0812.0010`.

[100] Peebles, P. J. E. *The large-scale structure of the universe* (Princeton, N.J., Princeton University Press, 1980. 435 p., 1980).

[101] Zel'dovich, Y. B. Gravitational instability: An approximate theory for large density perturbations. A&A **5**, 84–89 (1970).

[102] Bisnovatyi-Kogan, G. S. Cosmology with a nonzero neutrino rest mass. AZh **57**, 899–902 (1980).

[103] Bond, J. R., Efstathiou, G. & Silk, J. Massive neutrinos and the large-scale structure of the universe. *Physical Review Letters* **45**, 1980–1984 (1980).

[104] Doroshkevich, A. G., Khlopov, M. I., Sunyaev, R. A., Szalay, A. S. & Zeldovich, I. B. Cosmological impact of the neutrino rest mass. *New York Academy Sciences Annals* **375**, 32–42 (1981).

[105] Bode, P., Ostriker, J. P. & Turok, N. Halo Formation in Warm Dark Matter Models. ApJ **556**, 93–107 (2001). `arXiv:astro-ph/0010389`.

[106] Asaka, T., Shaposhnikov, M. & Kusenko, A. Opening a new window for warm dark matter. *Phys. Lett.* **B638**, 401–406 (2006). `hep-ph/0602150`.

[107] Bezrukov, F., Hettmansperger, H. & Lindner, M. keV sterile neutrino dark matter in gauge extensions of the standard model. Phys. Rev. D **81**, 085032–+ (2010). `0912.4415`.

[108] Wolfenstein, L. Neutrino oscillations in matter. *Phys. Rev.* **D17**, 2369–2374 (1978).

[109] Mikheev, S. P. & Smirnov, A. Y. Resonance enhancement of oscillations in matter and solar neutrino spectroscopy. *Sov. J. Nucl. Phys.* **42**, 913–917 (1985).

[110] Lesgourgues, J. & Pastor, S. Cosmological implications of a relic neutrino asymmetry. Phys. Rev. D **60**, 103521–+ (1999). `hep-ph/9904411`.

[111] Kirilova, D. On Lepton asymmetry and BBN. *Progress in Particle and*

Nuclear Physics **66**, 260–265 (2011).

[112] Serpico, P. D. & Raffelt, G. G. Lepton asymmetry and primordial nucleosynthesis in the era of precision cosmology. *Phys. Rev.* **D71**, 127301 (2005). `astro-ph/0506162`.

[113] Mangano, G., Miele, G., Pastor, S., Pisanti, O. & Sarikas, S. Constraining the cosmic radiation density due to lepton number with Big Bang Nucleosynthesis. *JCAP* **1103**, 035 (2011). `1011.0916`.

[114] Castorina, E. *et al.* Cosmological lepton asymmetry with a nonzero mixing angle θ_{13}. *Phys.Rev.* **D86**, 023517 (2012). `1204.2510`.

[115] Benson, A. J. *et al.* Dark Matter Halo Merger Histories Beyond Cold Dark Matter: I - Methods and Application to Warm Dark Matter (2012). `1209.3018`.

[116] Sommer-Larsen, J., Naselsky, P., Novikov, I. & Gotz, M. Inhomogenous Primordial Baryon Distributions on Sub- Galactic Scales: High-z Galaxy Formation with WDM. *Mon. Not. Roy. Astron. Soc.* **352**, 299 (2004). `astro-ph/0309329`.

[117] O'Shea, B. W. & Norman, M. L. Population III star formation in a Lambda WDM universe. *Astrophys. J.* **648**, 31–46 (2006). `astro-ph/0602319`.

[118] Gao, L. & Theuns, T. Lighting the Universe with filaments. *Science* **317**, 1527 (2007). `0709.2165`.

[119] Hansen, S. H. & Haiman, Z. Do we need stars to reionize the universe at high redshifts? Early reionization by decaying heavy sterile neutrinos. *Astrophys.J.* **600**, 26–31 (2004). `astro-ph/0305126`.

[120] Yoshida, N., Sokasian, A., Hernquist, L. & Springel, V. Early Structure Formation and Reionization in a Warm Dark Matter Cosmology. *Astrophys. J.* **591**, L1–L4 (2003). `astro-ph/0303622`.

[121] Yue, B. & Chen, X. Reionization in the Warm Dark Matter Model. *Astrophys.J.* **747**, 127 (2012). `1201.3686`.

[122] Hansen, S. H., Lesgourgues, J., Pastor, S. & Silk, J. Closing the window on warm dark matter. *MNRAS* **333**, 544–546 (2002). `astro-ph/0106108`.

[123] Viel, M., Lesgourgues, J., Haehnelt, M. G., Matarrese, S. & Riotto, A. Constraining warm dark matter candidates including sterile neutrinos and light gravitinos with wmap and the Lyman- alpha forest. *Phys. Rev.* **D71**, 063534 (2005). `astro-ph/0501562`.

[124] Viel, M., Lesgourgues, J., Haehnelt, M. G., Matarrese, S. & Riotto, A. Can sterile neutrinos be ruled out as warm dark matter candidates? *Phys. Rev. Lett.* **97**, 071301 (2006). `astro-ph/0605706`.

[125] Seljak, U., Makarov, A., McDonald, P. & Trac, H. Can sterile neutrinos be the dark matter? *Phys. Rev. Lett.* **97**, 191303 (2006). `astro-ph/0602430`.

[126] Viel, M. *et al.* How cold is cold dark matter? Small scales constraints from the flux power spectrum of the high-redshift Lyman-alpha forest. *Phys. Rev. Lett.* **100**, 041304 (2008). `0709.0131`.

[127] Strigari, L. E. *et al.* A large dark matter core in the fornax dwarf spheroidal galaxy? ApJ **652**, 306–312 (2006). `arXiv:astro-ph/0603775`.

[128] Colin, P., Valenzuela, O. & Avila-Reese, V. On the Structure of Dark Matter Halos at the Damping Scale of the Power Spectrum with and without Relict Velocities. *Astrophys. J.* **673**, 203–214 (2008). `0709.4027`.

[129] de Naray, R. K., Martinez, G. D., Bullock, J. S. & Kaplinghat, M. The Case Against Warm or Self-Interacting Dark Matter as Explanations for Cores in Low Surface Brightness Galaxies (2009). `0912.3518`.

[130] Schneider, A., Smith, R. E., Maccio, A. V. & Moore, B. Nonlinear Evolution of Cosmological Structures in Warm Dark Matter Models (2011). `1112.0330`.

[131] Boyarsky, A., Lesgourgues, J., Ruchayskiy, O. & Viel, M. Realistic Sterile Neutrino Dark Matter with KeV Mass does not Contradict Cosmological Bounds. *Physical Review Letters* **102**, 201304–+ (2009). `0812.3256`.

[132] Jedamzik, K., Lemoine, M. & Moultaka, G. Gravitino, axino, Kaluza-Klein graviton warm and mixed dark matter and reionisation. *JCAP* **0607**, 010 (2006). `astro-ph/0508141`.

[133] Lovell, M. *et al.* The Haloes of Bright Satellite Galaxies in a Warm Dark Matter Universe. MNRAS *to appear* (2011). `1104.2929`.

[134] Klypin, A., Kravtsov, A. V., Valenzuela, O. & Prada, F. Where Are the Missing Galactic Satellites? ApJ **522**, 82–92 (1999). `arXiv: astro-ph/9901240`.

[135] Moore, B. *et al.* Dark matter substructure within galactic halos. *Astrophys. J.* **524**, L19–L22 (1999). `arXiv:astro-ph/9907411`.

[136] Bullock, J. S., Kravtsov, A. V. & Weinberg, D. H. Reionization and the Abundance of Galactic Satellites. ApJ **539**, 517–521 (2000). `arXiv: astro-ph/0002214`.

[137] Benson, A. J., Frenk, C. S., Lacey, C. G., Baugh, C. M. & Cole, S. The effects of photoionization on galaxy formation - II. Satellite galaxies in the Local Group. MNRAS **333**, 177–190 (2002). `arXiv:astro-ph/0108218`.

[138] Somerville, R. S. Can Photoionization Squelching Resolve the Substructure Crisis? ApJ **572**, L23–L26 (2002). `arXiv:astro-ph/0107507`.

[139] Macciò, A. V. *et al.* Luminosity function and radial distribution of Milky Way satellites in a ΛCDM Universe. MNRAS **402**, 1995–2008 (2010). `0903.4681`.

[140] Strigari, L. E., Frenk, C. S. & White, S. D. M. Kinematics of Milky Way satellites in a Lambda cold dark matter universe. MNRAS **408**, 2364–2372 (2010). `1003.4268`.

[141] Boylan-Kolchin, M., Bullock, J. S. & Kaplinghat, M. Too big to fail? The puzzling darkness of massive Milky Way subhalos. MNRAS **415**, L40–L44 (2011). `1103.0007`.

[142] Stasielak, J., Biermann, P. L. & Kusenko, A. Thermal evolution of the primordial clouds in warm dark matter models with kev sterile neutrinos. ApJ **654**, 290–303 (2007). `arXiv:astro-ph/0606435`.

[143] Ripamonti, E., Mapelli, M. & Ferrara, A. The impact of dark matter decays and annihilations on the formation of the first structures. *Mon. Not. Roy. Astron. Soc.* **375**, 1399–1408 (2007). `astro-ph/0606483`.

[144] Biermann, P. L. & Kusenko, A. Relic keV sterile neutrinos and reion-

ization. *Phys. Rev. Lett.* **96**, 091301 (2006). `astro-ph/0601004`.

[145] Kusenko, A. Sterile dark matter and reionization (2006). `astro-ph/0609375`.

[146] Mapelli, M., Ferrara, A. & Pierpaoli, E. Impact of dark matter decays and annihilations on reionization. *Mon. Not. Roy. Astron. Soc.* **369**, 1719–1724 (2006). `astro-ph/0603237`.

[147] Ripamonti, E., Mapelli, M. & Ferrara, A. Intergalactic medium heating by dark matter. *Mon. Not. Roy. Astron. Soc.* **374**, 1067–1077 (2007). `astro-ph/0606482`.

[148] Viel, M., Schaye, J. & Booth, C. M. The impact of feedback from galaxy formation on the Lyman-alpha transmitted flux (2012). `1207.6567`.

[149] Viel, M., Markovic, K., Baldi, M. & Weller, J. The Non-Linear Matter Power Spectrum in Warm Dark Matter Cosmologies. MNRAS (2011). `1107.4094`.

[150] Smith, R. E. & Markovic, K. Testing the Warm Dark Matter paradigm with large-scale structures. *Phys. Rev.* **D84**, 063507 (2011). `1103.2134`.

[151] Markovic, K., Bridle, S., Slosar, A. & Weller, J. Constraining warm dark matter with cosmic shear power spectra. *JCAP* **1101**, 022 (2011). `1009.0218`.

[152] Miranda, M. & Macciò, A. V. Constraining Warm Dark Matter using QSO gravitational lensing **706** (2007). `0706.0896`.

[153] Dunstan, R. M., Abazajian, K. N., Polisensky, E. & Ricotti, M. The Halo Model of Large Scale Structure for Warm Dark Matter (2011). `1109.6291`.

[154] Polisensky, E. & Ricotti, M. Constraints on the Dark Matter Particle Mass from the Number of Milky Way Satellites. *Phys. Rev.* **D83**, 043506 (2011). `1004.1459`.

[155] Macciò, A. V. & Fontanot, F. How cold is dark matter? Constraints from Milky Way satellites. MNRAS **404**, L16–L20 (2010). `0910.2460`.

[156] Macciò, A. V., Paduroiu, S., Anderhalden, D., Schneider, A. & Moore, B. Cores in warm dark matter haloes: a Catch 22 problem. MNRAS

424, 1105–1112 (2012). `1202.1282`.

[157] Shao, S., Gao, L., Theuns, T. & Frenk, C. S. The phase space density of fermionic dark matter haloes (2012). `1209.5563`.

[158] Vernet, J. *et al.* X-shooter, the new wide band intermediate resolution spectrograph at the ESO Very Large Telescope. A&A **536**, A105 (2011). `1110.1944`.

[159] Semboloni, E., Hoekstra, H., Schaye, J., van Daalen, M. P. & McCarthy, I. J. Quantifying the effect of baryon physics on weak lensing tomography. MNRAS **417**, 2020–2035 (2011). `1105.1075`.

[160] van Daalen, M. P., Schaye, J., Booth, C. M. & Vecchia, C. D. The effects of galaxy formation on the matter power spectrum: A challenge for precision cosmology. *Mon. Not. Roy. Astron. Soc.* **415**, 3649–3665 (2011). `1104.1174`.

[161] Maccio', A. V., Ruchayskiy, O., Boyarsky, A. & Munoz-Cuartas, J. C. The inner structure of haloes in Cold+Warm dark matter models. MNRAS (2012). `1202.2858`.

[162] Mandelbaum, R., Seljak, U. & Hirata, C. M. Halo mass - concentration relation from weak lensing. *JCAP* **0808**, 006 (2008). `0805.2552`.

[163] King, L. J. & Mead, J. M. G. The mass-concentration relationship of virialized haloes and its impact on cosmological observables. MNRAS **416**, 2539–2549 (2011). `1105.3155`.

[164] Bilic, N. & Viollier, R. D. Gravitational phase transition of fermionic matter. *Phys. Lett. B* **408**, 75–80 (1997). `arXiv:astro-ph/9607077`.

[165] Viollier, R. D. Neutrino halos around baryonic stars and supermassive neutrino stars - Atoms of the macrocosm? *Progress in Particle and Nuclear Physics* **32**, 51–74 (1994).

[166] Martin, N. F., de Jong, J. T. A. & Rix, H.-W. A Comprehensive Maximum Likelihood Analysis of the Structural Properties of Faint Milky Way Satellites. ApJ **684**, 1075–1092 (2008). `0805.2945`.

[167] Kuhlen, M., Diemand, J. & Madau, P. The Shapes, Orientation, and Alignment of Galactic Dark Matter Subhalos. ApJ **671**, 1135–1146 (2007). `0705.2037`.

[168] Tremaine, S., Henon, M. & Lynden-Bell, D. H-functions and mixing in violent relaxation. MNRAS **219**, 285–297 (1986).

[169] Cowsik, R. & Ghosh, P. Dark matter in the universe - Massive neutrinos revisited. ApJ **317**, 26–51 (1987).

[170] Madsen, J. & Epstein, R. I. Firm bounds on the neutrino mass from the distribution of dark matter in galaxies. ApJ **282**, 11–18 (1984).

[171] Madsen, J. Dark matter phase space densities. Phys. Rev. D **64**, 027301–+ (2001). `arXiv:astro-ph/0006074`.

[172] Boyanovsky, D., de Vega, H. J. & Sanchez, N. G. Constraints on dark matter particles from theory, galaxy observations, and N-body simulations. Phys. Rev. D **77**, 043518–+ (2008). `arXiv:0710.5180`.

[173] Gorbunov, D., Khmelnitsky, A. & Rubakov, V. Constraining sterile neutrino dark matter by phase-space density observations. *JCAP* **0810**, 041 (2008). `0808.3910`.

[174] Binney, J. & Tremaine, S. *Galactic Dynamics: Second Edition* (Galactic Dynamics: Second Edition, by James Binney and Scott Tremaine. ISBN 978-0-691-13026-2 (HB). Published by Princeton University Press, Princeton, NJ USA, 2008., 2008).

[175] Hogan, C. J. & Dalcanton, J. J. New dark matter physics: Clues from halo structure. Phys. Rev. D **62**, 063511–+ (2000). `arXiv:astro-ph/0002330`.

[176] Dalcanton, J. J. & Hogan, C. J. Halo cores and phase space densities: Observational constraints on dark matter physics and structure formation. ApJ **561**, 35–45 (2001). `astro-ph/0004381`.

[177] Hansen, S. H., Egli, D., Hollenstein, L. & Salzmann, C. Dark matter distribution function from non-extensive statistical mechanics. *New Astronomy* **10**, 379–384 (2005). `arXiv:astro-ph/0407111`.

[178] Bolz, M., Brandenburg, A. & Buchmuller, W. Thermal production of gravitinos. *Nucl.Phys.* *B* **606**, 518–544 (2001). `hep-ph/0012052`.

[179] Rychkov, V. S. & Strumia, A. Thermal production of gravitinos. *Phys. Rev.* **D75**, 075011 (2007). `hep-ph/0701104`.

[180] Borgani, S., Masiero, A. & Yamaguchi, M. Light gravitinos as mixed

dark matter. *Phys. Lett.* **B386**, 189–197 (1996). `hep-ph/9605222`.

[181] Antonov, V. A. *Solution of the problem of stability of stellar system Emden's density law and the spherical distribution of velocities* (Vestnik Leningradskogo Universiteta, Leningrad: University, 1962, 1962).

[182] Lynden-Bell, D. & Wood, R. The gravo-thermal catastrophe in isothermal spheres and the onset of red-giant structure for stellar systems. MNRAS **138**, 495–+ (1968).

[183] Pryor, C. & Kormendy, J. The dark matter halos of Draco and Ursa Minor. AJ **100**, 127–140 (1990).

[184] Cole, S. & Lacey, C. The structure of dark matter haloes in hierarchical clustering models. MNRAS **281**, 716 (1996). `arXiv:astro-ph/9510147`.

[185] Carlberg, R. G. *et al.* The Average Mass Profile of Galaxy Clusters. ApJ **485**, L13+ (1997). `arXiv:astro-ph/9703107`.

[186] Hansen, S. H. & Moore, B. A universal density slope Velocity anisotropy relation for relaxed structures. *New Astronomy* **11**, 333–338 (2006).

[187] Zait, A., Hoffman, Y. & Shlosman, I. Dark Matter Halos: Velocity Anisotropy-Density Slope Relation. ApJ **682**, 835–840 (2008). `0711.3791`.

[188] Van Hese, E., Baes, M. & Dejonghe, H. The Dynamical Structure of Dark Matter Halos with Universal Properties. ApJ **690**, 1280–1291 (2009). `0809.0901`.

[189] An, J. H. & Evans, N. W. A Cusp Slope-Central Anisotropy Theorem. ApJ **642**, 752–758 (2006). `arXiv:astro-ph/0511686`.

[190] Evans, N. W., An, J. & Walker, M. G. Cores and cusps in the dwarf spheroidals. MNRAS **393**, L50–L54 (2009). `0811.1488`.

[191] Strigari, L. E. *et al.* The Most Dark-Matter-dominated Galaxies: Predicted Gamma-Ray Signals from the Faintest Milky Way Dwarfs. ApJ **678**, 614–620 (2008). `arXiv:0709.1510`.

[192] Strigari, L. E. *et al.* Redefining the Missing Satellites Problem. ApJ **669**, 676–683 (2008). `0704.1817`.

[193] Wu, X. The mass distribution of dwarf spheroidal galaxies from stellar kinematics: Draco, Ursa Minor and Fornax (2007). `astro-ph/0702233`.

[194] Klypin, A., Zhao, H. & Somerville, R. S. ΛCDM-based Models for the Milky Way and M31. I. Dynamical Models. ApJ **573**, 597–613 (2002). `astro-ph/0110390`.

[195] Battaglia, G. *et al*. The radial velocity dispersion profile of the Galactic halo: constraining the density profile of the dark halo of the Milky Way. MNRAS **364**, 433–442 (2005). `arXiv:astro-ph/0506102`.

[196] Walker, M. G. *et al*. A Universal Mass Profile for Dwarf Spheroidal Galaxies? ApJ **704**, 1274–1287 (2009). `0906.0341`.

[197] Widrow, L. M. & Dubinski, J. Equilibrium Disk-Bulge-Halo Models for the Milky Way and Andromeda Galaxies. ApJ **631**, 838–855 (2005). `arXiv:astro-ph/0506177`.

[198] Gastaldello, F. *et al*. Probing the Dark Matter and Gas Fraction in Relaxed Galaxy Groups with X-Ray Observations from Chandra and XMM-Newton. ApJ **669**, 158–183 (2007). `arXiv:astro-ph/0610134`.

[199] Mateo, M., Hurley-Keller, D. & Nemec, J. Dwarf Cepheids in the Carina Dwarf Spheroidal Galaxy. AJ **115**, 1856–1868 (1998). `arXiv:astro-ph/9807233`.

[200] Belokurov, V. *et al*. Cats and Dogs, Hair and a Hero: A Quintet of New Milky Way Companions. ApJ **654**, 897–906 (2007). `arXiv:astro-ph/0608448`.

[201] Koposov, S. *et al*. The Luminosity Function of the Milky Way Satellites. ApJ **663**, 948 (2007). `0706.2687`.

[202] Irwin, M. J. *et al*. Discovery of an Unusual Dwarf Galaxy in the Outskirts of the Milky Way. ApJ **656**, L13–L16 (2007). `arXiv:astro-ph/0701154`.

[203] Zucker, D. B. *et al*. A Curious Milky Way Satellite in Ursa Major. ApJ **650**, L41–L44 (2006). `arXiv:astro-ph/0606633`.

[204] Belokurov, V. *et al*. A Faint New Milky Way Satellite in Bootes. ApJ **647**, L111–L114 (2006). `arXiv:astro-ph/0604355`.

[205] Gilmore, G. Dark Matter on small scales; Telescopes on large scales. *ArXiv Astrophysics e-prints* (2007). `arXiv:astro-ph/0703370`.

[206] Simon, J. D. & Geha, M. The Kinematics of the Ultra-Faint Milky Way Satellites: Solving the Missing Satellite Problem. ApJ **670**, 313–331 (2007). `arXiv:0706.0516`.

[207] Mateo, M., Olszewski, E., Welch, D. L., Fischer, P. & Kunkel, W. A kinematic study of the Fornax dwarf spheroidal galaxy. AJ **102**, 914–926 (1991).

[208] Bonanos, A. Z., Stanek, K. Z., Szentgyorgyi, A. H., Sasselov, D. D. & Bakos, G. Á. The RR Lyrae Distance to the Draco Dwarf Spheroidal Galaxy. AJ **127**, 861–867 (2004). `arXiv:astro-ph/0310477`.

[209] Dall'Ora, M. *et al.* Variable Stars in the Newly Discovered Milky Way Satellite in Bootes. ApJ **653**, L109–L112 (2006). `arXiv:astro-ph/0611285`.

[210] Coleman, M. G. *et al.* The Elongated Structure of the Hercules Dwarf Spheroidal Galaxy from Deep Large Binocular Telescope Imaging. ApJ **668**, L43–L46 (2007).

[211] de Jong, J. T. A. *et al.* The Structural Properties and Star Formation History of Leo T from Deep LBT Photometry. ApJ **680**, 1112–1119 (2008). `arXiv:0801.4027`.

[212] Okamoto, S., Arimoto, N., Yamada, Y. & Onodera, M. A Suprime-Cam study of the stellar population of the Ursa Major I dwarf spheroidal galaxy. A&A **487**, 103–108 (2008). `0804.2976`.

[213] Lee, M. G. *et al.* Deep Wide-Field BVI CCD Photometry of the Sextans Dwarf Spheroidal Galaxy. AJ **126**, 2840–2866 (2003).

[214] Rizzi, L., Held, E. V., Saviane, I., Tully, R. B. & Gullieuszik, M. The distance to the Fornax dwarf spheroidal galaxy. MNRAS **380**, 1255–1260 (2007). `arXiv:0707.0521`.

[215] Bellazzini, M., Gennari, N., Ferraro, F. R. & Sollima, A. The distance to the Leo I dwarf spheroidal galaxy from the red giant branch tip. MNRAS **354**, 708–712 (2004). `arXiv:astro-ph/0407444`.

[216] Bellazzini, M., Gennari, N. & Ferraro, F. R. The red giant branch tip and bump of the Leo II dwarf spheroidal galaxy. MNRAS **360**, 185–

193 (2005). `arXiv:astro-ph/0503418`.

[217] Pietrzyński, G. *et al.* The Araucaria Project: the Distance to the Sculptor Dwarf Spheroidal Galaxy from Infrared Photometry of RR Lyrae Stars. AJ **135**, 1993–1997 (2008). `arXiv:0804.0347`.

[218] Landau, L. D. & Lifshitz, E. M. *The classical theory of fields* (Course of theoretical physics - Pergamon International Library of Science, Technology, Engineering and Social Studies, Oxford: Pergamon Press, 1975, 4th rev.engl.ed., 1975).

[219] Muñoz, R. R. *et al.* Exploring Halo Substructure with Giant Stars: The Dynamics and Metallicity of the Dwarf Spheroidal in Boötes. ApJ **650**, L51–L54 (2006). `arXiv:astro-ph/0606271`.

[220] Spergel, D. N. *et al.* Three-Year Wilkinson Microwave Anisotropy Probe (WMAP) Observations: Implications for Cosmology. ApJS **170**, 377–408 (2007). `arXiv:astro-ph/0603449`.

[221] Boyarsky, A., Neronov, A., Ruchayskiy, O. & Shaposhnikov, M. Constraints on sterile neutrinos as dark matter candidates from the diffuse X-ray background. MNRAS **370**, 213–218 (2006). `arXiv:astro-ph/0512509`.

[222] Boyarsky, A., Neronov, A., Ruchayskiy, O. & Shaposhnikov, M. Restrictions on parameters of sterile neutrino dark matter from observations of galaxy clusters. Phys. Rev. D **74**, 103506 (2006). `arXiv:astro-ph/0603368`.

[223] Boyarsky, A., Neronov, A., Ruchayskiy, O., Shaposhnikov, M. & Tkachev, I. Strategy for Searching for a Dark Matter Sterile Neutrino. *Physical Review Letters* **97**, 261302–+ (2006). `arXiv:astro-ph/0603660`.

[224] Riemer-Sørensen, S., Hansen, S. H. & Pedersen, K. Sterile Neutrinos in the Milky Way: Observational Constraints. ApJ **644**, L33–L36 (2006). `arXiv:astro-ph/0603661`.

[225] Watson, C. R., Beacom, J. F., Yüksel, H. & Walker, T. P. Direct x-ray constraints on sterile neutrino warm dark matter. Phys. Rev. D **74**, 033009–+ (2006). `arXiv:astro-ph/0605424`.

[226] Boyarsky, A., Ruchayskiy, O. & Markevitch, M. Constraints on Para-

meters of Radiatively Decaying Dark Matter from the Galaxy Cluster 1E 0657-56. ApJ **673**, 752–757 (2008). `arXiv:astro-ph/0611168`.

[227] Abazajian, K. N., Markevitch, M., Koushiappas, S. M. & Hickox, R. C. Limits on the Radiative Decay of Sterile Neutrino Dark Matter from the Unresolved Cosmic and Soft X-ray Backgrounds. Phys. Rev. D **75**, 063511–+ (2007). `arXiv:astro-ph/0611144`.

[228] Boyarsky, A., Nevalainen, J. & Ruchayskiy, O. Constraints on the parameters of radiatively decaying dark matter from the dark matter halos of the Milky Way and Ursa Minor. A&A **471**, 51–57 (2007). `arXiv:astro-ph/0610961`.

[229] Boyarsky, A., den Herder, J., Neronov, A. & Ruchayskiy, O. Search for the light dark matter with an X-ray spectrometer. *Astroparticle Physics* **28**, 303–311 (2007). `arXiv:astro-ph/0612219`.

[230] Boyarsky, A., Iakubovskyi, D., Ruchayskiy, O. & Savchenko, V. Constraints on decaying dark matter from XMM-Newton observations of M31. MNRAS **387**, 1361–1373 (2008). `arXiv:0709.2301`.

[231] Boyarsky, A., Malyshev, D., Neronov, A. & Ruchayskiy, O. Constraining DM properties with SPI. MNRAS **387**, 1345–1360 (2008). `0710. 4922`.

[232] Shaposhnikov, M. & Tkachev, I. The numsm, inflation, and dark matter. *Phys. Lett.* **B639**, 414–417 (2006). `hep-ph/0604236`.

[233] Kusenko, A. Sterile neutrinos, dark matter, and the pulsar velocities in models with a higgs singlet. *Phys. Rev. Lett.* **97**, 241301 (2006). `hep-ph/0609081`.

[234] Petraki, K. & Kusenko, A. Dark-matter sterile neutrinos in models with a gauge singlet in the Higgs sector. *Phys. Rev.* **D77**, 065014 (2008). `0711.4646`.

[235] Petraki, K. Small-scale structure formation properties of chilled sterile neutrinos as dark matter. Phys. Rev. D **77**, 105004–+ (2008). `arXiv:0801.3470`.

[236] Gorbunov, D., Khmelnitsky, A. & Rubakov, V. Is gravitino still a warm dark matter candidate? (2008). `0805.2836`.

[237] Boyanovsky, D. Clustering properties of a sterile neutrino dark matter

candidate. *Phys. Rev.* **D78**, 103505 (2008). `0807.0646`.

[238] Blumenthal, G. R., Faber, S. M., Flores, R. & Primack, J. R. Contraction of dark matter galactic halos due to baryonic infall. ApJ **301**, 27–34 (1986).

[239] Gnedin, O. Y., Kravtsov, A. V., Klypin, A. A. & Nagai, D. Response of Dark Matter Halos to Condensation of Baryons: Cosmological Simulations and Improved Adiabatic Contraction Model. ApJ **616**, 16–26 (2004). `arXiv:astro-ph/0406247`.

[240] Lin, D. N. C. & Faber, S. M. Some implications of nonluminous matter in dwarf spheroidal galaxies. ApJ **266**, L21–L25 (1983).

[241] Moore, B. Evidence against Dissipationless Dark Matter from Observations of Galaxy Haloes. Nature **370**, 629–+ (1994).

[242] Mastropietro, C. *et al.* Morphological evolution of discs in clusters. MNRAS **364**, 607–619 (2005). `arXiv:astro-ph/0411648`.

[243] Mayer, L., Mastropietro, C., Wadsley, J., Stadel, J. & Moore, B. Simultaneous ram pressure and tidal stripping; how dwarf spheroidals lost their gas. MNRAS **369**, 1021–1038 (2006). `arXiv:astro-ph/0504277`.

[244] Mayer, L., Kazantzidis, S., Mastropietro, C. & Wadsley, J. Early gas stripping as the origin of the darkest galaxies in the Universe. Nature **445**, 738–740 (2007). `arXiv:astro-ph/0702495`.

[245] Read, A. M., Sembay, S. F., Abbey, T. F. & Turner, M. J. L. 'Patching' EPIC-MOS: Temporal and Spatial Dependency of the Detector Response. In A. Wilson (ed.) *The X-ray Universe 2005*, vol. 604 of *ESA Special Publication*, 925 (2006).

[246] Naab, T., Johansson, P. H., Ostriker, J. P. & Efstathiou, G. Formation of Early-Type Galaxies from Cosmological Initial Conditions. ApJ **658**, 710–720 (2007). `arXiv:astro-ph/0512235`.

[247] Kormendy, J. & Freeman, K. C. Scaling Laws for Dark Matter Halos in Late-Type and Dwarf Spheroidal Galaxies. In Ryder, S., Pisano, D., Walker, M. & Freeman, K. (eds.) *Dark Matter in Galaxies*, vol. 220 of *IAU Symposium*, 377 (2004). `arXiv:astro-ph/0407321`.

[248] Donato, F. *et al.* A constant dark matter halo surface density in galax-

ies. MNRAS **397**, 1169–1176 (2009). `0904.4054`.

[249] Gentile, G., Famaey, B., Zhao, H. & Salucci, P. Universality of galactic surface densities within one dark halo scale-length. Nature **461**, 627–628 (2009). `0909.5203`.

[250] Bardeau, S. *et al.* A CFH12k lensing survey of X-ray luminous galaxy clusters. II. Weak lensing analysis and global correlations. A&A **470**, 449–466 (2007). `arXiv:astro-ph/0703395`.

[251] Broadhurst, T., Umetsu, K., Medezinski, E., Oguri, M. & Rephaeli, Y. Comparison of Cluster Lensing Profiles with ΛCDM Predictions. ApJ **685**, L9–L12 (2008). `0805.2617`.

[252] Comerford, J. M. & Natarajan, P. The observed concentration-mass relation for galaxy clusters. MNRAS **379**, 190–200 (2007). `arXiv: astro-ph/0703126`.

[253] Corless, V. L., King, L. J. & Clowe, D. A new look at massive clusters: weak lensing constraints on the triaxial dark matter haloes of A1689, A1835 and A2204. MNRAS **393**, 1235–1254 (2009). `0812.0632`.

[254] Donnarumma, A., Ettori, S., Meneghetti, M. & Moscardini, L. X-ray and strong lensing mass estimate of MS2137.3-2353. MNRAS **398**, 438–450 (2009). `0902.4051`.

[255] Ettori, S., De Grandi, S. & Molendi, S. Gravitating mass profiles of nearby galaxy clusters and relations with X-ray gas temperature, luminosity and mass. A&A **391**, 841–855 (2002). `arXiv:astro-ph/ 0206120`.

[256] Gavazzi, R. *et al.* A weak lensing study of the Coma cluster. A&A **498**, L33–L36 (2009). `0904.0220`.

[257] Kubo, J. M. *et al.* The Mass of the Coma Cluster from Weak Lensing in the Sloan Digital Sky Survey. ApJ **671**, 1466–1470 (2007). `0709. 0506`.

[258] McLaughlin, D. E. Evidence in Virgo for the Universal Dark Matter Halo. ApJ **512**, L9–L12 (1999). `arXiv:astro-ph/9812242`.

[259] Rines, K., Geller, M. J., Kurtz, M. J. & Diaferio, A. CAIRNS: The Cluster and Infall Region Nearby Survey. I. Redshifts and Mass Profiles. AJ **126**, 2152–2170 (2003). `arXiv:astro-ph/0306538`.

[260] Schmidt, R. W. & Allen, S. W. The dark matter haloes of massive, relaxed galaxy clusters observed with Chandra. MNRAS **379**, 209–221 (2007). `arXiv:astro-ph/0610038`.

[261] Sereno, M., Lubini, M. & Jetzer, P. A multiwavelength strong lensing analysis of baryons and dark matter in the dynamically active cluster AC 114. A&A **518**, A55 (2010). `0904.0018`.

[262] Umetsu, K. & Broadhurst, T. Combining Lens Distortion and Depletion to Map the Mass Distribution of A1689. ApJ **684**, 177–203 (2008). `0712.3441`.

[263] `http://sites.google.com/site/dima806/clusters.pdf`.

[264] Romanowsky, A. J. *et al.* Mapping The Dark Side with DEIMOS: Globular Clusters, X-Ray Gas, and Dark Matter in the NGC 1407 Group. AJ **137**, 4956–4987 (2009). `0809.2088`.

[265] Sun, M. *et al.* Chandra Studies of the X-Ray Gas Properties of Galaxy Groups. ApJ **693**, 1142–1172 (2009). `0805.2320`.

[266] `http://sites.google.com/site/dima806/groups.pdf`.

[267] Humphrey, P. J. *et al.* A Chandra View of Dark Matter in Early-Type Galaxies. ApJ **646**, 899–918 (2006). `arXiv:astro-ph/0601301`.

[268] Weijmans, A.-M. *et al.* The shape of the dark matter halo in the early-type galaxy NGC 2974. MNRAS **383**, 1343–1358 (2008). `0711.1775`.

[269] Weijmans, A. *et al.* Stellar velocity profiles and line strengths out to four effective radii in the early-type galaxies NGC3379 and 821. MNRAS **398**, 561–574 (2009). `0906.0018`.

[270] Napolitano, N. R. *et al.* The Planetary Nebula Spectrograph elliptical galaxy survey: the dark matter in NGC 4494. MNRAS **393**, 329–353 (2009). `0810.1291`.

[271] Zhang, Z. *et al.* Probing the Mass Distributions in NGC 1407 and Its Associated Group with the X-Ray Imaging Spectroscopic and Optical Photometric and Line-Strength Indices Data. ApJ **656**, 805–817 (2007). `arXiv:astro-ph/0610934`.

[272] `http://sites.google.com/site/dima806/ellipticals.pdf`.

[273] Athanassoula, E., Bosma, A. & Papaioannou, S. Halo parameters of

spiral galaxies. A&A **179**, 23–40 (1987).

[274] Begeman, K. G., Broeils, A. H. & Sanders, R. H.   Extended rotation curves of spiral galaxies - Dark haloes and modified dynamics. MNRAS **249**, 523–537 (1991).

[275] Begum, A. & Chengalur, J. N. Kinematics of two dwarf galaxies in the NGC 6946 group. A&A **424**, 509–517 (2004).

[276] Blais-Ouellette, S., Carignan, C., Amram, P. & Côté, S.   Accurate Parameters of the Mass Distribution in Spiral Galaxies. I. Fabry-Perot Observations of NGC 5585. AJ **118**, 2123–2131 (1999). `arXiv: astro-ph/9911223`.

[277] de Blok, W. J. G. & Bosma, A.   High-resolution rotation curves of low surface brightness galaxies. A&A **385**, 816–846 (2002). `arXiv: astro-ph/0201276`.

[278] de Blok, W. J. G. *et al*. High-Resolution Rotation Curves and Galaxy Mass Models from THINGS. AJ **136**, 2648–2719 (2008). `0810.2100`.

[279] de Blok, W. J. G. & McGaugh, S. S. The dark and visible matter content of low surface brightness disc galaxies. MNRAS **290**, 533–552 (1997). `arXiv:astro-ph/9704274`.

[280] van den Bosch, F. C. & Swaters, R. A. Dwarf galaxy rotation curves and the core problem of dark matter haloes. MNRAS **325**, 1017–1038 (2001). `arXiv:astro-ph/0006048`.

[281] Chemin, L., Carignan, C., Drouin, N. & Freeman, K. C. H I Studies of the Sculptor Group Galaxies. VIII. The Background Galaxies: NGC 24 and NGC 45. AJ **132**, 2527–2538 (2006). `arXiv:astro-ph/0609148`.

[282] Côté, S., Carignan, C. & Freeman, K. C. The Various Kinematics of Dwarf Irregular Galaxies in Nearby Groups and Their Dark Matter Distributions. AJ **120**, 3027–3059 (2000).

[283] Côté, S., Carignan, C. & Sancisi, R. A dark-halo-dominated galaxy - NGC 5585. AJ **102**, 904–913 (1991).

[284] Dutton, A. A., Courteau, S., de Jong, R. & Carignan, C. Mass Modeling of Disk Galaxies: Degeneracies, Constraints, and Adiabatic Contraction. ApJ **619**, 218–242 (2005). `arXiv:astro-ph/0310001`.

[285] Geehan, J. J., Fardal, M. A., Babul, A. & Guhathakurta, P. Investigating the Andromeda stream - I. Simple analytic bulge-disc-halo model for M31. MNRAS **366**, 996–1011 (2006). `arXiv:astro-ph/0501240`.

[286] Gentile, G., Salucci, P., Klein, U., Vergani, D. & Kalberla, P. The cored distribution of dark matter in spiral galaxies. MNRAS **351**, 903–922 (2004). `arXiv:astro-ph/0403154`.

[287] Kent, S. M. Dark matter in spiral galaxies. I - Galaxies with optical rotation curves. AJ **91**, 1301–1327 (1986).

[288] Kent, S. M. Dark matter in spiral galaxies. II - Galaxies with H I rotation curves. AJ **93**, 816–832 (1987).

[289] Lake, G. & Feinswog, L. The distribution of dark matter in galaxies. I - Models of spiral galaxies. AJ **98**, 166–179 (1989).

[290] Lake, G., Schommer, R. A. & van Gorkom, J. H. The distribution of dark matter in the dwarf galaxy DDO 170. AJ **99**, 547–560 (1990).

[291] Marchesini, D. *et al*. Hα Rotation Curves: The Soft Core Question. ApJ **575**, 801–813 (2002). `arXiv:astro-ph/0202075`.

[292] Kuzio de Naray, R., McGaugh, S. S., de Blok, W. J. G. & Bosma, A. High-Resolution Optical Velocity Fields of 11 Low Surface Brightness Galaxies. ApJS **165**, 461–479 (2006). `arXiv:astro-ph/0604576`.

[293] Kuzio de Naray, R., McGaugh, S. S. & de Blok, W. J. G. Mass Models for Low Surface Brightness Galaxies with High-Resolution Optical Velocity Fields. ApJ **676**, 920–943 (2008). `0712.0860`.

[294] Puche, D. & Carignan, C. H I studies of the Sculptor group galaxies. VII - Implications on the distribution and nature of dark matter in groups. ApJ **378**, 487–495 (1991).

[295] Sicotte, V. & Carignan, C. NGC 5204: A Strongly Warped Magellanic Spiral.II.H I Kinematics and Mass Distribution. AJ **113**, 609–617 (1997).

[296] Spano, M. *et al*. GHASP: an Hα kinematic survey of spiral and irregular galaxies - V. Dark matter distribution in 36 nearby spiral galaxies. MNRAS **383**, 297–316 (2008). `0710.1345`.

[297] Swaters, R. A., Madore, B. F., van den Bosch, F. C. & Balcells, M.

The Central Mass Distribution in Dwarf and Low Surface Brightness Galaxies. ApJ **583**, 732–751 (2003). `arXiv:astro-ph/0210152`.

[298] Tempel, E., Tamm, A. & Tenjes, P. Visible and dark matter in M 31 - II. A dynamical model and dark matter density distribution. *ArXiv e-prints* (2007). `0707.4374`.

[299] Weldrake, D. T. F., de Blok, W. J. G. & Walter, F. A high-resolution rotation curve of NGC 6822: a test-case for cold dark matter. MNRAS **340**, 12–28 (2003). `arXiv:astro-ph/0210568`.

[300] Frigerio Martins, C. The distribution of the dark matter in galaxies as the imprint of its Nature. *ArXiv e-prints* (2009). `0903.4588`.

[301] `http://sites.google.com/site/dima806/spirals.pdf`.

[302] van Eymeren, J., Trachternach, C., Koribalski, B. S. & Dettmar, R. Non-circular motions and the cusp-core discrepancy in dwarf galaxies. A&A **505**, 1–20 (2009). `0906.4654`.

[303] `http://sites.google.com/site/dima806/dwarves.pdf`.

[304] Navarro, J. F., Frenk, C. S. & White, S. D. M. The Structure of Cold Dark Matter Halos. ApJ **462**, 563–+ (1996). `arXiv:astro-ph/9508025`.

[305] Navarro, J. F., Frenk, C. S. & White, S. D. M. A Universal Density Profile from Hierarchical Clustering. ApJ **490**, 493–+ (1997). `arXiv:astro-ph/9611107`.

[306] Burkert, A. The Structure of Dark Matter Halos in Dwarf Galaxies. ApJ **447**, L25+ (1995). `arXiv:astro-ph/9504041`.

[307] Macciò, A. V., Dutton, A. A. & van den Bosch, F. C. Concentration, spin and shape of dark matter haloes as a function of the cosmological model: WMAP1, WMAP3 and WMAP5 results. MNRAS **391**, 1940–1954 (2008). `0805.1926`.

[308] Springel, V. *et al.* The Aquarius Project: the subhaloes of galactic haloes. MNRAS **391**, 1685–1711 (2008). `0809.0898`.

[309] Komatsu, E. *et al.* Five-Year Wilkinson Microwave Anisotropy Probe Observations: Cosmological Interpretation. ApJS **180**, 330–376 (2009). `0803.0547`.

[310] Neto, A. F. *et al.* The statistics of Λ CDM halo concentrations. MNRAS **381**, 1450–1462 (2007). `0706.2919`.

[311] Bullock, J. S. *et al.* Profiles of dark haloes: evolution, scatter and environment. MNRAS **321**, 559–575 (2001). `arXiv:astro-ph/9908159`.

[312] Dvali, G., Gabadadze, G. & Porrati, M. 4D gravity on a brane in 5D Minkowski space. *Physics Letters B* **485**, 208–214 (2000). `arXiv:hep-th/0005016`.

[313] Kormendy, J. & Djorgovski, S. Surface photometry and the structure of elliptical galaxies. ARA&A **27**, 235–277 (1989).

[314] Tully, R. B. & Fisher, J. R. A new method of determining distances to galaxies. A&A **54**, 661–673 (1977).

[315] Milgrom, M. A modification of the Newtonian dynamics - Implications for galaxies. ApJ **270**, 371–389 (1983).

[316] Loewenstein, M. & Kusenko, A. Dark Matter Search Using Chandra Observations of Willman 1 and a Spectral Feature Consistent with a Decay Line of a 5 keV Sterile Neutrino. ApJ **714**, 652–662 (2010). `0912.0552`.

[317] Willman, B. *et al.* A New Milky Way Dwarf Galaxy in Ursa Major. ApJ **626**, L85–L88 (2005). `arXiv:astro-ph/0503552`.

[318] Loewenstein, M., Kusenko, A. & Biermann, P. L. New Limits on Sterile Neutrinos from Suzaku Observations of the Ursa Minor Dwarf Spheroidal Galaxy. ApJ **700**, 426–435 (2009). `0812.2710`.

[319] Riemer-Sørensen, S. & Hansen, S. H. Decaying dark matter in the Draco dwarf galaxy. A&A **500**, L37–L40 (2009).

[320] Piconcelli, E. *et al.* *XMM-Newton Users Handbook, issue 2.10*. ESA: XMM-Newton SOC (2012). `http://xmm.esac.esa.int/external/xmm_user_support/documentation/uhb`.

[321] Monte carlo methods for including correlated systematic calibration uncertainties in astrophysical analysis: Chandra acis. `http://cxc.harvard.edu/ccr/proceedings/07_proc/presentations/drake/`.

[322] Kerins, E. *et al.* Theory of pixel lensing towards M31 - I. The dens-

ity contribution and mass of MACHOs. MNRAS **323**, 13–33 (2001). `arXiv:astro-ph/0002256`.

[323] Boyarsky, A. *et al*. Searching for dark matter in X-rays: how to check the dark matter origin of a spectral feature. MNRAS **407**, 1188–1202 (2010). `1001.0644`.

[324] Dealing with epic out-of-time (oot) events. `http://xmm.esa.int/sas/current/documentation/threads/EPIC_OoT.shtml`.

[325] Read, A. M. & Ponman, T. J. The XMM-Newton EPIC background: Production of background maps and event files. A&A **409**, 395–410 (2003). `arXiv:astro-ph/0304147`.

[326] Nevalainen, J., Markevitch, M. & Lumb, D. XMM-Newton EPIC Background Modeling for Extended Sources. ApJ **629**, 172–191 (2005). `arXiv:astro-ph/0504362`.

[327] Carter, J. A. & Read, A. M. The XMM-Newton EPIC background and the production of background blank sky event files. A&A **464**, 1155–1166 (2007). `arXiv:astro-ph/0701209`.

[328] Leccardi, A. & Molendi, S. Radial temperature profiles for a large sample of galaxy clusters observed with XMM-Newton. A&A **486**, 359–373 (2008). `0804.1909`.

[329] Kuntz, K. D. & Snowden, S. L. The EPIC-MOS particle-induced background spectra. A&A **478**, 575–596 (2008).

[330] De Luca, A. & Molendi, S. The 2-8 keV cosmic X-ray background spectrum as observed with XMM-Newton. A&A **419**, 837–848 (2004). `arXiv:astro-ph/0311538`.

[331] Fin_over_fout public script, v. 1.1. `http://xmm.vilspa.esa.es/external/xmm_sw_cal/background/Fin_over_Fout`.

[332] Repository of xmm-newton epic filter wheel closed (fwc) data. `http://xmm2.esac.esa.int/external/xmm_sw_cal/background/filter_closed/index.shtml`.

[333] The ftools webpage. `http://heasarc.gsfc.nasa.gov/docs/software/ftools/ftools_menu.html`.

[334] Lumb, D. H., Warwick, R. S., Page, M. & De Luca, A. X-ray background

measurements with XMM-Newton EPIC. A&A **389**, 93–105 (2002). `arXiv:astro-ph/0204147`.

[335] Hickox, R. C. & Markevitch, M. Absolute Measurement of the Unresolved Cosmic X-Ray Background in the 0.5-8 keV Band with Chandra. ApJ **645**, 95–114 (2006). `astro-ph/0512542`.

[336] Moretti, A. *et al.* A new measurement of the cosmic X-ray background. A&A **493**, 501–509 (2009). `0811.1444`.

[337] Mateos, S., Saxton, R. D., Read, A. M. & Sembay, S. Statistical evaluation of the flux cross-calibration of the XMM-Newton EPIC cameras. A&A **496**, 879–889 (2009). `0901.4026`.

[338] Carter, J. A., Sembay, S. & Read, A. M. A high charge state coronal mass ejection seen through solar wind charge exchange emission as detected by XMM-Newton. MNRAS **402**, 867–878 (2010). `0911.0897`.

[339] Guainazzi, M. *et al.* Epic status of calibration and data analysis. XMM-Newton calibration technical report, EPIC Concortium (2012). `http://xmm2.esac.esa.int/docs/documents/CAL-TN-0018.ps.gz`.

[340] Kirsch, M. G. F. *et al.* XMM-Newton (cross)-calibration. In G. Hasinger & M. J. L. Turner (ed.) *Society of Photo-Optical Instrumentation Engineers (SPIE) Conference Series*, vol. 5488 of *Presented at the Society of Photo-Optical Instrumentation Engineers (SPIE) Conference*, 103–114 (2004). `astro-ph/0407257`.

[341] Kerins, E. The impact of spheroid stars for Macho microlensing surveys of the Andromeda Galaxy. *Mon. Not. Roy. Astron. Soc.* **347**, 1033 (2004). `astro-ph/0310537`.

[342] Kusenko, A. & Loewenstein, M. Searching for dark matter in X-rays: how not to check the dark matter origin of a spectral feature. *ArXiv e-prints* (2010). `1001.4055`.

[343] Walterbos, R. A. M. & Kennicutt, R. C., Jr. Multi-color photographic surface photometry of the Andromeda galaxy. A&AS **69**, 311–332 (1987).

[344] Walterbos, R. A. M. & Kennicutt, R. C., Jr. An optical study of stars and dust in the Andromeda galaxy. A&A **198**, 61–86 (1988).

[345] Bell, E. F., McIntosh, D. H., Katz, N. & Weinberg, M. D. The Optical and Near-Infrared Properties of Galaxies. I. Luminosity and Stellar Mass Functions. ApJS **149**, 289–312 (2003). `arXiv:astro-ph/0302543`.

[346] Bell, E. F. & de Jong, R. S. Stellar Mass-to-Light Ratios and the Tully-Fisher Relation. ApJ **550**, 212–229 (2001). `arXiv:astro-ph/0011493`.

[347] Seigar, M. S., Barth, A. J. & Bullock, J. S. A revised Λ CDM mass model for the Andromeda Galaxy. MNRAS **389**, 1911–1923 (2008). `arXiv:astro-ph/0612228`.

[348] Stanek, K. Z. & Garnavich, P. M. Distance to M31 with the Hubble Space Telescope and HIPPARCOS Red Clump Stars. ApJ **503**, L131+ (1998). `arXiv:astro-ph/9802121`.

[349] Walker, M. G., Mateo, M. & Olszewski, E. W. Stellar Velocities in the Carina, Fornax, Sculptor, and Sextans dSph Galaxies: Data From the Magellan/MMFS Survey. AJ **137**, 3100–3108 (2009). `0811.0118`.

[350] Martin, N. F., Ibata, R. A., Chapman, S. C., Irwin, M. & Lewis, G. F. A Keck/DEIMOS spectroscopic survey of faint Galactic satellites: searching for the least massive dwarf galaxies. MNRAS **380**, 281–300 (2007). `arXiv:0705.4622`.

[351] Jeltema, T. E. & Profumo, S. Searching for Dark Matter with X-ray Observations of Local Dwarf Galaxies. ApJ **686**, 1045–1055 (2008). `0805.1054`.

[352] Xmm-newton epic background components. `http://www.star.le.ac.uk/~amr30/BG/BGTable.html`.

[353] Pradas, J. & Kerp, J. XMM-Newton data processing for faint diffuse emission. Proton flares, exposure maps and report on EPIC MOS1 bright CCDs contamination. A&A **443**, 721–733 (2005). `arXiv:astro-ph/0508137`.

[354] Mirabal, N. & Nieto, D. Willman 1 in X-rays: Can you tell a dwarf galaxy from a globular cluster? *ArXiv e-prints* (2010). `1003.3745`.

[355] Prokhorov, D. & Silk, J. Can the Excess in the Fe XXVI Lyγ Line from the Galactic Center Provide Evidence for 17 keV Sterile Neutrinos?

ApJ **725**, L131–L134 (2010). `1001.0215`.

[356] Koyama, K. *et al.* Iron and Nickel Line Diagnostics for the Galactic Center Diffuse Emission. PASJ **59**, 245–255 (2007). `arXiv: astro-ph/0609215`.

[357] Riemer-Sørensen, S., Pedersen, K., Hansen, S. H. & Dahle, H. Probing the nature of dark matter with cosmic x rays: Constraints from "dark blobs" and grating spectra of galaxy clusters. Phys. Rev. D **76**, 043524–+ (2007). `arXiv:astro-ph/0610034`.

[358] Abazajian, K. N., Markevitch, M., Koushiappas, S. M. & Hickox, R. C. Limits on the radiative decay of sterile neutrino dark matter from the unresolved cosmic and soft x-ray backgrounds. Phys. Rev. D **75**, 063511–+ (2007). `arXiv:astro-ph/0611144`.

[359] Yüksel, H., Beacom, J. F. & Watson, C. R. Strong Upper Limits on Sterile Neutrino Warm Dark Matter. *Physical Review Letters* **101**, 121301–+ (2008). `0706.4084`.

[360] Mirabal, N. Swift observation of Segue 1: constraints on sterile neutrino parameters in the darkest galaxy. MNRAS **409**, L128–L131 (2010). `1010.4706`.

[361] Borriello, E., Paolillo, M., Miele, G., Longo, G. & Owen, R. Constraints on sterile neutrino dark matter from XMM-Newton observations of M33. MNRAS **425**, 1628–1632 (2012). `1109.5943`.

[362] Watson, C. R., Li, Z. & Polley, N. K. Constraining sterile neutrino warm dark matter with Chandra observations of the Andromeda galaxy. JCAP **3**, 18 (2012). `1111.4217`.

[363] Loewenstein, M. & Kusenko, A. Dark Matter Search Using XMM-Newton Observations of Willman 1. ApJ **751**, 82 (2012). `1203.5229`.

[364] Combet, C. *et al.* Decaying dark matter: Stacking analysis of galaxy clusters to improve on current limits. Phys. Rev. D **85**, 063517 (2012). `1203.1164`.

[365] Piro, L. *et al.* EDGE: Explorer of diffuse emission and gamma-ray burst explosions. *Experimental Astronomy* **23**, 67–89 (2009). `0707. 4103`.

[366] Abazajian, K. Detection of Dark Matter Decay in the X-ray. In *as-*

tro2010: The Astronomy and Astrophysics Decadal Survey, vol. 2010 of *ArXiv Astrophysics e-prints*, 1–+ (2009). `0903.2040`.

[367] Boyarsky, A., Ruchayskiy, O., Iakubovskyi, D., Maccio', A. V. & Malyshev, D. New evidence for dark matter. *ArXiv e-prints* (2009). `0911.1774`.

[368] Merrifield, M. R. The rotation curve of the Milky Way to 2.5 R_0 from the thickness of the H I layer. AJ **103**, 1552–1563 (1992).

[369] Alcock, C. *et al.* The MACHO Project First-Year Large Magellanic Cloud Results: The Microlensing Rate and the Nature of the Galactic Dark Halo. ApJ **461**, 84–+ (1996). `arXiv:astro-ph/9506113`.

[370] Battaglia, G. *et al.* Erratum: The radial velocity dispersion profile of the Galactic halo: constraining the density profile of the dark halo of the Milky Way. MNRAS **370**, 1055–1056 (2006).

[371] Smith, M. C. *et al.* The RAVE survey: constraining the local Galactic escape speed. MNRAS **379**, 755–772 (2007). `arXiv:astro-ph/0611671`.

[372] Xue, X. X. *et al.* The Milky Way's Circular Velocity Curve to 60 kpc and an Estimate of the Dark Matter Halo Mass from the Kinematics of ˜2400 SDSS Blue Horizontal-Branch Stars. ApJ **684**, 1143–1158 (2008). `0801.1232`.

[373] Sofue, Y., Honma, M. & Omodaka, T. Unified Rotation Curve of the Galaxy – Decomposition into de Vaucouleurs Bulge, Disk, Dark Halo, and the 9-kpc Rotation Dip –. PASJ **61**, 227– (2009). `0811.0859`.

[374] Weber, M. & de Boer, W. Determination of the local dark matter density in our Galaxy. A&A **509**, A25 (2010). `0910.4272`.

[375] McMillan, P. J. Mass models of the Milky Way. MNRAS **414**, 2446–2457 (2011). `1102.4340`.

[376] Haberl, F., Dennerl, K. & Pietsch, W. Deep XMM-Newton observation of a northern LMC field I. Selected X-ray sources. A&A **406**, 471–481 (2003). `arXiv:astro-ph/0212319`.

[377] Stiele, H. *et al.* The deep XMM-Newton Survey of M 31. A&A **534**, A55 (2011). `1106.4755`.

[378] Haberl, F. *et al.* The XMM-Newton survey of the Small Magellanic Cloud. A&A **545**, A128 (2012). `1208.0231`.

[379] McConnachie, A. W. *et al.* Distances and metallicities for 17 Local Group galaxies. MNRAS **356**, 979–997 (2005). `arXiv:astro-ph/0410489`.

[380] Gondolo, P. Dark matter annihilations in the Large Magellanic Cloud. *Nuclear Physics B Proceedings Supplements* **35**, 148–149 (1994). `arXiv:astro-ph/9312011`.

[381] Tasitsiomi, A., Gaskins, J. & Olinto, A. V. Gamma-ray and synchrotron emission from neutralino annihilation in the Large Magellanic Cloud. *Astroparticle Physics* **21**, 637–650 (2004). `arXiv:astro-ph/0307375`.

[382] Siffert, B. B., Limone, A., Borriello, E., Longo, G. & Miele, G. Radio emission from dark matter annihilation in the Large Magellanic Cloud. MNRAS **410**, 2463–2471 (2011). `1006.5325`.

[383] van der Marel, R. P., Alves, D. R., Hardy, E. & Suntzeff, N. B. New Understanding of Large Magellanic Cloud Structure, Dynamics, and Orbit from Carbon Star Kinematics. AJ **124**, 2639–2663 (2002). `arXiv:astro-ph/0205161`.

[384] Bekki, K. & Stanimirović, S. The total mass and dark halo properties of the Small Magellanic Cloud. MNRAS **395**, 342–350 (2009). `0807.2102`.

[385] `http://sites.google.com/site/dima806/galnum.pdf`.

[386] Heasarc: Nasa's archive of data on energetic phenomena. `http://heasarc.nasa.gov`.

[387] `http://sites.google.com/site/dima806/obsnum.pdf`.

[388] Turner, M. J. L. *et al.* The European Photon Imaging Camera on XMM-Newton: The MOS cameras : The MOS cameras. A&A **365**, L27–L35 (2001). `arXiv:astro-ph/0011498`.

[389] Strüder, L. *et al.* The European Photon Imaging Camera on XMM-Newton: The pn-CCD camera. A&A **365**, L18–L26 (2001).

[390] Aschenbach, B. *et al.* Imaging performance of the XMM-Newton x-

ray telescopes. In Truemper, J. E. & Aschenbach, B. (eds.) *Society of Photo-Optical Instrumentation Engineers (SPIE) Conference Series*, vol. 4012 of *Society of Photo-Optical Instrumentation Engineers (SPIE) Conference Series*, 731–739 (2000). `arXiv:astro-ph/0007256`.

[391] de la Calle, I. *et al.* *Users Guide to the XMM-Newton Science Analysis System, issue 9.0*. ESA: XMM-Newton SOC (2012). `http://xmm.esac.esa.int/external/xmm_user_support/documentation/sas_usg/USG`.

[392] Xmm-newton science analysis system. `http://xmm.esa.int/sas/`.

[393] Description of `espfilt` task for xmm-newton science analysis system v. 11.0.0. `http://xmm.esac.esa.int/sas/11.0.0/doc/espfilt/index.html`.

[394] Abbey, T. *et al.* Micrometeroid Damage to CCDs in XMM-Newton and Swift and its Significance for Future X-ray Missions. In Wilson, A. (ed.) *The X-ray Universe 2005*, vol. 604 of *ESA Special Publication*, 943 (2006).

[395] Xmm-newton epic mos1 ccd6 update. `http://xmm.esac.esa.int/external/xmm_news/items/MOS1-CCD6/`.

[396] Epic source finding thread: edetect_chain. `http://xmm.esac.esa.int/sas/current/documentation/threads/src_find_thread.shtml`.

[397] Description of `backscale` task for xmm-newton science analysis system v. 11.0.0. `http://xmm.esac.esa.int/sas/11.0.0/doc/backscale/index.html`.

[398] Description of `evselect` task for xmm-newton science analysis system v. 11.0.0. `http://xmm.esac.esa.int/sas/11.0.0/doc/evselect/index.html`.

[399] Lumb, D. H., Berthiaume, G. D., Burrows, D. N., Garmire, G. P. & Nousek, J. A. Charge coupled devices (CCDs) in X-ray astronomy. *Experimental Astronomy* **2**, 179–201 (1991).

[400] Sembay, S. *et al.* In-orbit performance of the EPIC-MOS detectors on XMM-Newton. In G. Hasinger & M. J. L. Turner (ed.) *Society of Photo-Optical Instrumentation Engineers (SPIE) Conference Series*, vol. 5488

of *Society of Photo-Optical Instrumentation Engineers (SPIE) Conference Series*, 264–271 (2004). `arXiv:astro-ph/0407347`.

[401] Sembay, S. & Bennie, P. Mos ccd rmf description. XMM-Newton calibration technical report (2000). `http://xmm.vilspa.esa.es/docs/documents/CAL-TN-0006-1-0.ps.gz`.

[402] McCarthy, K. J., Owens, A. & Keay, A. Escape peak ratios in silicon X-ray charge coupled devices (CCDs). *Nuclear Instruments and Methods in Physics Research A* **384**, 403–409 (1997).

[403] Description of `rmfgen` task for xmm-newton science analysis system v. 11.0.0. `http://xmm.esac.esa.int/sas/11.0.0/doc/rmfgen/index.html`.

[404] Description of `arfgen` task for xmm-newton science analysis system v. 11.0.0. `http://xmm.esac.esa.int/sas/11.0.0/doc/arfgen/index.html`.

[405] Nazé, Y., Flores, C. A. & Rauw, G. A detailed X-ray investigation of ζ Puppis. I. The dataset and some preliminary results. A&A **538**, A22 (2012). `1112.0862`.

[406] Freyberg, M. J. *et al.* EPIC pn-CCD detector aboard XMM-Newton: status of the background calibration. In Flanagan, K. A. & Siegmund, O. H. W. (eds.) *Society of Photo-Optical Instrumentation Engineers (SPIE) Conference Series*, vol. 5165 of *Society of Photo-Optical Instrumentation Engineers (SPIE) Conference Series*, 112–122 (2004). `http://xmm2.esac.esa.int/docs/documents/CAL-TN-0068-0-1.ps.gz`.

[407] de Plaa, J. *et al.* Cold fronts and multi-temperature structures in the core of Abell 2052. A&A **523**, A81+ (2010). `1008.3109`.

[408] Deslattes, R. D. *et al.* X-ray transition energies: new approach to a comprehensive evaluation. *Reviews of Modern Physics* **75**, 35–99 (2003).

[409] Arnaud, K. A. XSPEC: The First Ten Years. In Jacoby, G. H. & Barnes, J. (eds.) *Astronomical Data Analysis Software and Systems V*, vol. 101 of *Astronomical Society of the Pacific Conference Series*, 17 (1996).

[410] Tsunemi, H. *et al.* Development of a large format charge-coupled

device (CCD) for applications in X-ray astronomy. *Nucl. Instr. and Methods in Phys. Research A* **579**, 866–870 (2007).

[411] Porter, F. Low-temperature detectors in x-ray astronomy. *Nuclear Instruments and Methods in Physics Research Section A: Accelerators, Spectrometers, Detectors and Associated Equipment* **520**, 354 − 358 (2004).

[412] McCammon, D. *Thermal Equilibrium Calorimeters - An Introduction*, 1 (2005).

[413] Takahashi, T. *et al.* The ASTRO-H Mission. In *Society of Photo-Optical Instrumentation Engineers (SPIE) Conference Series*, vol. 7732 of *Presented at the Society of Photo-Optical Instrumentation Engineers (SPIE) Conference* (2010). `1010.4972`.

[414] den Herder, J.-W. *et al.* ORIGIN: metal creation and evolution from the cosmic dawn. *Experimental Astronomy* 30 (2011). `1104.2048`.

[415] Barcons, X. *et al.* Athena (Advanced Telescope for High ENergy Astrophysics) Assessment Study Report for ESA Cosmic Vision 2015-2025 (2012). `1207.2745`.

[416] Kelley, R. L. *et al.* The Suzaku High Resolution X-Ray Spectrometer. PASJ **59**, 77–112 (2007).

[417] `http://astro-h.isas.jaxa.jp/index.html.en`.

[418] McCammon, D. *et al.* A High Spectral Resolution Observation of the Soft X-Ray Diffuse Background with Thermal Detectors. ApJ **576**, 188–203 (2002). `arXiv:astro-ph/0205012`.

[419] Markevitch, M. *et al.* Chandra Spectra of the Soft X-Ray Diffuse Background. ApJ **583**, 70–84 (2003). `astro-ph/0209441`.

[420] Landau, L. D. & Lifshitz, E. M. *Statistical physics. Pt.1, Pt.2* (Course of theoretical physics, Pergamon International Library of Science, Technology, Engineering and Social Studies, Oxford: Pergamon Press, 1980—c1980, 3rd rev.and enlarg. ed., 1980).

[421] Henley, D. B. & Shelton, R. L. An XMM-Newton Survey of the Soft X-ray Background. I. The O VII and O VIII Lines Between l = 120° and l = 240°. ApJS **187**, 388–408 (2010). `1002.4631`.

[422] Henley, D. B. & Shelton, R. L. An XMM-Newton Survey of the Soft X-Ray Background. II. An All-Sky Catalog of Diffuse O VII and O VIII Emission Intensities. ApJS **202**, 14 (2012). 1208.4360.

Samenvatting

De aard van donkere materie is een van de meest intrigerende vragen van
de moderne natuurkunde. Deze materie speelt niet alleen een cruciale rol in
ons begrip van de oorsprong en de evolutie van het heelal, maar het begrip
hiervan zal ook een uitgesproken invloed hebben op de ontwikkeling van de
deeltjesfysica. In feite bevat het Standaard Model van de elementaire deel-
tjes geen geschikte kandidaat voor donkere materie. Door de parameter-
ruimte van donkere-materie deeltjes via onderzoek af te bakenen kan men
onderscheid maken tussen de verschillende mogelijke uitbreidingen van het
Standaard Model om zo meer te leren over de fundamentele eigenschappen
van materie.

Experimenteel gezien is er weinig bekend over de eigenschappen van
donkere-materie deeltjes, zoals hun massa, de sterkte van hun interacties,
en het oorspronkelijke spectrum van hun snelheden. Als men bijvoorbeeld
uitgaat van een specifieke interactie sterkte en een bepaald interactie type,
dan is het mogelijk om de productiesnelheid te bepalen van donkere-materie
deeltjes in het vroege heelal en daarmee ook hun massa. In plaats daar-
van analyseren wij in dit proefschrift model-onafhankelijke grenzen aan de
mogelijke massa van donkere-materie deeltjes die afgeleid worden uit astro-
fysische waarnemingen. Daarnaast wordt vaak verondersteld dat donkere-
materie deeltjes absoluut stabiel zijn. Hun stabiliteit wordt beschermd door
een symmetrie die vaak specifiek voor dit doel is ingesteld. Deze aanname
wordt in dit proefschrift niet gemaakt en *we voeren een systematisch model-
onafhankelijke programma uit om de beperkingen aan de mogelijke levens-
duur en vervalsnelheid van donkere materie deeltjes te bepalen*. Dit wordt
gedaan door te zoeken naar de karakteristieke signalen van verval van don-
kere materie deeltjes. De verkregen resultaten worden vervolgens toegepast
op een goed gemotiveerd model van deeltjesfysica: een minimale uitbrei-

ding van het Standaard Model met drie rechtshandige neutrino's. Dit model biedt een toetsbare verklaring van zowel donkere materie als de materie-antimaterie asymmetrie in het waargenomen Universum, en van de gemeten massa's van neutrino's. De beschikbare ruimte die de parameters in dit model kunnen bestrijken – en die aan alle zijden begrensd is – wordt gebruikt als referentie voor onze model-onafhankelijke zoektocht.

Het proefschrift is als volgt opgebouwd:

I. *Bepaling van de ondergrens van de massa van donkere-materie deeltjes* en het energie bereik van mogelijke zoektochten. Als donkere materie bestaat uit fermionen, kan zijn faseruimte dichtheid niet groter zijn dan die van een ontaard Fermi gas. (Deze beperking kan verder worden aangescherpt door toepassing van de stelling van Liouville). We hebben de bestaande theoretische benaderingen herzien en een nieuwe methode ontwikkeld die het mogelijk maakt om sterke maar robuuste grenzen af te leiden voor de massa van donkere-materie deeltjes. Door de experimentele gegevens te analyseren van objecten met de grootste donkere-materie faseruimtedichtheid – bolvormige dwergsterrenstelsels – wordt aangetoond dat de massa van het donkere materie fermion groter moet zijn dan ~ 0.4 keV, en daarmee ook dat het vervalsignaal van de donkere materie moet worden gezocht in het Röntgen /γ-ray energie bereik. Omdat de vervalsnelheid snel toeneemt met de massa van het deeltje, geniet het Röntgen bereik de voorkeur bij de zoektocht naar vervallende fermionische donkere materie.

II. *Studie naar donkere materie kolomdichtheid in verschillende soorten donkere materie halo's.* Door het analyseren van de verdeling van donkere materie in enkele honderden objecten van verschillende schaal (dwerg-, spiraal-, en elliptische sterrenstelsels, groepen van sterrenstelsels en clusters van sterrenstelsels) die gedomineerd worden door donkere materie, wordt aangetoond dat het verwachte signaal van het verval van donkere materie langzaam toeneemt met de massa van het object. Wij tonen aan dat de gemiddelde centrale donkere-materie kolomdichtheid, welke het verwachte signaal definieert, een universele schalingsrelatie volgt als functie van de totale massa van de halo. De helling van deze afhankelijkheid verschilt tussen geïsoleerde halo's en sub-halo's. Op de beschikbare schalen vallen zowel de schalingsrelaties als de spreiding rond deze relaties heel precies samen met de voorspellingen gedaan door "N-body" simulaties die gebaseerd zijn op het koude donkere materie model.

III. *Identificatie van de beste observationele studie objecten.* Ondanks het feit dat clusters van sterrenstelsels het sterkste donkere-materie vervalsignaal zouden leveren, wordt dit voordeel ten opzichte van kleinere objecten teniet gedaan door hun zeer sterke Röntgen straling. Dit maakt de verwachte signaal-ruisverhouding voor clusters niet optimaal. De beste studie objecten zijn dus dwerg en spiraalstelsels. Het verwachte vervalsignaal van deze objecten varieert maar een halve orde van grootte. Daarom (i) heeft men vrijheid bij het kiezen van de waar te nemen stelsels om ingewikkelde astrofysische achtergronden te vermijden; (ii) is het mogelijk om, indien een spectraallijn als kandidaat voor een vervalsignaal wordt gevonden, de intensiteit hiervan te vergelijken tussen verschillende objecten met een vergelijkbaar verwacht signaal. Dit maakt het mogelijk om *eenduidig* onderscheid te maken tussen het vervalsignaal van donkere materie en het signaal van mogelijke astrofysische of instrumentale achtergronden. Deze werkwijze wordt geïllustreerd met het controleren van een recente claim dat een spectraallijn in een *Chandra* waarneming van een van de satellieten van de Melkweg zou kunnen worden geïnterpreteerd als een vervalsignaal van donkere materie. Ons werk toont aan dat een dergelijke interpretatie met een hoge mate van waarschijnlijkheid kan worden uitgesloten op basis van oude waarnemingen van het Andromeda sterrenstelsel en de Fornax/Sculptor bolvormige dwergsterrenstelsels.

IV. *Gecombineerde analyse van een groot aantal Röntgen waarnemingen.*

We hebben de spectra geanalyseerd van een aantal nabijgelegen objecten die zijn waargenomen door de *XMM-Newton* telescoop; door de ontwikkelde methodologie toe te passen, hebben we de sterkst begrenzingen kunnen vast leggen voor donkere-materie deeltjes met een massa van de orde van grootte van 1 keV. Om de begrenzingen nog scherper te definieren en om de regimes van deeltjesfysica modellen die vanuit een theoretisch perspectief interessant zijn, te onderzoeken, zijn waarnemingen met een lange integratietijd vereist van objecten die gedomineerd worden door donkere materie. Omdat deze aanpak duur is, hebben we een gecombineerde analyse uitgevoerd op een zeer grote dataset van archiefmateriaal van waarnemingen van sterrenstelsels door *XMM-Newton*. De extreem grote gecombineerde integratietijd van deze dataset (twee ordes van grootte langer dan van een typische enkele waarneming) vereist een zeer goede beheersing van systematische fouten en de instrumentele achtergronden, en laat het niet toe om standaard

data-analyse technieken te gebruiken. Ten einde deze problemen het hoofd te bieden, is een nieuwe datareductie methode ontwikkeld. Hiermee werden verschillende nieuwe smalle spectraallijnen als kandidaten gevonden in het 2.5–11 keV bereik. Na een zorgvuldige analyse zijn al deze kandidaten geclassificeerd als zwakke instrumentale lijnen die niet eerder zijn waargenomen. Tenslotte leiden we nieuwe grenzen af voor de vervallende donkere materie parameters. Deze grenzen laten echter nog een groot deel van de parameterruimte van de interessante deeltjesfysica modellen onaangeroerd.

V. Om de gevoeligheid voor de spectraallijn van vervallende donkere materie te verbeteren en om de gehele beschikbare parameter ruimte voor minimale modellen van vervallende donkere materie af te tasten, dient de energieresolutie van een Röntgen telescoop vergelijkbaar te zijn met de intrinsieke breedte van de spectraallijn van de vervallende donkere materie. Dit betekent dat een verbetering van ten minste een orde van grootte ten opzichte van de bestaande Röntgen missies noodzakelijk is. Wij bespreken de mogelijkheid om gebruik te maken van microcalorimeters met een gezichtsveld van ~ 10 graden en de vooruitzichten van toekomstige geplande en voorgestelde missies.

List of Publications

Constraints on decaying dark matter from XMM-Newton observations of M31
A. Boyarsky, D. Iakubovskyi, O. Ruchayskiy and V. Savchenko
Monthly Notices of the Royal Astronomical Society **387** 1361-1373 (2008).

A lower bound on the mass of dark matter particles
A. Boyarsky, O. Ruchayskiy and D. Iakubovskyi
Journal of Cosmology and Astro-Particle Physics **03** 005 (2009).

New evidence for dark matter
A. Boyarsky, O. Ruchayskiy, D. Iakubovskyi, A. V. Macciò and D. Malyshev
arXiv:0911.1774, **to appear**.

Searching for dark matter in X-rays: how to check the dark matter origin of a spectral feature
A. Boyarsky, O. Ruchayskiy, D. Iakubovskyi, M. G. Walker, S. Riemer-Sørensen and S. H. Hansen
Monthly Notices of the Royal Astronomical Society **407** 1188-1202 (2010) — arXiv:1001.0644.

Next decade of sterile neutrino studies
A. Boyarsky, D. Iakubovskyi, O. Ruchayskiy
Physics of the Dark Universe, **1** 136-154 (2012).

Searching for decaying dark matter in stacked spectra of nearby galaxies observed with XMM-Newton
A. Boyarsky, D. Iakubovskyi, O. Ruchayskiy, **to appear**.

Curriculum vitae

Name: Dmytro Iakubovskyi

Date of birth: April 04, 1983

Place of birth: Krivoy Rog, Ukraine

EDUCATION

Jun. 2004: M.Sc. in Physics at Taras Shevchenko National University of Kyiv
Cosmological solutions in theories with one brane
Supervisor: Dr. Yuri Shtanov.

Jun. 2003: B.Sc. in Physics at Taras Shevchenko National University of Kyiv
Solutions of 5D models with branes
Supervisor: Dr. Yuri Shtanov.

Jun. 1999: High School Diploma at Ukrainian Lyceum of Physics and Mathematics (Kiev, Ukraine).

Acknowledgments